Investigation and Mitigation of Degradation in Hydrogen Fuel Cells

Submitted in partial fulfillment of the requirements for

the degree of

Doctor of Philosophy

in

Mechanical Engineering

Pratiti Mandal

B. Tech., Mechanical Engineering

M. Tech., Thermal Sciences and Engineering

Indian Institute of Technology, Kharagpur

Carnegie Mellon University

Pittsburgh, PA

September, 2016

Acknowledgements

I will like to acknowledge support from Phil and Marsha Dowd for their generous Dowd-ICES Fellowship award in 2015, which supported the last year of my PhD. I am grateful to Phil and Marsha Dowd for taking out time to meet the Dowd-ICES fellows and for their support and encouragement. I will also like to thank John and Claire Bertucci, for their generous Bertucci Fellowship award in 2014 that provided financial support for my PhD studies during the years 2014-2015. I am thankful to Dr. Bo Ki Hong (Global R&D Master, Fuel Cell Engineering Design Team, Hyundai-Kia Motors Company, Korea) for proposing the interesting research project which comprises the major part of my dissertation, and for his guidance and active participation in the project execution and discussions. The collaborative research project (R-141594.0001) was supported by Hyundai-Kia Motors Company. The first two years of my PhD research work was supported by the Nation Science Foundation CAREER award (Grant no. 1053752, P.I: Shawn Lister). The acquisition of the nano-CT, which was an important tool that was used for the research work presented in this dissertation, was supported by National Science Foundation MRI award (Grant no. 11229090, P.I.: Shawn Litster). I will also like to acknowledge the travel grants from Graduate Students Assembly, Carnegie Mellon University, Bertucci Fellowship and 3-Minutes Thesis Competition (hosted by CMU Libraries) award for providing support for my conference travels.

I am extremely grateful to my PhD Committee members, Prof. Paul Salvador, Prof. Jonathan Malen, Prof. Venkat Viswanathan and Prof. Shawn Litster (chair) for their time and valuable advice for enriching and completing and improving the dissertation.

Special thanks to Prof. Venkat Viswanathan for the intriguing discussions during my research presentation in the Electrochemical Energy Group (EEG) Meetings and his mentorship.

I also want to take this opportunity to express my gratefulness to my PhD advisor, Prof. Shawn Litster for his unfailing support, advice and mentorship all through the PhD years in CMU. He is very considerate about individual needs of the students and has always been available for advice at every stage of PhD and for future career moves and goals. I am also thankful to him for encouraging collaborative and co-operative culture within his own lab as well as across different research groups in the academia and industry. I will also like to thank him for giving me an opportunity to serve as the Teaching Assistant for his Fluid Mechanics class and also allowing me to give a few guest lectures in the class – it was a very rewarding experience during my PhD years.

I am thankful to my colleagues, Dr. William (Billy) Epting, Dr. Katherine (Kacy) Tully, Dr. Iryna Zenyuk, Seong Jin An, Dr. Siddharth Komini Babu and to all my current lab members, the EEG members for helping me learn new lab-techniques, disclosing valuable PhD life hacks and making my PhD years a fun and enriching experience. I am also grateful to the graduate and undergraduate students whose research work I have supervised and my collaborators from CMU and outside, for being friendly and patient, keeping me motivated, as well as helping me expand my knowledge-base to other fields. I extend my gratitude to the MechE machine shop geniuses, Ed, John and Jim, and all the MechE staff for being extremely friendly and helpful.

Last but not the least, I am extremely grateful to the group of “crazy” friends, most of whom I met during my participation in Indian Graduate Student Association (IGSA) activities, for being so awesome, for giving me unfailing support, and for helping me maintain my sanity during the last four years. I will like to extend my heart-felt gratitude to my family for allowing me to live my dreams, for having faith in me and being encouraging of every career decisions I have taken. I will also like to acknowledge my early career mentors, Hafizul Mondal, Prof. Suman Chakraborty and Dr. Ranabir Dey, who have inspired and encouraged me to pursue a PhD. Special thanks to Dr. Arka Roy for being my partner-in-crime, bearing all my rants and irrationalities, for being a part of the happiest and toughest days, for being the greatest critique of my academic as well as extra-academic undertakings and for being supportive of all my professional and personal endeavors.

Abstract

The ever increasing demand of petroleum in the transport sector has led to depletion of low cost/low risk reserves, increased levels of pollution, and greenhouse gas emissions that take a heavy toll on the environment as well as the national economy. There is an urgent need to use alternative energy resources along with an efficient and affordable energy conversion system to arrest environmental degradation. Polymer electrolyte fuel cells (PEFCs) show great promise in this regard - they use hydrogen gas as a fuel that electrochemically reacts with air to produce electrical energy and water as the by product. In a fuel cell electric vehicle (FCEV), these zero tail pipe emission systems offer high efficiency and power density for medium-heavy duty and long range transportation. However, PEFC technology is currently challenged by its limited durability when subjected to harsh and adverse operating conditions and transients that arises during the normal course of vehicle operation. The hydrogen-based fuel cell power train for electric vehicles must achieve high durability while maintaining high power efficiency and fuel economy in order to equal the range and lifetime of an internal-combustion-engine vehicle. The technology also needs to meet the cost targets to make FCEVs a commercial success. In this dissertation, one of the degradation phenomena that severely impede the durability of the system has been investigated. In scenarios where the cell becomes locally starved of hydrogen fuel, “cell reversal” occurs, which causes the cell to consume itself through carbon corrosion and eventually fail. Carbon corrosion in the anode disrupts the original structure of the electrode and can cause undesirable outcomes like catalyst particle migration, aggregation, loss of structural and chemical integrity. A comprehensive study using advanced electrochemical diagnostics and high

resolution 3D imaging was performed and a new understanding to extend PEFC life time and robustness, by implementing engineered materials solutions, has been achieved. This will eventually help in making fuel cell systems more efficient, durable and economically viable, in order to better harness clean energy resources.

Table of Contents

Acknowledgements ii

Abstract v

List of Abbreviations xi

List of Figures xiii

Chapter 1

Introduction 1

1.1. Fuel Cells for Transportation Applications 1

1.2. Polymer Electrolyte Membrane Fuel Cells 3

1.2.1. *In-situ* Electrochemical Diagnostics 6

1.2.2. *Ex-situ* Material Characterization 12

1.2.3. Degradation in PEFCs 14

1.3. Outline and Overview of the Dissertation 15

Chapter 2

3D Morphological Analysis using Nanoscale X-ray Computed Tomography 18

2.1. Introduction 18

2.2. Nano-CT Imaging Basics 19

2.3. Specimen Preparation Techniques 25

2.3.1. Fuel Cell Electrodes 26

2.3.2. Thin-film and Membranes 30

2.3.3. Dispersed Particles 30

2.3.4. *In-situ* Imaging and Samples Requiring Controlled Environment 32

2.4. Conclusion 36

Chapter 3

Structure-Performance Relationship of PEFC Electrodes 37

3.1. Introduction 37

3.2. Electrochemical Diagnostics 38

3.2.1. Electrode Fabrication 38

3.2.2. Experimental Protocol 39

3.2.3. Electrochemical Characterization 40

3.3. Morphological Analysis 42

3.4. Discussion 47

3.4. Conclusion 48

Chapter 4

Degradation due to Cell Reversal 49

4.1. Introduction 49

4.2. Cell Reversal 51

4.3. Reversal Tolerant Anode 53

Chapter 5

Effectiveness of Reversal Tolerant Anodes 55

5.1. Introduction 55

5.2. Electrochemical Diagnostics 56

5.2.1. MEA Fabrication 56

5.2.2. Experimental Procedure 59

5.2.3. Electrochemical Measurement Results 62

5.2. Morphological Analysis 73

5.3. Conclusion 80

Chapter 6

Role of Water in Degradation due to Cell Reversal 81

6.1. Introduction 81

6.2. Electrochemical Diagnostics 82

6.2.1. MEA Fabrication and Experimental Procedure 82

6.2.2. Electrochemical Measurement Results 83

6.3. Morphological Analysis 93

6.4. Conclusion 98

Chapter 7

Limitation of Existing Reversal Tolerant Anodes 100

7.1. Introduction 100

7.2. Anomalous Behavior of OER Catalyst based Anodes 102

7.3. *In-situ* Electrochemical Diagnostics 106

7.3.1. Electrolyzer with IrO_2 and IrO_2/C Anodes 108

7.3.2. Challenges for In-house Electrolyzer and Possible Solutions 113

7.4. Conclusion 116

Chapter 8

Conclusions and Future Directions 118

8.1. Summary 118

8.2. Future directions 120

References 125

Appendix I: MEA Fabrication Using Decal Transfer Method 151

List of Abbreviations

AFM	Atomic Force Microscopy
BET	Brunauer-Emmett-Teller
CCM	Catalyst Coated Membrane
CT	Computed Tomography
CV	Cyclic Voltammetry
ECSA	Electrochemical Active Surface Area
EDX	Energy Dispersive X-ray Spectroscopy
EIS	Electrochemical Impedance Spectroscopy
FEP	Fluorinated Ethylene Propylene
FER	Fluoride Emission Rate
FOV	Field-of-View
FRT	First Reversal Test (or time)
GDE	Gas Diffusion Electrode
GDL	Gas Diffusion Layer
HER	Hydrogen Evolution Reaction
HOR	Hydrogen Oxidation Reaction
HRES	High Resolution
I-V	Current-Voltage
LFOV	Large Field-of-View
MEA	Membrane Electrode Assembly
Micro-CT	Microscale X-ray Computed Tomography
MIP	Mercury Intrusion Porosimetry
NEXAFS	Near Edge X-ray Absorption Fine Structure
Nano-CT	Nanoscale X-ray Computed Tomography
OCV	Open-Circuit Voltage
OER	Oxygen Evolution Reaction
ORR	Oxygen Reduction Reaction
PEFC	Polymer Electrolyte Membrane Fuel Cell

PEM	Polymer Electrolyte Membrane
PTFE	Polytetrafluoroethylene
RH	Relative Humidity
ROI	Region-of-Interest
RTA	Reversal Tolerant Anode
SEM	Scanning Electron Microscopy
SHE	Standard Hydrogen Electrode
slpm	Standard liter(s) per minute
SNR	Signal-to-Noise Ratio
STXM	Scanning Transmission X-ray Microscopy
TEM	Transmission Electron Microscopy
XCT	X-ray Computed Tomography
XRD	X-ray Powder Diffraction

List of Figures

Figure 1.1. A radar chart showing the current state of fuel cell technology for automotive application as w.r.t. the 2020 DOE targets…….. 3

Figure 1.2. Schematic representation of the microstructure and transport in an MEA. ……. 4

Figure 1.3. (a) Polarization (I-V) curve for a PEFC with the losses (i.e., overpotentials) shown. (b) Power density plot obtained from the polarization curve, showing the dominating losses in different voltage regimes…… 8

Figure 1.4. A typical Nyquist plot obtained from electrochemical EIS measurement on a PEFC, along with the equivalent circuit model used to fit the plot…… 10

Figure 1.5. A typical CV curve for a PEFC, showing the electrochemical reactions corresponding to the current peaks……. 12

Figure 2.1. Schematic diagram of the optics train used in the nano-CT…… 20

Figure 2.2. (a) 3D rendering of a portland cement sample with tomographic slices on the cut-out surface, imaged using LFOV absorption contrast mode. (b) Tomographic slices and volume rendering of Ga-In embedded silicone elastomer, imaged using LFOV absorption contrast mode…….. 21

Figure 2.3. (a) Tomographic slice through 3D image of Li-plated Cu wire. (b) Radiographs of Pt wire embedded polymer sensor. Both imaged in phase contrast mode……..... 21

Figure 2.4. A tomography slice through the reconstructed image of a carbon-based combustion particle, showing phase contrast imaging artifacts…… 22

Figure 2.5. Tomography slices through a PEFC electrode (anode) (a) and track-etched polycarbonate membrane (b), both imaged in HRES phase contrast mode... 23

Figure 2.6. (a) Tomography slices through the imaged volume of soaked hydrogel polymer and volume rendering of the solid phase (dark pixel represent pores) [1]. (b) An intensity based volume rendering of carbon nano-fibers (~100 nm) with PTFE binder…… 23

Figure 2.7. Intensity based volume rendering (LFOV absorption contrast) and tomography slices (LFOV phase contrast)……. 24

Figure 2.8. Schematics of sample preparation and mounting for imaging PEFC electrodes, on MEAs in pristine state (a), and for post-mortem analysis (b)..…… 28

Figure 2.9. (a) A clip-type sample holder with a triangular piece of Kapton® film with dispersed catalyst particles. (b) A Kapton® mesh used for trapping combustion particles to be imaged using nano-CT..…… 32

Figure 2.10. (a) Images of the flow-cell set-up mounted on nano-CT sample holder. (b) Radiographs of polycarbonate micro-capillary with incomplete catalyst layer packing…… 34

Figure 2.11. (a) Image of the in-situ metal-ion battery set-up along with a schematic of the capillary-based cell. (b) Radiographs showing growth of Cu dendrite grown insitu during potential hold at 0.7 V. The plot at the bottom shows the current measured and the time-stamps of the radiographs are marked on the plot…….. 35

Figure 3.1. Polarization curves (a) and power density plots (b) for MEAs with electrodes fabricated using catalyst ink with ultrasonication (black-circles) and without ultrasonication (blue-squares). The error bars show standard deviation in the measured current density values…….. 41

Figure 3.2. (a) Raw tomography slice through the imaged electrode. The brighter pixels represent the solid phase, and the darker pixels represent pore phase. (b) 3D volume rendering of a cropped volume of the imaged electrode segmented into solid (Pt/C/ionomer, shown in grey) and pore phase (shown in dark grey or black). (c) The volume rendering of the solid phase with the agglomerates separated and labeled as different colors…… 43

Figure 3.3. Size distribution of agglomerates in the catalyst layer of the two kinds 44

Figure 3.4. (a) SEM image of the dispersed catalyst ink on a Kapton® film (sputtered with 20 nm of gold). (b) 3D rendering of segmented agglomerate on the same region on the Kapton® film with dispersed catalyst ink, imaged using the nano-CT. (c) Zoomed in images of a few agglomerates present in the FOV of (a) and (b)…… 45

Figure 3.5. Validation of agglomerate model against the experimental data…… 47

Figure 4.1. Cell voltage reversal of a conventional MEA with Pt/C anode……. 52

Figure 4.2. Schematic showing the major electrochemical reactions in a PEFC under regular operating condition and under hydrogen starvation condition (with RTA and without RTA)…….. 54

Figure 5.1. TEM image of an aggregate of IrO_2 nanoparticle synthesized using Adam's Fusion method. On the right is a higher resolution image (zoomed into

the region marked in red on the left image) showing individual IrO_2 nanoparticles with particle diameter of ca. 5 nm…….. 58

Figure 5.2. Voltage vs. time plot for first reversal of conventional MEA (i.e. MEA with RTA 0 wt%). The time has been denoted in terms of voltage reversal time (0 second corresponds to the cell potential becoming negative)…… 61

Figure 5.3. (a) First voltage reversal for MEAs with RTA (5 wt% and 50 wt%) along with MEA without RTA (0 wt%). (b) Voltage vs time plot for first and consecutive reversal tests in RTA 0 wt% and (b) RTA 50 wt% MEAs. …… 64

Figure 5.4. Performance degradation due to cell reversal in MEAs with RTA 0 wt% (a), RTA 5 wt% (b) and RTA 50 wt% (c) shown by polarization curves measured at BOL and after each reversal test (the accumulated reversal time, ART after which the polarization curve was recorded, is shown in the legends). (d) The cell performance is shown in terms of voltage recorded at 1.2 A cm^{-2} current shown as a percentage of BOL value for the three kind of MEAs……. 65

Figure 5.5. Reversal tolerance time of MEAs with different loadings of OER catalyst. FRT is the trace for first reversal test and $ERT_{t=35\%}$ is the total reversal time till EOL was reached (i.e. degradation to 35% of BOL performance)…… 66

Figure 5.6. Cell performance degradation rate due to cell reversal after first reversal test (a) and average degradation rate over the total reversal time (b)…… 67

Figure 5.7. Nyquist plot from EIS measurements done of the RTA 0 wt% (a), RTA 5 wt% (b) and RTA 50 wt% (c)MEAs at BOL(black, squares), after first reversal test(blue, diamonds) and at EOL(red, circles). Change in Ohmic resistance (d), cathode charge transfer resistance (e) and anode charge transfer

resistance (f) of the MEAs with increase in voltage reversal time……. 69

Figure 5.8. (a-c) Cathode CVs for RTA 0 et%, RTA 5 wt% and RTA 50 wt% respectively. (d-f) Anode CVs for RTA 0 wt%, RTA 5 wt% and RTA 50 wt% respectively. The three traces are for CVs measured at BOL, after first reversal test and after EOL was reached, with the total reversal time denoted in the figures. 71

Figure 5.9. Change in ECSA of Pt catalyst in the cathode (estimated from cathode CV) shown as percentage w.r.t. to the ECSA at BOL for all the MEAs with increasing accumulated reversal time (ART)……. 72

Figure 5.10. Change in the difference in the H-adsorption peak on Pt with accumulated reversal time, obtained from the anode CVs of the MEAs…… 72

Figure 5.11. 3D volume renderings of the anodes in pristine state are shown on the left (a, c and e) and in the EOL state is shown on the right (b, d and f). The volume in purple/blue is the intensity based rendering of the raw image showing the porous matrix of Pt/C-ionomer. The IrO_2 is rendered in orange. The greyscale images, on the right of the volume renderings show a virtual cross-section (tomographic slice) through the imaged volume of the anode, in which, the bright zone is the anode. (The large bright parts are IrO_2 and the grey region is the Pt/C-ionomer matrix)…….. 74

Figure 5.12. A schematic representation of a degraded RTA, showing carbon loss, Pt-catalyst agglomeration and isolation, and highly resistive ionomer network near the membrane……. 75

Figure 5.13. (a) Anode thickness in pristine and EOL state of the MEAs. (b) and (c) Total volume and surface area of the segmented IrO_2 agglomerates in the

pristine and EOL of RTA 5 wt% and RTA 50 wt% specimens, respectively. The bars show average value and the error bars show the standard deviation in the values…….. 77

Figure 5.14. SEM images of MEA cross-sections: (a) MEA (RTA 0 wt%) in pristine condition and (b), an MEA (RTA 5 wt%) in EOL condition after several cell reversal tests…… 79

Figure 5.15. Fluoride emission rate during regular operation and during reversal tests measured from effluent water from anode and cathode of the RTA 0 wt% MEA…… 79

Figure 6.1. (a) First reversal behavior of RTA 50 wt% MEA undergoing cell reversal at different RH conditions. (b) First reversal time (FRT) as a function of the RH. The dotted line is used as a visual guide. The shaded regions denote operation regimes for an RTA…… 84

Figure 6.2. Cell potential measured at low RH under regular reactant gases (i.e. H_2 at anode and air at cathode) shown to the scale of the voltage reversal plots. The inset is a zoomed in version of the plot to show small fluctuation in the voltage measured…… 86

Figure 6.3. (a) Polarization curves measured at BOL and after each reversal test performed at 82% RH. (b) Performance decay of RTA MEAs due to cell reversal.. 88

Figure 6.4. Degradation rate during first cell reversal at different RH conditions… 89

Figure 6.5. Nyquist plots for EIS measured at BOL (black-diamonds), after first cell reversal (blue-squares) and at EOL (red-circles) for MEAs that have undergone cell reversal at 28% RH (a), 68% RH (b), and 82% RH (c)……. 90

Figure 6.6. Anode CVs at BOL, after first cell reversal and at EOL for MEAs that have undergone cell reversal at 28% RH (a), 68% RH (b), and 82% RH (c)…… 92

Figure 6.7. SEM images of anode surface of pristine MEA (a) and that of EOL MEA (i.e., catalyst layer-GDL interface) that has undergone cell reversal at 68% RH (b). The images on the right are the zoomed in images. The images were obtained using back-scatter electron detector. The brightest zones are IrO_2 agglomerates and the darkest regions are the pores and cracks on the anode surface. The medium greyscale intensity is the Pt/C/ionomer porous network……. 95

Figure 6.8. 3D volume rendering of anode of pristine MEA (a) and EOL MEAs which have undergone cell reversal at 28% RH (b), 68% RH (c) and 82% RH (d). The grayscale image on the right face of the volume shows a virtual cross-section through the imaged anode volume. IrO2 agglomerates have been segmented and rendered in orange in the 3D volume and they are the brightest phase in the tomographic slices shown. The intensity based rendering of the porous network of Pt/C/ionomer is shown in purple and is the bright layer in the tomographic slices. The footprint area of the anode volume rendered is 36 μm×36 μm…….. 96

Figure 6.9. Anode thickness and the total volume and surface area of IrO_2 agglomerates present in the EOL MEA shown as percentage of the quantities in the pristine anode. The bar height for the anode thickness shows the average value measured over all the tomographic slices through 36 μm×36 μm footprint area of the imaged anode volume with the error-bars showing the standard deviation……. 98

Figure 7.1. The first reversal time for RTA 50 wt% MEAs subjected to cell reversal at 65C and 90C, at medium to high RH conditions. The data points are shown with blue squares and red circles respectively. The dotted lines are trend lines used as visual guides…….. 103

Figure 7.2. (a) Hypothesized trend for the dependence of the rate of OER activity of IrO_2 and the activity of carbon towards carbon oxidation (or corrosion), on water activity (i.e., RH).(b) A schematic for the hypothesis of non-uniform ionomer coverage on IrO_2 particles (or agglomerates) as compare to that on Pt/C... 108

Figure 7.3. Image of the disassembled electrolysis cell hardware…… 111

Figure 7.4. Cell potential (equivalent to anode half-cell potential) during OER in PEM electrolyzer operated at 0.2 A cm^{-2}……... 111

Figure 7.5. (a) Anode CVs at BOL and after 10 hr of OER in MEA with IrO_2 anode (b) Anode CVs at BOL and after 10 min of OER (i.e. after failure) of MEA with IrO_2/C anode……... 112

Figure 7.6. SEM images of electrolyzer anode surfaces with IrO_2 (a) and IrO_2/C (b). The zoomed in images of the red box bounded areas are shown below the corresponding images. Secondary electron detector was used. The bright agglomerated volumes were primarily composed of IrO_2……. 114

Figure 7.7. Areal elemental map of IrO_2/C anode obtained from EDX. (a) SEM image of the area mapped. (b)-(e) Map for F, Ir, O and C respectively……. 115

Figure 8.1. (a) Schematic of catalyst degradation caused by carbon loss due to the carbon corrosion reaction. (b) Schematic of a well-dispersed OER catalyst (IrO_2), in a Pt/C matrix with good ionomer coverage for an effective RTA design…….. 123

Chapter 1

Introduction

1.1. Fuel Cells for Transportation Applications

Fuel cells are highly efficient systems that convert the chemical energy in fuels, such as hydrogen, methanol, carbon-monoxide, light hydrocarbons, etc. into electrical energy through electrochemical reactions. These fuel cells can be employed as efficient energy conversion devices for transportation, industrial, commercial and residential energy sectors. Fuel cells provide fuel flexibility, and can use renewable fuels including natural gas, biogas, etc. This reduces the dependence on petroleum imports and thus offers benefit to the national economy and energy security as well as enables the expanded utilization of renewable power (through use for hydrogen generation, storage and transmission). The transportation energy sector has contributed to the highest amount of green-house gas emission into the earth's atmosphere in the last decade, and 70% of petroleum consumption, which has dire consequences to the environment, health and economy [2]. Replacing the conventional gasoline engines with high efficiency and zero-emission electrical powered engines is necessary for moving towards a sustainable future. Hydrogen fuel cells that are also known as polymer electrolyte membrane fuel cells

(PEFCs) are popularly used for energy conversion in transportation energy sector. With the energy conversion and storage being decoupled for a fuel cell system, PEFCs can be employed in vehicles of short to high range, and from light to heavy duty. Unlike gasoline vehicles, fuel cell electric vehicles (FCEVs) are highly efficient, reliable, low maintenance and zero-tailpipe-emission systems. They share the similarity with gasoline vehicles in their refueling capability and high mile range. The prospect of replacing gasoline vehicles by electric vehicles has triggered a great volume of research and development activity for innovating material components, operation strategy and auxiliary systems for fuel cells. Great progress has been met in achieving the Department of Energy (DOE) automotive fuel cell 2020 targets of high power density, specific power and vehicle start and operation from freezing temperatures. However, the targets towards reducing the cost of the system down to $40/kW, increasing energy efficiency to 65% and meeting a total durability of 5000 hours operation of a fuel cell stack by the year 2020 are yet to be achieved [3]. The radar chart showing the 2020 targets and the current status of the fuel cell technology, from the 2016 Annual Merit Review, Fuel Cell Technologies Office report is shown in Figure 1.1. In this dissertation, one of the degradation phenomena which challenge the durability and robustness of a fuel cell in automotive application has been investigated. The discussion has been coupled with economic optimization as well as the importance of the electrode morphology towards gaining high performance and cost minimization of the existing Pt-catalyst based hydrogen fuel cells.

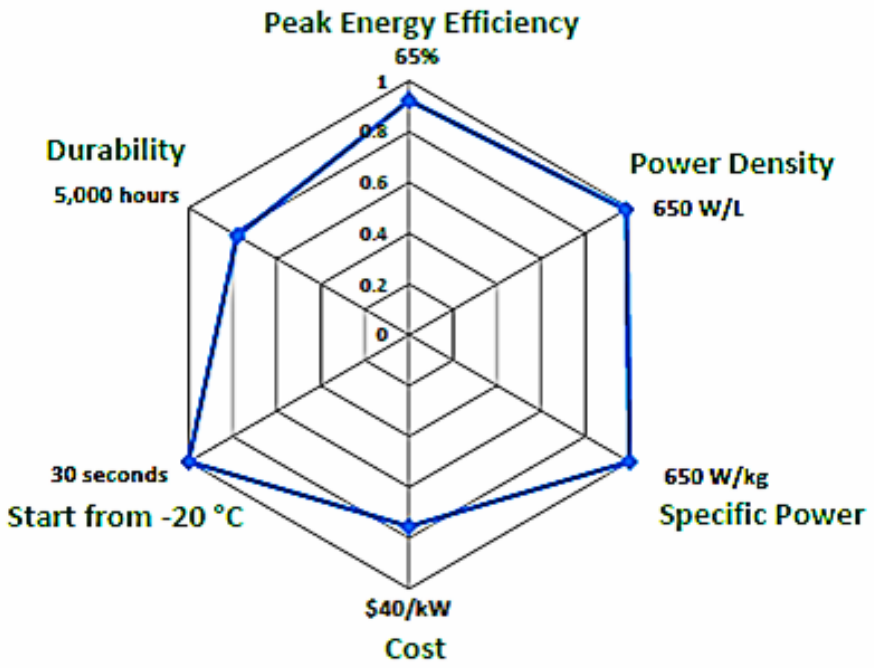

Figure 1.1. A radar chart showing the current state of fuel cell technology for automotive application as w.r.t. the 2020 DOE targets.

1.2. Polymer Electrolyte Membrane Fuel Cells

At a very basic level, hydrogen fuel cells or PEFCs are comprised of a cathode, anode, and membrane- the entire unit is termed as the membrane electrode assembly (MEA). A schematic of an MEA is shown in Figure 1.2. Hydrogen splits into protons (H^+) and electrons (e^-) in the anode. The electrons go through an external circuit driving the electric load, while the polymer electrolyte membrane (PEM) allows protons to move from the anode to the cathode. At the cathode, the electrons and protons react with oxygen to produce water. The electrodes are porous, micro-structured films (also known as catalyst layer) consisting of carbon supported platinum catalyst nanoparticles bound in polymer electrolyte (ionomer) films that form a complex network of aggregates or

agglomerate structures with small-primary pores within them and larger secondary pores between the agglomerates [4], [5]. Hydrogen oxidation reaction (HOR) and oxygen reduction reaction (ORR) that takes place on the Pt catalyst in anode and cathode respectively, as shown in Equations 1.1 and 1.2, along with the equilibrium potentials:

$$H_2 \leftrightarrows 2H^+ + 2e^-, \quad E^o = 0.00 \text{ V } (vs. \text{ SHE}) \qquad [1.1]$$

$$O_2 + 4H^+ + 4e^- \leftrightarrows 2H_2O, \quad E^o = 1.23 \text{ V } (vs. \text{ SHE}) \qquad [1.2]$$

The ORR has more sluggish kinetics than the HOR, and hence catalyst loading in the cathode is maintained higher than that of the anode. Thus, the cathode catalyst layer is thicker than the anode catalyst layer, which has a lower Pt loading [6].

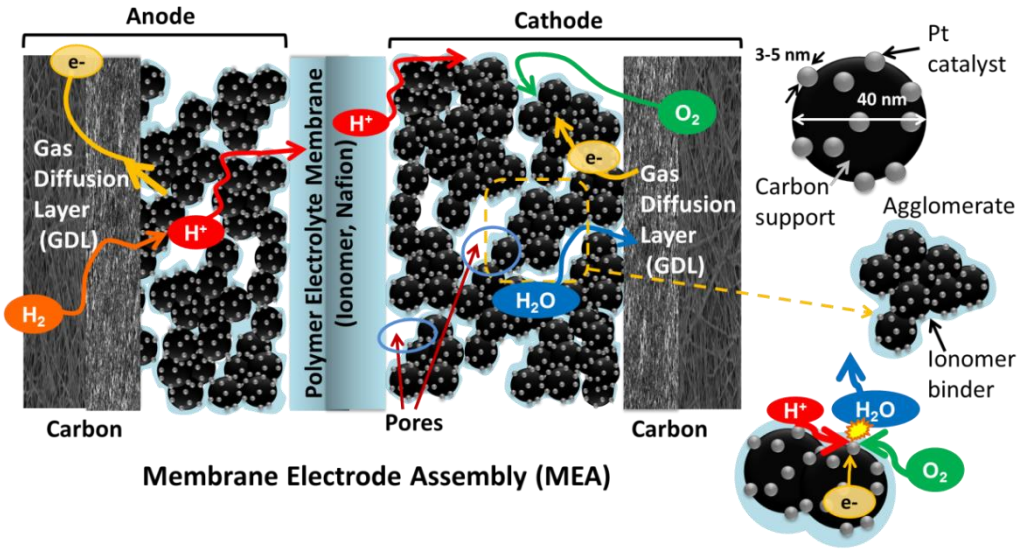

Figure 1.2. Schematic representation of the microstructure and transport in an MEA.

The catalyst layer microstructure, which determines the mass transport characteristics of the electrode, is very crucial to the performance output of a PEFC. The layer has to be porous and have percolating pore network, to allow the gaseous reactants

reach the reaction sites; and at the same time should have a good distribution of ionomer for the protons to be conducted to the Pt sites, which should be electronically well connected through a percolating conductive network. The structure should also be capable of effectively removing the by-product water, which might condense in the pores and prevent reactants from reaching the Pt sites, especially at the cathode. Water management is also very important for proper functioning of a PEFC. The ionomer widely used in the fuel cell and as the PEM is a perfluorosulfonic acid (PFSA) based ionomer, Nafion®, which needs to be hydrated for high proton conductivity, and at the same time, accumulation of liquid water within the catalyst layer needs to be prevented [4], [7]. The microstructure and operation strategy affects the water management within the electrodes.

The catalyst layers have a carbon based gas diffusion layer (GDL) on both sides of the MEA to provide electrical contact between the electrodes and the current collector, along with better water removal characteristics and mechanical and structural integrity to the MEA. The GDL architecture and design can be engineered for effective water removal from the MEA [8]. The GDL (carbon paper or cloth) is often treated with a hydrophobic polymer, like polytetrafluoroethylene (PTFE), to aid in water removal. It is also often coated with a micro-porous layer, with similar micro-structure as the catalyst-layer, to improve the mechanical compatibility, good contact, and effective wicking of liquid water into the GDL [9]–[11]. The catalyst layer can be prepared by coating the ionomer-Pt/C catalyst particles dispersion onto the GDL, forming a gas diffusion electrode (GDE) [12] or coated onto the PEM, to form a catalyst-coated membrane (CCM) [13], [14].

The transport pathways of the electrochemical reaction species that are illustrated in Figure 1.2 shows that a well-designed microstructure is indispensable to the efficient functioning of the fuel cell. Any disruption of the electrode morphology or degradation of any component of the cell is detrimental to the functioning of the PEFC. The experimental way of studying the performance, for diagnosing inefficacies and degradation phenomena in a fuel cell is through *in-situ* electrochemical tests and diagnostics, as well as *ex-situ* material characterization.

1.2.1. *In-situ* Electrochemical Diagnostics

The interplay of several electrochemical kinetics and transport mechanisms is responsible for power generation by a hydrogen fuel cell. In order to quantify the performance of a fuel cell and to diagnose loss of performance, it is necessary to measure its properties and electrochemical characteristics while in operation. It also helps in evaluating the effectiveness of any particular component of the PEFC. The popular tests for performing in-situ electrochemical diagnostics are measurement of polarization curve or current-voltage (I-V) curve, electrochemical impedance spectrum (EIS), and cyclic voltammetry (CV). Each of these techniques and their implications has been discussed in the following subsections [15], [16].

Polarization curve

Polarization or I-V curve is recorded by measuring the steady-state response of a fuel cell. It alloys direct measurement of the performance of a cell at a given operating condition. Power output of a fuel cell can be directly obtained from the polarization curve. The measurement can be performed in a potentiostatic mode: controlling potential

and recording current output, or a galvanostatic mode: controlling current and recording voltage output. Several current and voltage steps are usually used in monotonically increasing (for current) or decreasing (for voltage) order starting at the open-circuit state. A typical polarization curve for an MEA is shown in Figure 1.3(a). The current is usually plotted as current density, i.e., current output divided by the geometrical active area of the MEA. For a fuel cell, the power or current output is directly proportional to the area of the MEA. Hence, for a fair comparison between MEAs and for different operating conditions current density serves as a better metric. Figure 1.3(b) shows the power output curve calculated from the polarization curve shown in Figure 1.3(a).

The potential recorded at each current density is lower than the equilibrium cell potential because of losses in the system. The open-circuit voltage (OCV) is also lower than the equilibrium cell potential because of losses in the system induced by parasitic reactions within the electrodes, especially, due to H_2 cross-over into the cathode across the membrane. When a load is applied across the electrode while fuel and oxidant is being supplied to the anode and the cathode respectively, losses induced by reaction kinetics (activation overpotential), electronic and protonic resistance (Ohmic overpotential) and mass transport limitation (concentration overpotential) due to finite rate of diffusion of the reactant species through the pores of GDL and catalyst layer to the reaction sites are observed. The regimes dominated by each of these losses are shown in Figure 1.3(b).

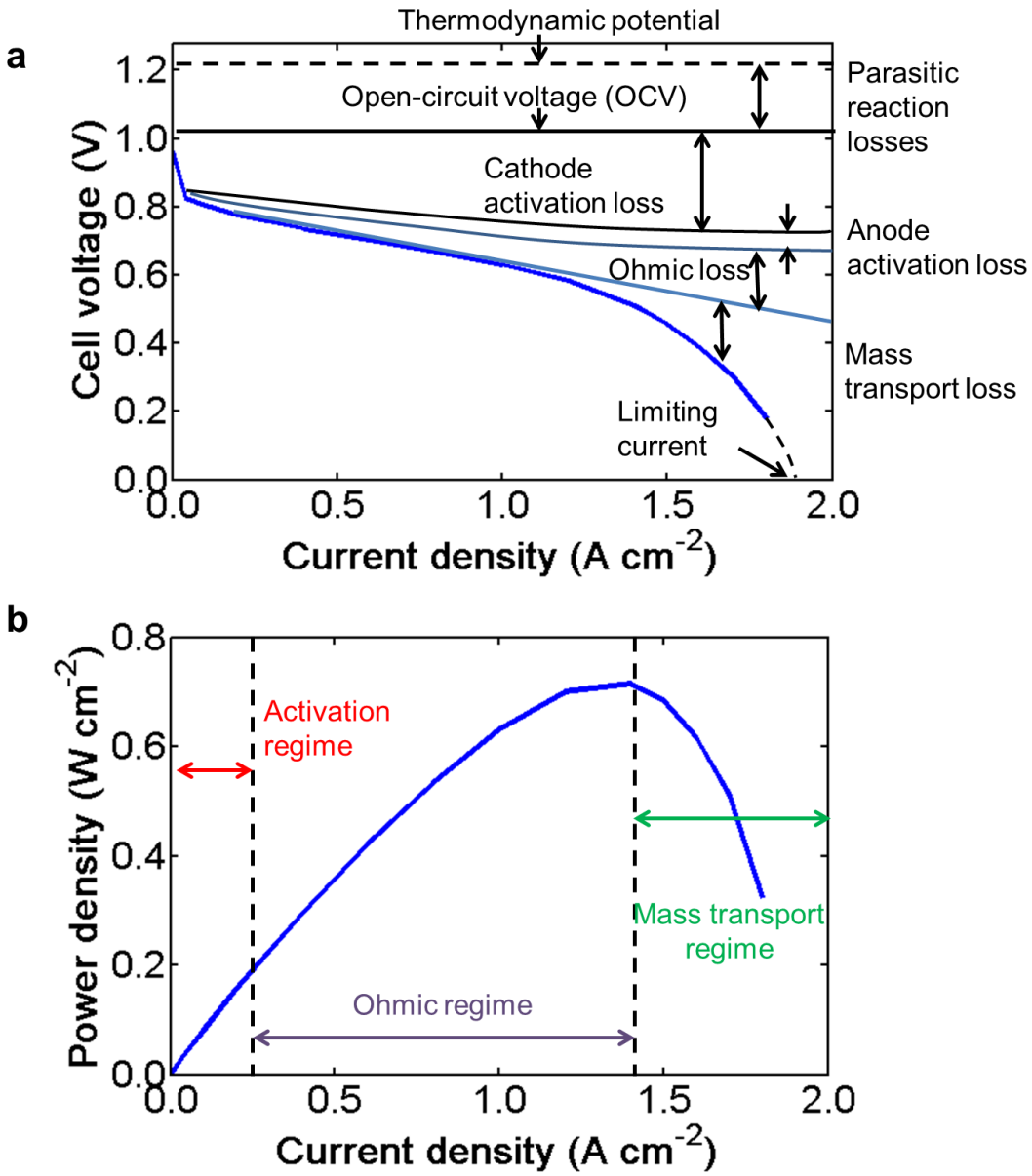

Figure 1.3. (a) Polarization (I-V) curve for a PEFC with the losses (i.e., overpotentials) shown. (b) Power density plot obtained from the polarization curve, showing the dominating losses in different voltage regimes.

Electrochemical impedance spectroscopy (EIS)

Electrochemical impedance spectroscopy (EIS) measures the dynamic response of an electrochemical system unlike polarization curve measurement. It provides

information on the individual losses in the system. EIS is measured by recording the current response to a sinusoidal potential applied across the fuel cell or vice-versa. The measurement is done over a range of frequencies at a particular potential with fixed amplitude. The amplitude of variation is usually kept low (5% of the bias current in case of galvanostatic EIS), such that the current or voltage response within the range lies in the linear response zone on the polarization curve. EIS measurement is usually plotted as a Nyquist plot, as shown in Figure 1.4. The activation or kinetic losses in the anode and cathode can be considered as impedances in series with the Ohmic resistance which can be considered as a linear resistor. The Nyquist plot can be fitted with an equivalent circuit model (shown as an inset in Figure 1.4). The anode and cathode impedances are represented as units with a resistor (representing Faradaic resistance, which is a function of kinetics of the electrochemical reactions) and capacitor (representing double-layer capacitance, which depends on the capacitive nature of the electrode-electrolyte interface) connected in parallel. The values of the component of the impedances can be de-convoluted from the Nyquist plot obtained from EIS measurement and used to understand the individual losses in the system. At low current values (in the activation regime), the mass transport losses are minimal and the loops in the Nyquist plot denote the kinetic losses in the anode and cathode. The equivalent circuit model used in the dissertation is a simplified model which allowed us to estimate the effect of the degradation phenomena on the Ohmic resistance and electrochemical kinetics of the anode and cathode reactions.

EIS however is difficult to conduct on a high power system or at fuel cell stack level; in which case, current-interrupt method is implemented to get an estimate of the individual losses.

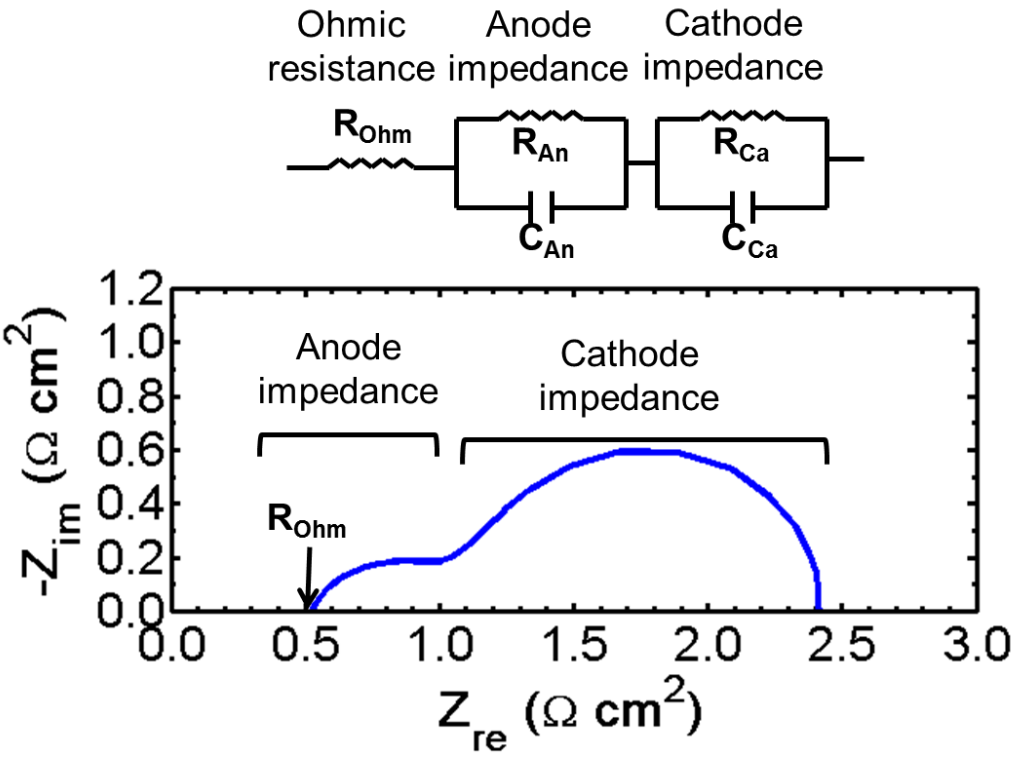

Figure 1.4. A typical Nyquist plot obtained from electrochemical EIS measurement on a PEFC, along with the equivalent circuit model used to fit the plot.

Cyclic voltammetry (CV)

Cyclic voltammetry (CV) is also a dynamic response measurement for an electrochemical system. It is used to characterize the catalyst activity in a fuel cell. The measurement is done by sweeping the potential back and forth from nearly 0 V to around 1.2 V (or lower) at a constant rate and the current response is recorded and plotted against the voltage. A typical CV curve is shown in Figure 1.5. The current response is a

combination of the constant capacitive charging current, which due to the linearly changing voltage and the current, and due to electrochemical reactions on the electrochemically active catalyst surface. In order to characterize the electrochemical activity of Pt catalyst in a PEFC, CV is performed in hydrogen-pumping mode, where hydrogen is supplied to the counter or reference electrode and the working electrode is supplied with inert gas like nitrogen. The peaks in the CV in 0.1-0.3 V range corresponds to hydrogen adsorption-desorption on the Pt active sites and the area under the curve is used to estimate the electrochemically active surface area (ECSA) of the Pt catalyst in the electrode. For the most accurate estimate of the ECSA using CV, the gas flow rate and temperature in the working electrode should be low [17]. The ECSA calculation in the dissertation uses the total charge transfer during hydrogen adsorption instead of the charge transfer during hydrogen desorption, which tends to vary with the change of the upper limit of the voltage sweep [18]. The ECSA was calculated as follows:

$$\mathrm{ECSA} = \frac{\mathrm{Q}_h}{\text{catalyst loading} \times \mathrm{Q_m}}$$

Where, Q_h and Q_m are the total charge transfer due to hydrogen adsorption onto Pt sites and the adsorption charge for an atomically smooth Pt surface. Q_m is considered to be 210 μC/cm^2. The area used for ECSA calculation is shown in Figure 1.5 (the voltage axis is converted to time for calculating the area).

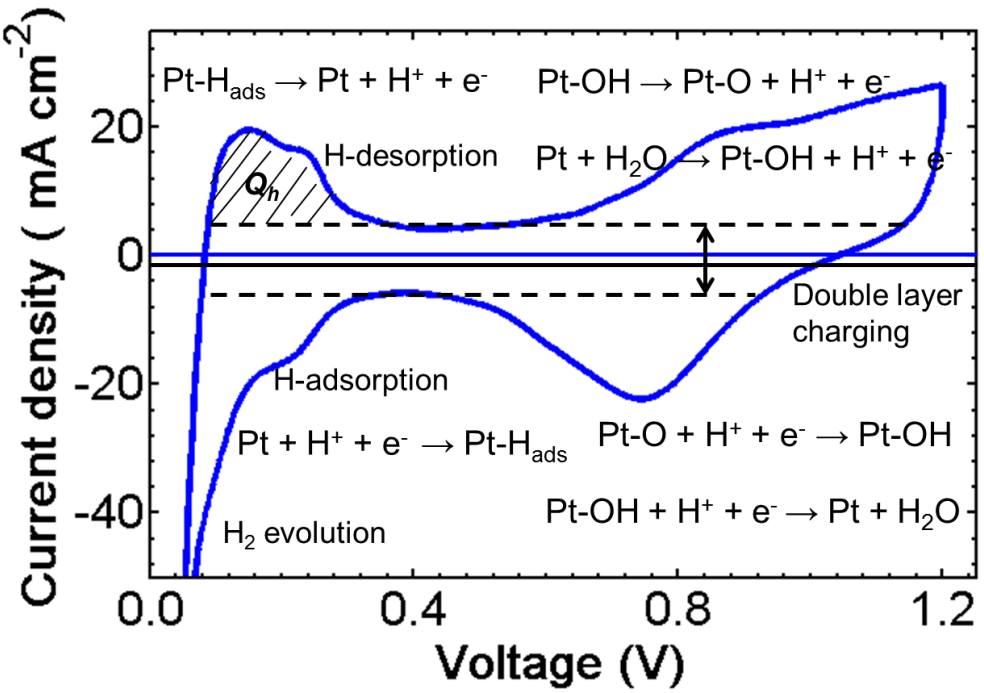

Figure 1.5. A typical CV curve for a PEFC, showing the electrochemical reactions corresponding to the current peaks.

1.2.2. *Ex-situ* Material Characterization

As discussed earlier, the micro-structure of the fuel cell electrodes and GDL and the state of the PEM reflects on the electrochemical response obtained from the fuel cell. Besides, morphology, the chemical characteristics of the components also affects the cell performance. Thus, *ex-situ* material characterization is important for analyzing material and components of a fuel cell before being employed into an MEA to predict the performance and also after being tested and cycled for durability studies.

The porosity of the electrodes can be determined by using ex-situ methods like mercury-intrusive-porosimetry (MIP) [19] and catalyst surface area can be determined by Brunauer-Emmett-Teller (BET) method [15].

Several imaging tools (besides optical microscopy) have been used to determine structures of the components of an MEA. The electron based tools like scanning electron microscopy (SEM) and transmission electron microscopy (TEM) have been widely used to analyze MEA surface, cross-section in both pristine and degraded state, the latter being popularly used to study electrocatalyst structure, distribution and degradation [18], [20]–[25]. X-ray based techniques like scanning transmission X-ray microscopy (STXM) [26]–[29], near-edge X-ray absorption fine structure (NEXAFS) [27], X-ray photon spectroscopy (XPS) [30], [31], X-ray diffraction (XRD) [18], [32], energy dispersive X-ray spectroscopy (EDX, which in-fact, can also performed in an SEM, using electron beam instead of X-rays) [32], [33], X-ray computed tomography (XCT: micro-CT and nano-CT denoting microscale and nanoscale resolution yielded by the systems respectively) [5], [19], [34]–[37]. Atomic force microscopy (AFM) has also been implemented to characterize structural and electronic properties of the catalyst layer and the PEM or other PEFC precursors [31], [38]–[41].

XCT is used to obtain three-dimensional (3D) images and specimen can be imaged in ambient conditions or under controlled environmental conditions. Hence, it has been used for *in-situ* and *in-operando* studies for fuel cells, e.g., to study evolution of the structure or image water transport through the pores and gas channels of the fuel cell hardware [36], [42], [43]. Neutron imaging has also been used for *in-situ* visualization of water transport in a fuel cell while in operation [44]–[47]. In this dissertation, nano-CT, SEM and EDX have been used for material characterization.

1.2.3. Degradation in PEFCs

Limited durability of a PEFC, when used in a fuel cell stack of an FCEV increases the lifetime cost of the system and reduces the reliability of the technology. In order to meet the 5000+ hours operation of an FCEV, each component of the fuel cell should be resistant to stress conditions [3]. The catalyst and catalyst support are crucial to effective performance of the fuel cell and hence it is important to prevent their degradation. An automotive fuel cell stack experiences several start-up/shut-down (SU/SD) cycles during its lifetime. SU/SD causes air-fuel boundary in the anode, which can cause the cathode half-cell potential to shoot higher than 1 V, which induces carbon corrosion [48]–[50]. Air-fuel boundary can be prevented by adopting protected SU/SD with advanced operational strategies. MEA degradation can occur when the cell in in idling state, or at open circuit potential [51]–[53]. The high potential can cause damage to the catalyst support at the cathode. The high potential can also accelerate ionomer degradation. The transients that an automotive fuel cell is subjected to, also challenges the durability of the catalyst. Large potential swings and cycling can cause Pt dissolution [54]. Besides loss of catalyst ECSA, it can also cause Pt migration/deposition into the PEM [55]. Pt in the PEM can in-turn cause severe degradation of the PEM by free radical (•OH) formation that can cause the polymer chain scission [51], [56]–[58]. This leads to membrane thinning (and eventual pin holes in the PEM, leading to cell failure) or electrical shorting by the Pt nanoparticle network. Another common cause for catalyst degradation is poisoning. Carbon-monoxide or other contaminants present in H_2 feed gas or in the air feed can cause passivation of the Pt ORR and HOR reaction sites; thus, adversely affecting the cell performance [59], [60]. Cation contaminants can adversely affect the

ionomer conductivity as well [51]. Cathode flooding can cause temporary loss of cell performance because the reactant gases cannot reach the Pt sites [61], [62]. However, the degradation of performance is reversible in this case and the power revives when the water is removed. This is also analogous to the case when the cathode might have a depleted supply of air, causing the cell to lose power, but does not cause any irreversible damage to the cell [51]. On the other hand, hydrogen fuel starvation at the anode, caused by anode flooding or blockage in the fuel supply line or during freeze-start, etc., can cause severe irreversible damage to the cell and cause catastrophic cell failure [63]–[66]. Fuel starvation can cause "cell reversal" (more details in Chapter 4) due to high potential at the anode that induces carbon corrosion. The anode, which has a low catalyst loading, can be easily depleted of its carbon support. Besides, catalyst agglomeration and loss of ECSA, the corrosion can extend to the GDL carbon as well and the high potential can cause cell heating, membrane thinning and pin holes and electrical shorting of the cell, causing the cell to meet "sudden death", which can shut down the fuel cell power, causing the car to stop abruptly. Cell reversal is a serious degradation issue that needs to be addressed for ensuring safety of an FCEV and commercial success of fuel cell technology. In this dissertation, cell reversal caused by fuel starvation, has been investigated. A strategy of protecting the cell from failure has been discussed along with the limitations of the existing strategy and ways of mitigation.

1.3. Outline and Overview of the Dissertation

This dissertation contains detailed discussion of degradation phenomena which can severely shorten the life of a fuel cell stack used for automobile application, thus

increasing the lifetime cost of such a system. The studies have been performed on lab-scale with well controlled operating conditions, in order to delineate the effects of different operation parameters (such as gas flow rate, temperature, relative humidity, catalyst loading, etc.), understand the mechanism of such degradation phenomena and the effectiveness of the solution strategy. All the PEFCs were operated in single-cell mode. Besides performing in-situ electrochemical diagnostics, we also analyzed the micro-structure of the cell components.

The basics of the functioning and implementation of nano-scale X-ray computed tomography (nano-CT) has been described in Chapter 2. This imaging technique was mostly used for acquiring three-dimensional images for characterizing the fuel cell electrodes. The Chapter has mention of few other material characterization examples from collaborative research activities and independent projects besides the dissertation topic.

Chapter 3 contains details of a project on correlative study of PEFC performance and micro-structure of the electrode, which highlighted the importance of electrode architecture at nano- and micro-scale towards minimizing under-utilization of expensive Pt catalyst and improving the power output of the cell. The work served as a robust way of analyzing fuel cell electrodes and relating the micro-structural features to the overall performance of the cell when used for power generation. The analysis method used, has been implemented in other research projects undertaken in our research group.

Chapter 4 introduces the degradation phenomenon that is caused by fuel (hydrogen) starvation and how it can lead to catastrophic failure of conventional fuel cell.

In-situ electrochemical diagnostics and morphological analysis was performed to study the change in performance, structure and properties of the MEA due to starvation.

The application of a material-based mitigation strategy to combat the fast degradation due to fuel starvation: causing cell reversal is explained in Chapter 5. A reversal tolerant anode for the study was designed by adding water-electrolysis catalyst in addition to hydrogen-oxidation electrocatalyst (Pt). The effectiveness and utilization of the additional catalyst was analyzed by varying the catalyst loading in the anode. Chapter 6 discusses the effect of temperature and relative humidity on the effectiveness of the material-based degradation mitigation strategy. The limitations and the challenges encountered with the material to ensure long-term protection of the cell, has been investigated further, with controlled experiments and ex-situ material characterization. The preliminary results that verified part of the hypothesis for deactivation of the catalyst have been presented.

Finally, Chapter 8 summarizes the dissertation and also discusses the future directions for the research. The possible strategies that can be implemented to protect PEFC electrocatalyst and meet the durability goal for Pt-based PEFCs for automotive application have been described.

Chapter 2

3D Morphological Analysis using Nanoscale X-ray Computed Tomography

2.1. Introduction

The nano-CT is a unique tool which allows non-invasive imaging of internal structures of composite material in high-resolution. The system obtains X-ray transmission images of the sample from several angles and then the images are computationally back-projected and combined to yield a 3D image of the sample. The advantages of using nano-CT over other 3D microscopy techniques, e.g. focused-ion beam sectioning with scanning electron microscopy (FIB-SEM) and transmission electron microscopy CT (TEM-CT), are the ambient imaging environment and non-destructive imaging processes, enabling in-situ, in-operando, and 4D (i.e., 3D spatial and time) studies [19], [36], [67]–[70]. The system used for obtaining 3D images presented in

the dissertation, was the UltraXRM-L200 (also known as the Ultra-800, Carl Zeiss X-ray Microscopy-formerly Xradia, Inc., Pleasanton, CA, USA). This system is lab-scale nano-CT with low X-ray dosage (compared to the synchrotron sources), which is advantageous, because the X-ray is less damaging to sensitive materials e.g. polymers like Nafion® [71], living cells like yeast, etc. [72], [73]. However, the low dosage decreases the photon counts and hence to maintain high signal-to-noise ratio (SNR), the exposure times are usually of the order of minutes. In this chapter, the imaging basics of the X-ray microscope and the various methods used for specimen preparation and imaging fuel cell samples as well as other materials have been described.

2.2. Nano-CT Imaging Basics

The nano-CT (UltraXRM-L200) uses a copper-rotating anode that generates X-ray of 8 keV energy, powered by a lab-scale X-ray generator (40 kV, 30 A). The X-ray passes through a mono-capillary condenser, which uses reflective optics and high aperture to re-focus the X-rays onto the sample after passing through the pinhole. The high resolution attained (with limitation on the source to object and object to detector distance) is because of the high-precision zone-plate (Fresnel diffraction lens) used in the system [74]. Figure 2.1 shows a schematic of the nano-CT optics. The X-ray computed tomography uses radiographs (transmission X-ray images) obtained from different angles of the sample and computationally reconstructs the 3D structure by filtered back projection of the radiographs. The imaging is done in the ambient environment. The maximum resolution is 50 nm (limited by the resolution achieved by the Fresnel zone-plate) with a maximum pixel resolution of 16 nm. There are two modes of operation of

the nano-CT categorized by the field-of-view (FOV) and image resolution: The high resolution (HRES) mode, with 16 µm FOV, voxel size of 16 nm (practical limit of spatial resolution is 50 nm) and the large field-of-view (LFOV) mode, with 65 µm, voxel size of 64 nm (practically achieved spatial resolution is 120-150 nm).

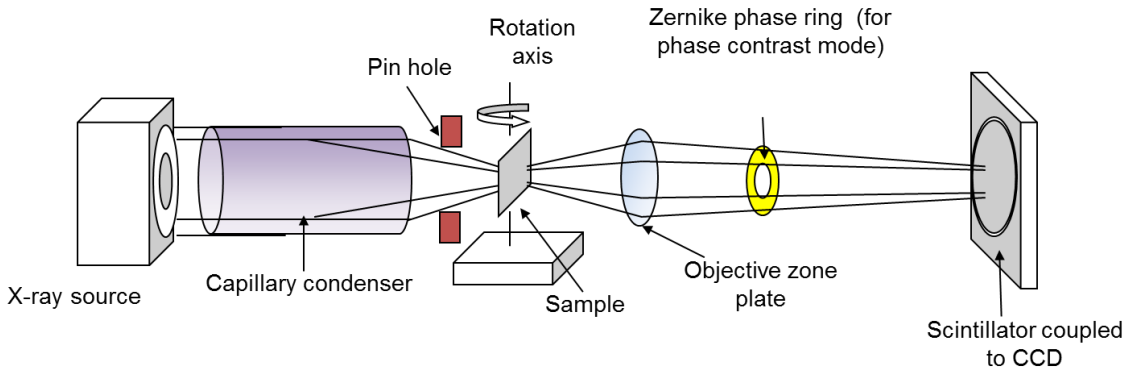

Figure 2.1. Schematic diagram of the optics train used in the nano-CT.

The nano-CT is capable of differentiating materials based on their X-ray attenuation coefficient, which is a function of the atomic number (Z) and density. This is termed as absorption contrast, some examples of which are shown in Figure 2.2(a) and (b). However, many engineering materials, including fuel cell specimens, have elements with low atomic numbers (e.g. carbon, polymers, soft tissue) that yield low X-ray absorption contrast with the background or other components within the material. For improving contrast in such materials, the nano-CT uses the Zernike phase contrast ring. Figure 2.3 (a) illustrates a tomographic slice through the 3D image of a copper wire electroplated with lithium metal, and the phase contrast helped distinguish the Li layer from the surrounding air. Figure 2.3 (b) shows a radiograph obtained with Zernike phase contrast which enhanced contrast at the interface between parylene and carboxy-methyl cellulose, which have very similar density and effective Z.

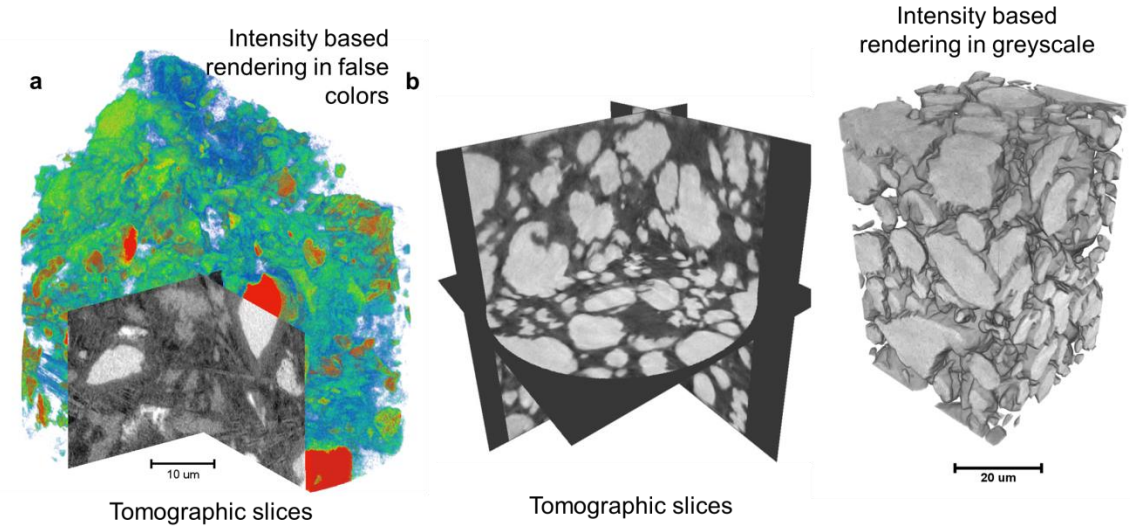

Figure 2.2 (a) 3D rendering of a portland cement sample with tomographic slices on the cut-out surface, imaged using LFOV absorption contrast mode. (b) Tomographic slices and volume rendering of Ga-In embedded silicone elastomer, imaged using LFOV absorption contrast mode [75].

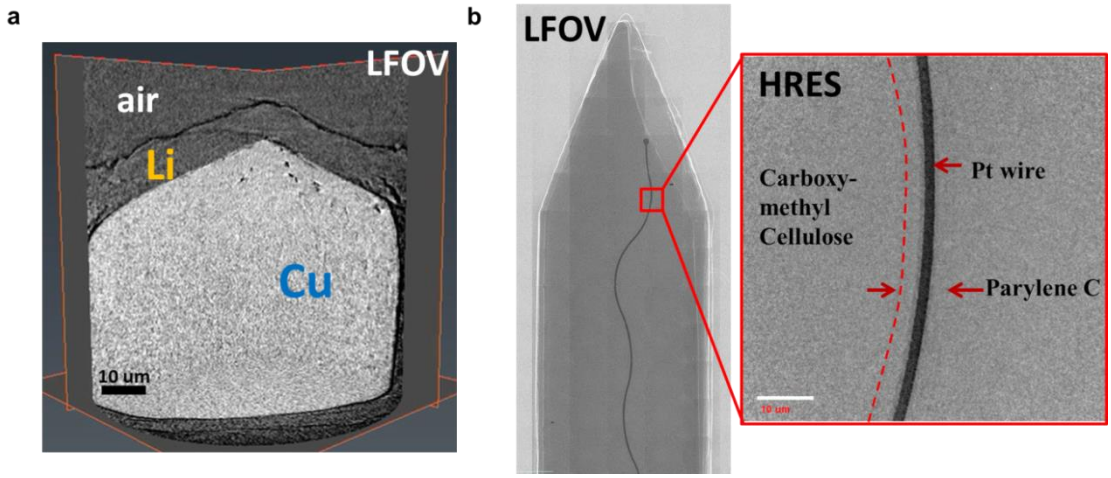

Figure 2.3 (a) Tomographic slice through 3D image of Li-plated Cu wire. (b) Radiographs of Pt wire embedded polymer sensor. Both imaged in phase contrast mode.

Although phase contrast really helps in imaging low Z materials in high-resolution, it reduces the inherent density-based and Z-based contrast to certain extent and it is associated with artifacts such as, shade-off and halo. Shade-off refers to the

diminishing intensity of the image, such that the intensities are close to that of the background, at voxels away from the edge of the material. Halo is a false edge (dark and bright pair) created at the interfaces of two phases of the material, which helps in enhancing the contrast visually. Both these artifacts (shown in Figure 2.4) pose challenge to the use of automated intensity based image segmentation tools, and necessitates development of phase retrieval algorithms for segmenting such materials for image analysis [76].

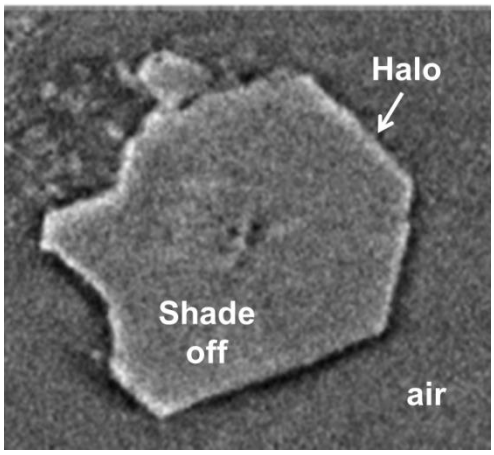

Figure 2.4. A tomography slice through the reconstructed image of a carbon-based combustion particle, showing phase contrast imaging artifacts.

On the other hand, this artifact is very useful for enhancing contrast between pores and solids, while imaging porous materials with pores with dimension of the order of and lower than the thickness of the halo, e.g. catalyst layers (Figure 2.5 (a)), porous membranes (Figure 2.5 (b)) and polymers (Figure 2.6 (a)) as well as for imaging nano-fibers (Figure 2.6 (b)). The overlapping halo from the closely spaced interfaces, creates a good contrast between the pores or within the fibers, thus making intensity based segmentation easy and robust for these materials.

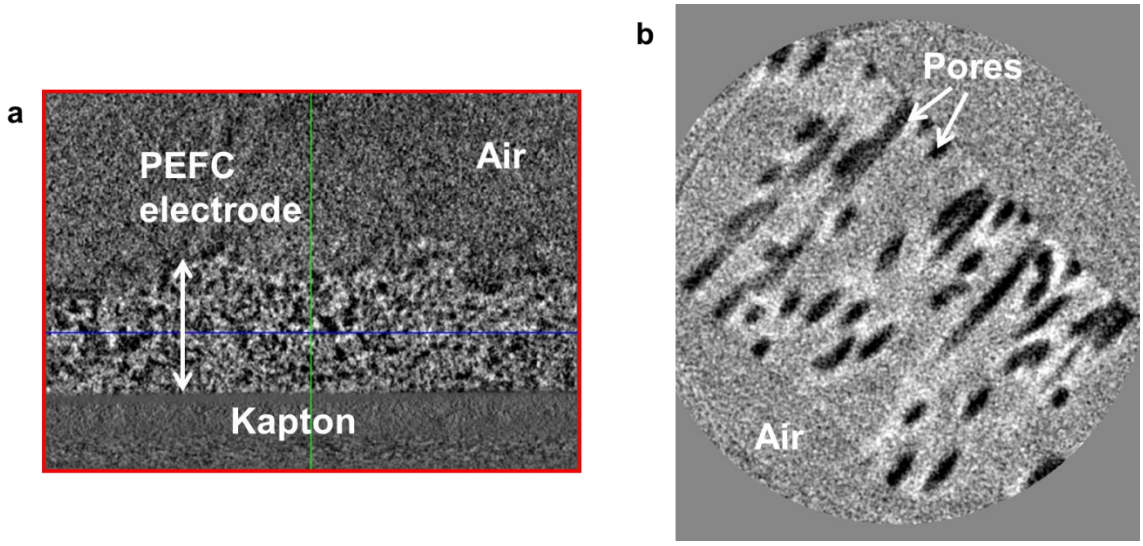

Figure 2.5. Tomography slices through a PEFC electrode (anode) (a) and track-etched polycarbonate membrane (b), both imaged in HRES phase contrast mode.

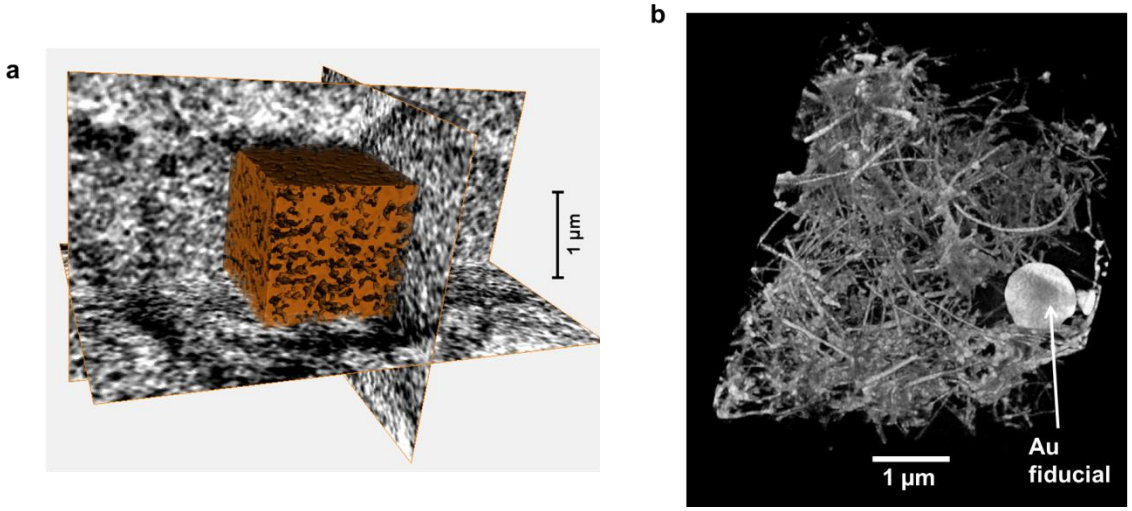

Figure 2.6. (a) Tomography slices through the imaged volume of soaked hydrogel polymer and volume rendering of the solid phase (dark pixel represent pores) [1]*. (b) An intensity based volume rendering of carbon nano-fibers (~100 nm) with PTFE binder.*

Besides, the capability of imaging materials in multi-scale by exploiting the LFOV and HRES imaging mode, another useful technique to maximize the potential of

the nano-CT, is to combine the absorption contrast with phase contrast. This is especially useful for imaging composite materials which have high density and/or high Z components along with other low density and/or low Z materials, which might or might not be porous. The absorption contrast helps in obtaining density or Z based uniform intensity in the high contrast phases, thus makes material segmentation and differentiation easy for image analysis, while the low Z materials gain enhanced contrast (in addition to high contrast in pores) in the phase contrast mode. The combined information of the two imaging modes, applied on the same volume of sample has been useful for non-platinum group metal (non-PGM) catalyst based fuel cell electrode characterization as well as for imaging Li-ion battery cathode [77], [78]. An intensity based volume rendering of the absorption contrast image and tomography slices of the phase contrast image, through the imaged volume of non-PGM electrode are shown in Figure 2.7.

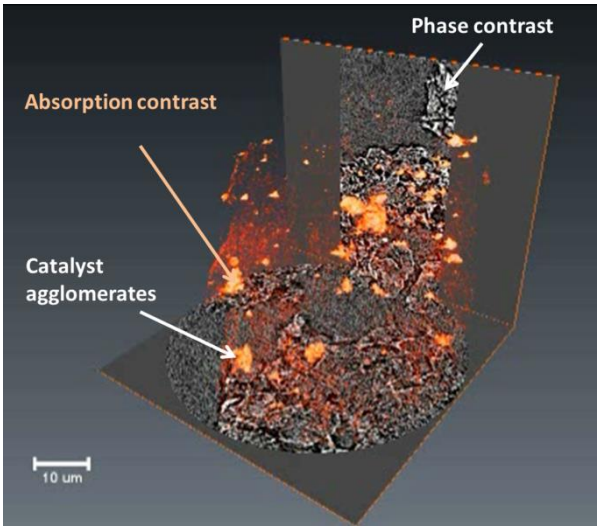

Figure 2.7. Intensity based volume rendering (LFOV absorption contrast) and tomography slices (LFOV phase contrast)

2.3. Specimen Preparation Techniques

Although the nano-CT provides a way to image internal structures of a material in a non-invasive manner, there are limitations with respect to sample size, such that the detector receives sufficient photon counts after the X-rays are transmitted through the sample. This makes preparing and mounting a specimen for imaging important. It can help maximize SNR of each radiograph and hence, improve the quality of the reconstructed 3D image. It was found that the best quality of reconstructed image was obtained when the specimen fitted in the FOV of the nano-CT, especially for composite materials. However, this can be discounted for flat samples which are much larger than the FOV in one plane and smaller than the FOV in the other [79]. Another possible cause of imaging artifact could be caused by sample drift during the scan. Sample drift can be largely controlled by using appropriate sample mounting techniques. Nevertheless, there can be small drifts (~1 μm) due to unavoidable circumstances, like stage thermal changes or some material relaxation in the sample itself. For correcting such drifts, a fiducial marker, e.g., a microsphere of a material with high X-ray attenuation (such as gold), can be used (Figure 2.6 (b)). A single (or sometimes a few) fiducial marker can be placed, by electrostatic or van-der-Waals interaction, in the FOV on the sample surface using a microspore equipped with micro-manipulator before starting the tomography scan. The center of the circle (projection of the sphere) can be tracked through all the radiographs and thus any sample-drift can be corrected before reconstructing the 3D image. This usually leads to a small decrease in the reconstructable volume of the sample. A fiducial marker is highly recommended for imaging samples in HRES mode, because of the high resolution required of the image and also for samples which are prone to volumetric

changes due to thermal and humidity changes. The latter also requires optimization of the tomography scan time such that the imaging time minimizes the chances of big sample drifts. A well-controlled environment in the nano-CT room and pre-equilibrated sample also reduces the possibility of sample drift. A drift caused by material relaxation outside the field of view, causing displacement of the sample volume can be corrected; however, any volumetric changes within the imaged volume cannot be corrected using a fiducial marker. A few techniques of sample preparation and mounting have been described in the following sub-sections for different types of materials.

2.3.1. Fuel Cell Electrodes

PEFC electrodes are porous network of Pt/C nano-particles. The catalyst nanoparticles and the ionomer film thickness are smaller than the resolution limit of the nano-CT, however the pores, which are of the order of 100 nm, are resolved by the HRES mode. A simple method of imaging the structure of an electrode in its pristine state is by using a piece of an inert but rigid film like Kapton®, which is popularly used as a decal substrate before transferring the electrode to the PEM. If one assumes that, the structure of the coated layer does not vary through the thickness (which might not be true when drying of the catalyst ink on the substrate is fast), one can chip off or scrape off a small part of the layer and mount it on a pin (1 cm tailors' pin) tip using epoxy such that the vertex is towards the top, which can be imaged using HRES phase contrast mode. The pin can be bent, such that a thin sliver will nearly fit into the 16 µm FOV [5].

A second method of mounting the sample is, to cut a triangular piece of the Kapton® coated with the catalyst layer (using fresh stainless steel blades) and gluing it

onto a pin tip (to be mounted on the sample holder). Then the pin tip can be bent, such that the catalyst layer would be on the top when the pin is mounted onto the sample holder (pin vise or the clip type holder). The tip of the triangle can be centered in the FOV and imaged. The sample will be prismatic and for a clean-cut triangle, the apex should always fit in the FOV.

The third and more robust method of preparing a PEFC electrode for imaging is to cut out a pillar using a high-precision laser-mill (QuickLaze 50ST2, ESI®) and mounting it on a flattened (by filling) tip or the head of the pin. This method is especially useful for MEA samples, where the electrode is coated onto the PEM. This method was used for the preparing sample for the images that are shown in Chapters 4, 5 and 6. A small 0.5 mm × 0.5 mm specimen was extracted from the MEA and then mounted onto Kapton® film fixed on a flattened pin-head using silver-epoxy composite adhesive (regular epoxy tends to flow and solidify around the edges of the sample and occlude the electrode volume close the membrane surface; and it makes imaging of PEFC anodes, which are usually thin and of the order of 5 μm, very difficult), such that the electrode was the topmost layer [14]. The electrode was then ablated with a low energy laser beam of 355 nm ultraviolet wavelength, leaving only the pillar-shaped electrode with diameter of approximately the size of the FOV (preferably a few microns larger, so that the ablated surface remains outside the FOV) on the membrane surface. The pillar-shaped anode specimen was made such that most of the volume of the specimen remains in the FOV for all nano-CT radiographs. The same method can be used for imaging an electrode coated onto a Kapton® film.

A major challenge in imaging the anode on a PFSA ionomer membrane (such as Nafion®) is specimen drift due to volumetric changes of the membrane as well as curling of the edges of the piece of the membrane during the scan, due from the inherent sensitivity of the PFSA ionomer membrane to even small changes of the ambient humidity. To minimize the possibility of edge curling, after ablating the anode catalyst layer around the pillar specimen, a sharp razor blade was used (with extreme care) to cut off the extra membrane around the pillar under a stereo microscope, leaving approximately 100 µm ×100 µm square piece of MEA with the anode pillar on the pin. Nafion® (membrane with thickness of 25 µm and higher) was difficult to ablate using the low power laser beam used to ablate carbon based electrode. The same was observed with PTFE membranes, which could not be ablated using the laser. In order to correct for minor specimen drift during computational reconstruction, spherical gold and silver nanoparticles were used as fiducial markers.

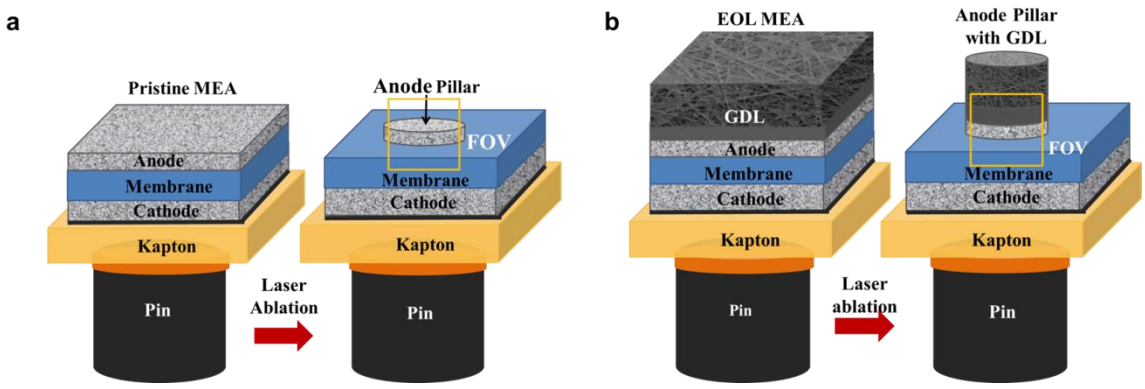

Figure 2.8. Schematics of sample preparation and mounting for imaging PEFC electrodes, on MEAs in pristine state (a), and for post-mortem analysis (b) [14].

In the case of post-mortem analysis of degraded cells (discussed in Chapter 5 and 6), where the MEA has 5 layers (PEM, electrodes and corresponding GDLs), the GDL

was detached from the side, which was not being imaged and that side was placed on the Ag-epoxy layer. Leaving the GDL intact on the electrode being imaged, allows one to investigate any possible changes at the GDL-electrode interface along with the membrane-electrode interface. The same method of laser-ablation to make a pillar-sample was used for this MEA. Figures 2.8 (a) and (b) show schematics of the sample preparation for the pristine (just the CCM) and an MEA (with GDL on the electrode) specimens, respectively

In the case of using laser ablation for preparing samples for nano-CT out of a Nafion® membrane with electrodes coated on both sides, there is an additional step required to obtain a robust sample. When the piece of MEA (or CCM) is glued on to the flat Kapton® film and the electrode on the top surface is ablated. The electrode on the epoxied surface ablates as well because the Nafion® is fairly transparent to the laser. This causes the sample to sit loose on the support film. Hence, after the sample preparation, the piece of MEA (after cleaving off the extra membrane around the pillar-sample) can be transferred onto the flattened pin surface (with or without a small piece of Kapton® support film, which ensures a flat platform for the sample) coated with Ag-epoxy as the final step. The manipulation can be done using fine-tipped tungsten needles while working under a stereo-microscope.

The laser ablation technique (to form pillar samples) has also been useful for fast sample extraction from solid-oxide-fuel-cells (SOFCs). A green laser beam, which ablates metals and ceramics, is used in this case. Unlike in a PEFC, the components of an SOFC are rigid and have ceramic based (i.e. high X-ray attenuation) materials. This requires the sample size to be smaller than the FOV of the nano-CT in order to increase

transmission of X-rays through the sample and maintain good signal-to-noise ratio (SNR) in the images. FIB-lift out has been popularly used [80], [81] for extracting samples for nano-CT; however, the process is usually time consuming and cost-intensive.

2.3.2. Thin-film and Membranes

The major challenge with mounting thin-film samples for imaging is that they are prone to sample drift (either due to its own weight or motion induced by the drift within the nano-CT. Films that are fairly rigid can be mounted as a triangular piece onto the clip-type sample holder or glued onto a pin, which is then mounted using the pin-vise or clip-type sample holder. However, films that have thickness ~10 µm (such as the track-etched polycarbonate membrane/filter, shown in Figure 2.5 (b)) are prone to sample movement during the scan. A way to impart rigidity to the sample is to cut a small piece out of the membrane, such that the ratio of thickness to characteristic length is ~1:10; e.g., a 6 µm film can be cut into a ~100 µm triangular piece and mounted on a pin, such that only ~50 µm of the film stands free on the top. Another way of imparting rigidity is by rolling the piece around the pin tip about its vertex such that the tip part will still have a flat region to fit into the 16-65 µm FOV. A fiducial marker is always wise to use in these cases of imaging flimsy samples.

2.3.3. Dispersed Particles

In order to image dispersed particles to analyze their morphology, a suitable substrate is required to mount the particles on. Kapton® film, which is rigid as well as low X-ray attenuating material, is a good candidate for depositing particles for tomography.

In most cases, an electrostatic (or van-der-Waal's) interaction is sufficient for the particles to adhere to the substrate. This method was used for imaging dispersed catalyst ink to image individual agglomerates that constitute a PEFC electrode (e.g., Figure 3.4). Diluted catalyst ink was deposited on a 25 μm Kapton® film and allowed to dry; then a triangular piece of the film was mounted for imaging. In a few cases, radiographs (moasaic) of an extended area had to be obtained, in order to find a FOV highly populated with the particles to be imaged, so as to obtain a statistically significant number of particles. The region-of-interest (ROI) might not necessarily be at the vertex of the triangle, which ensures a smaller sample size and a better quality image. However, in case of imaging dispersed particles, which are deposited on a substrate without much intricate structure, such as Kapton® film, a sample size much larger than the FOV in one of the dimensions does not negatively affect the image quality. It is however necessary to use a substrate that has very low X-ray attenuation. Another example of imaging particles on a large substrate is shown in Figure 2.9 (b), where a Kapton® mesh was used to trap combustion particles of certain size. The same mesh was mounted on the nano-CT sample holder to image particles trapped on it. One of the particles imaged in the on the mesh is shown in Figure 2.4.

The nano-CT has also been successfully used for imaging materials that are much larger than the FOV in the planar direction, while having a thickness that fits in the FOV, and have enough photon counts registered on most of the radiographs recorded through a full 180° rotation of the sample. In some cases a few projections have very low SNR (the ones which have X-rays passes through the full length of the broad sample), which can be eliminated from the set of images used for computational reconstruction of the 3D image.

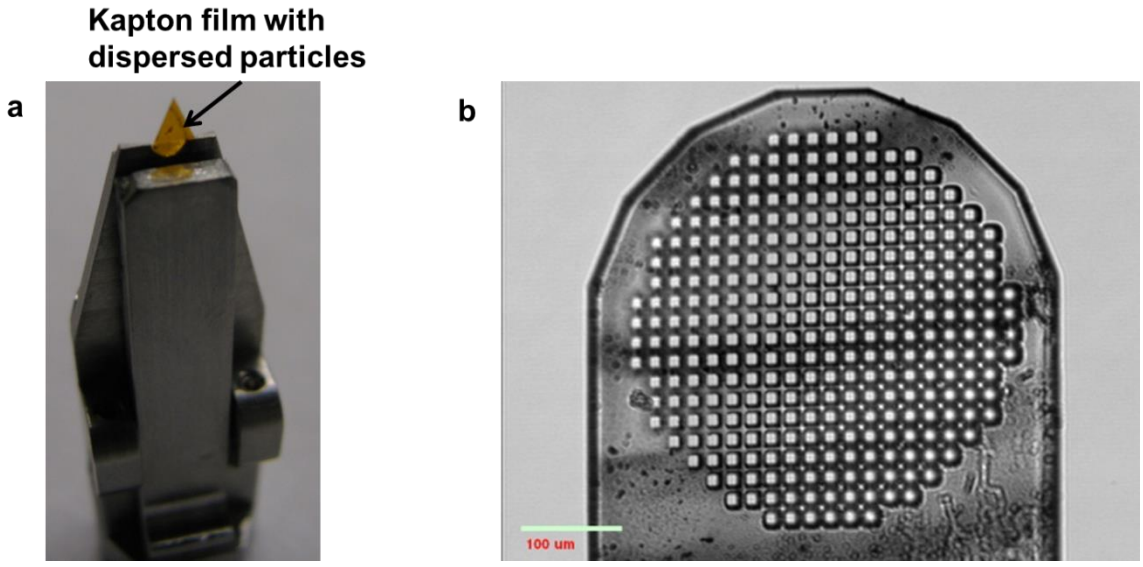

Figure 2.9 (a) A clip-type sample holder with a triangular piece of Kapton® film with dispersed catalyst particles. (b) A Kapton® mesh used for trapping combustion particles to be imaged using nano-CT.

2.3.4. *In-situ* Imaging and Samples Requiring Controlled Environment

The nano-CT provides an ambient imaging environment; hence, it can accommodate special environmental chambers in which samples can be mounted for imaging. This also enables us to perform in-situ and in-operando imaging. The image of the hydrogel sample shown in Figure 2.6 (a) was recorded with the hydrogel soaked in water to prevent the pores from collapsing as the sample dries [1]. A piece of hydrogel was introduced into a Kapton® capillary tube, with an inner diameter of 1 mm and 25 µm thick wall, filled with water. Both the ends of the capillary were sealed using silicone sealant. The capillary was then glued onto a pin with their axes parallel and the hydrogel was imaged as it was suspended in water. Some gold particles were sprinkled onto the

piece of hydrogel before placing it in the capillary, in order to help us track and correct for any sample movement during the tomography scan. A similar capillary mount was used for imaging the liquid metal-silicone composite shown in Figure 2.2 (b). In this case, the elastomer was cured within the capillary, in order to avoid any alteration to the morphology of the liquid-metal globules within the elastomer that could have been caused by shear stress of cleaving/cutting the elastomer to the dimension of the FOV of the nano-CT.

Capillary based set-ups have also been useful for developing *in-situ* experimental environment for the nano-CT. A flow-through cell set-up was developed for imaging water imbibition within a porous catalyst layer packed within a capillary with inner diameter ~50 μm (in order to image in HRES mode that will resolve the meso-pores within the catalyst layer). An image of the flow through cell is shown in Figure 2.10 (a). However, there was a challenge towards obtaining a good catalyst packing within the micro-capillaries. An example of incomplete catalyst packing within a polycarbonate capillary is shown in Figure 2.10 (b).

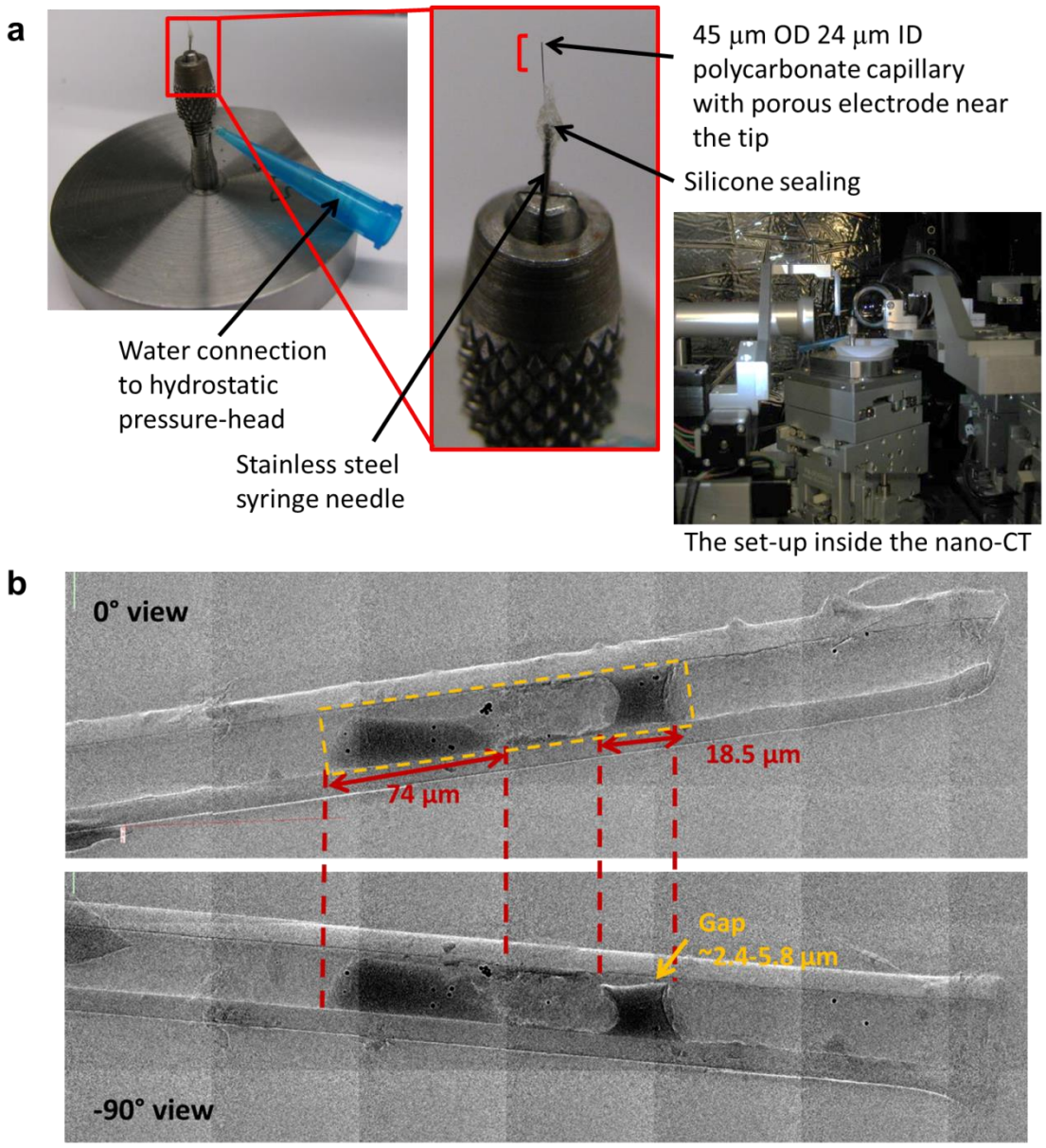

Figure 2.10 (a) Images of the flow-cell set-up mounted on nano-CT sample holder. (b) Radiographs of polycarbonate micro-capillary with incomplete catalyst layer packing.

A set-up for an in-operando study of dendrite growth in a metal-ion battery was also developed by housing two wire-electrodes in an electrolyte filled Kapton® capillary. To make the set-up robust and flexible, high-pressure fittings were used on either side that was used to feed in electrolyte and replenish it, when required. An I-shaped beam

was used to support the steel-tube fittings using magnetic mounts. The thin metallic section parallel to the capillary did however obstruct the view of the ROI (tip of the metal wire, i.e. the electrode). While acquiring images over 180° rotation of the sample, it led to 10% missing projections because of the beam. However, the 3D image could still be reconstructed using the software provided by Zeiss (formerly Xradia Inc.), and the 3D image quality can further be improved by using advanced reconstruction algorithms [82], [83]. An image of this set-up is shown in Figure 2.11 (a), and radiographs of the Cu dendrite at a few time intervals during potential cycling of the *in-situ* cell are shown in Figure 2.11 (b). This set-up will be used for 4D-CT (time-resolved 3D images during in-operando studies) to investigate the failure of batteries due to dendrite growth and develop control strategies [84].

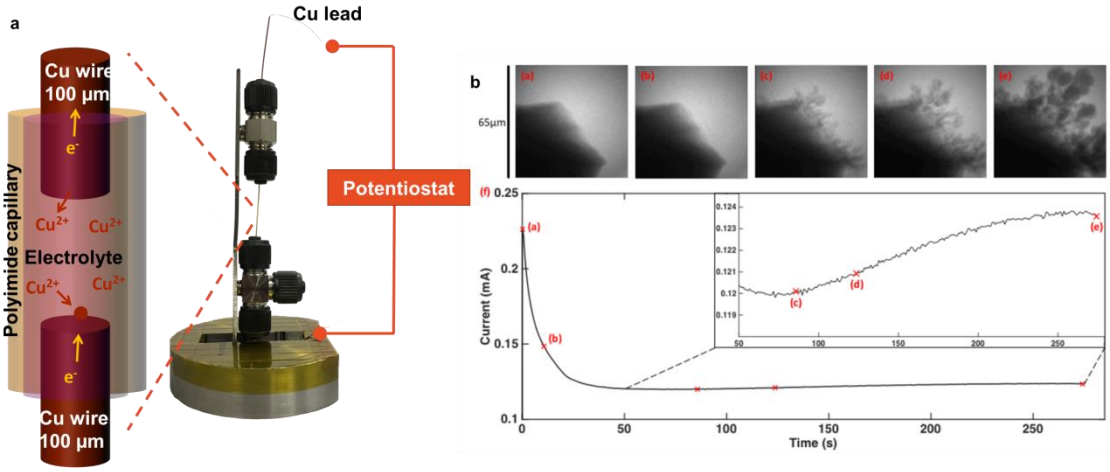

Figure 2.11 (a) Image of the in-situ metal-ion battery set-up along with a schematic of the capillary-based cell. (b) Radiographs showing growth of Cu dendrite in-situ, during potential hold at 0.7 V. The plot at the bottom shows the current measured and the time-stamps of the radiographs are marked on the plot.

2.4. Conclusion

The nano-CT with 8 keV X-ray source and equipped with optics for high-resolution and phase contrast is very versatile to image a varied range of composite materials comprising of low attenuating components like polymers and carbon to high attenuating materials like metals and ceramics. X-ray CT is a tool, popularly used in industry to perform non-destructive failure analysis, at macro to nano-scale. The non-invasive imaging also enables *in-situ* and *in-operando* studies as well as allows further material analysis using other tools for extensive material characterization. Besides image acquisition and reconstruction to obtain a 3D image, image segmentation and image analysis is also important to extract useful information of the image data and characterize morphology of materials imaged. All these techniques need to be developed and advanced hand-in-hand, to make the most efficient use of the tool and technique for scientific advancement in various fields.

Chapter 3

Structure-Performance Relationship of PEFC Electrodes

3.1. Introduction

High loadings of expensive platinum catalyst in PEFC cathodes increase cost and hinder commercial competitiveness. Unfortunately, achieving a desired mass activity of the catalyst is challenged by the mass transport resistances imposed by the electrode structure [85]. There exist many prior theoretical and numerical modeling studies on the cathode catalyst-layer microstructure to understand the ionic, electronic and mass transport processes in the electrodes and their effect on PEFC performances [86]. One common model to predict oxygen transport loss is the agglomerate model [87], [88], which resolves the coupled oxygen diffusion and oxygen reduction reaction within the composite volume of the Pt/C/ionomer agglomerate phase. A key result of the agglomerate model is the increased mass transfer losses with larger agglomerates [19], [88]. However, there is a deficit of direct experimental validation of these models. In this study, the effect of electrode morphology on PEFC performance has been experimentally

validated. The electrode morphology was analyzed from 3D imaging of the cathode catalyst layer as well as from 3D imaging of individual agglomerates formed in electrode ink itself, using the nano-CT. Nano-CT has previously been used in imaging of PEFC catalyst layers to quantify porosity, pore and solid phase size distributions [19], [89], [90] and to evaluate the effects of agglomerate size distribution on the predictions of the agglomerate model for the catalyst layer [88]. The 3D imaging of the electrode and the dispersed agglomerates presented here, provide insight into the electrode architecture and any inherent anisotropy in the solid aggregate structure and in the pore network that collectively impact the complex transport processes in the electrode. Electrochemical testing of fuel cells using the same electrodes, reported hereinafter, further assists in direct correlation of electrode morphology and overall PEFC performance.

3.2. Electrochemical Diagnostics

3.2.1. Electrode Fabrication

The PEFC electrodes were fabricated using a catalyst ink composed of carbon black supported Pt catalyst (Pt/C: HISPEC4000® grade, Johnson Matthey, UK) mixed with ionomer solution (Nafion® D521 grade, DuPont, USA) with deionized (DI) water and isopropanol (IPA) in a 1:1 ratio as the dispersion media [12]. The same initial catalyst ink was used to prepare two batches of electrodes by first manually painting a predetermined volume of the ink onto GDLs, in a single coating step, and then drying them at ambient conditions for 24 hours. The first batch of electrodes (B1) were fabricated using the catalyst ink, which had been stirred for 24 hours on magnetic stirrer.

The second batch (B2) was made using the catalyst ink which was ultrasonicated for 10 minutes, in addition to 24 hour of stirring. The two 1 cm^2 GDEs from each batch were heat-pressed onto a polymer electrolyte membrane (Nafion®-115) to prepare the MEAs. The catalyst loading on the cathodes and anodes of both the batches were ca. 0.66±0.02 mg_{Pt}/cm^2. Each MEA was assembled in a cell hardware (designed for 5 cm^2 cells) using incompressible gaskets of fiber-glass reinforced PTFE films of predetermined thickness, such that the GDLs are compressed by 20%.

3.2.2. Experimental Protocol

The electrodes were otherwise identical except for an additional sonication step of the ink used to fabricate them. Both set of electrodes were tested using the same protocol. The cell was conditioned for 8 hours at 80°C and 100% relative humidity to activate the cell components and obtain stable measurements. All the electrochemical measurements except the CV were done at the same conditions. The cell was left overnight, which provides time for the ionomer membrane and the electrodes to mechanically equilibrate. The next morning, the cell was heated up to 35°C and CV was performed on the cathode by scanning through potentials from 0.04 V to 0.9 V at a scan rate of 40 mV s^{-1}. The CVs were repeated for 10 times, until the signal stabilized to the same curve. During CV, the cell was supplied with 100% water-saturated H_2 to the anode and N_2 to the cathode at a rate of 0.1 slpm (which was the lowest stable flow rate obtained using the test stand). Next, the cell and humidifiers were heated up to 80°C, while being held at OCV with the reactant gases being supplied to the electrode: H_2 for anode and air for cathode. The polarization curves were measured coupled with EIS measurements (with 5% voltage

perturbation amplitude used and frequency of 10 kHz to 100 kHz, which gave us an estimate of the high-frequency resistance, i.e. Ohmic resistance) at every voltage steps. The performance of the cell was measured in potentiostatic mode. The voltage steps used were such that the activation regime had closely spaced voltage steps (with 5 min residual time till 0.8 V) after which steps of 0.2 V were used down till 0.2 V (with 10 min residual time). Constant flow rates of 0.1 slpm was used for both air and H_2, with a back pressure of 50 kPa (i.e. operating pressure of 1.5 atm). The gas flow and temperatures were controlled using the fuel cell test stand (FCT-150S, Bio-Logic, France) and the electrochemical measurements were done using a potentiostat (VSP, Bio-Logic, France).

3.2.3. Electrochemical Characterization

The polarization curves and the power density plots are shown in Figure 3.1. The plots have been corrected for Ohmic overpotential. The current values (and the power density values) plotted in the polarization curve (and power-density curve) were averaged over the last one minute of the potential-holds and the standard deviations are shown as error-bars. The Ohmic resistance in the system (ionic and electronic) was calculated from the high-frequency impedance values at all the I-V measurement points. The performance of both the electrodes was identical at the activation regime. The ECSA values of platinum in the cathodes, measured from CVs of both kinds of MEAs were also found to be similar at 30 ± 4 m^2_{Pt}/g_{Pt}. The difference in performance shows up in the mass transport regime, which indicates that the difference in performance is primarily due to differences in diffusion characteristics of the cathode, which is directly related to the morphology of

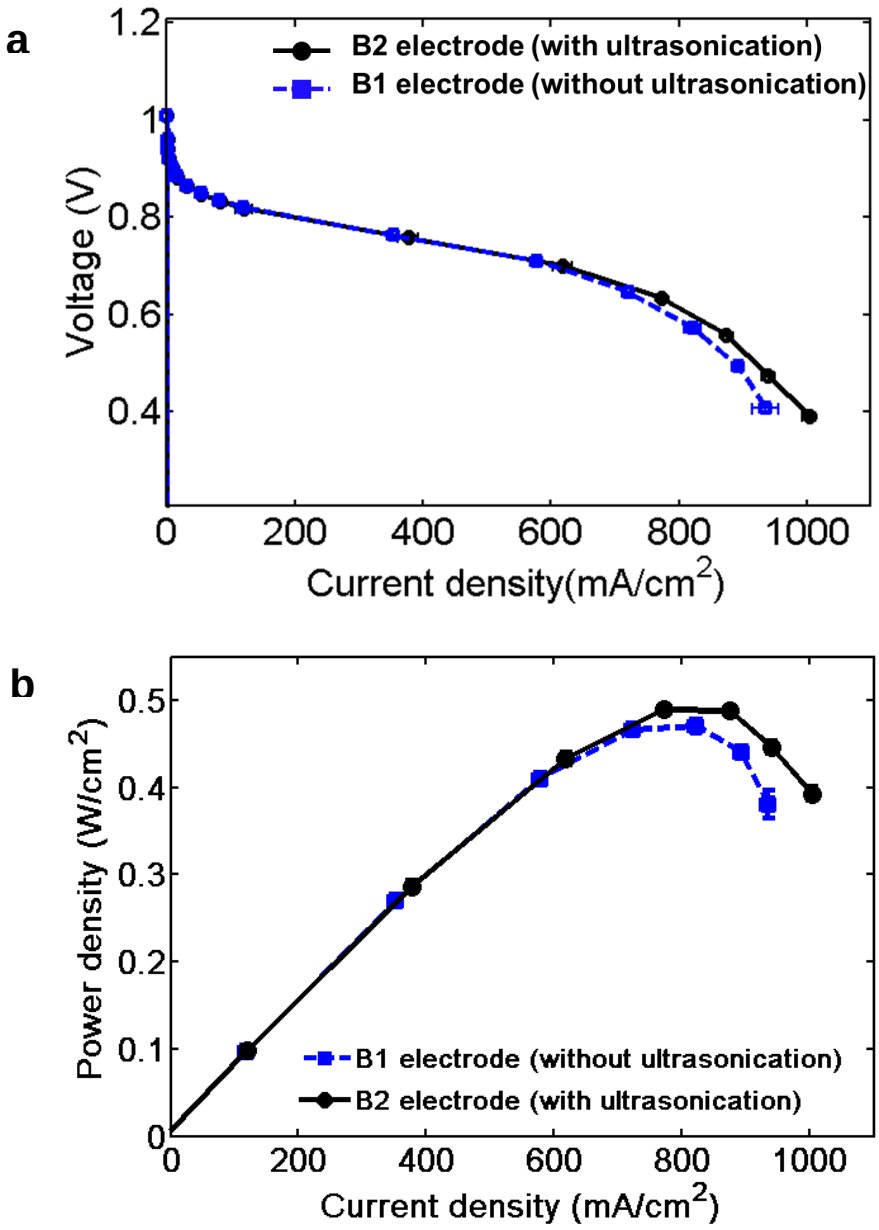

Figure 3.1. Polarization curves (a) and power density plots (b) for MEAs with electrodes fabricated using catalyst ink with ultrasonication (black-circles) and without ultrasonication (blue-squares). The error bars show standard deviation in the measured current density values.

the respective electrodes. The ultrasonicated catalyst layer has better transport properties due to better dispersion leading to smaller agglomerates (details are discussed in the next section).

3.3. Morphological Analysis

Samples for 3D imaging using nanoscale X-ray computed tomography (nano-CT) were obtained by painting the two batches of catalyst ink on polyimide (Kapton®) films. The catalyst layer was taken from the polymer film so that the GDL's microporous layer that has similar morphology as the catalyst layer would not be accidentally included in the imaged volume. The images were recorded in Zernike Phase contrast mode that provided high contrast between the pore phase and the solid phase (Pt/C/ionomer), as seen in the raw tomography slice in Figure 3.2(a). The images of the two kinds of catalyst layers were normalized to the same range of intensity after they were cropped to a volume within the sample. After segmenting the images into pore and solid phase, shown in Figure 3.2(b), we used a morphological separation algorithm to split the solid phase into interconnected solid domains, which we consider to be the catalyst agglomerates, shown in Figure 3.2(c).

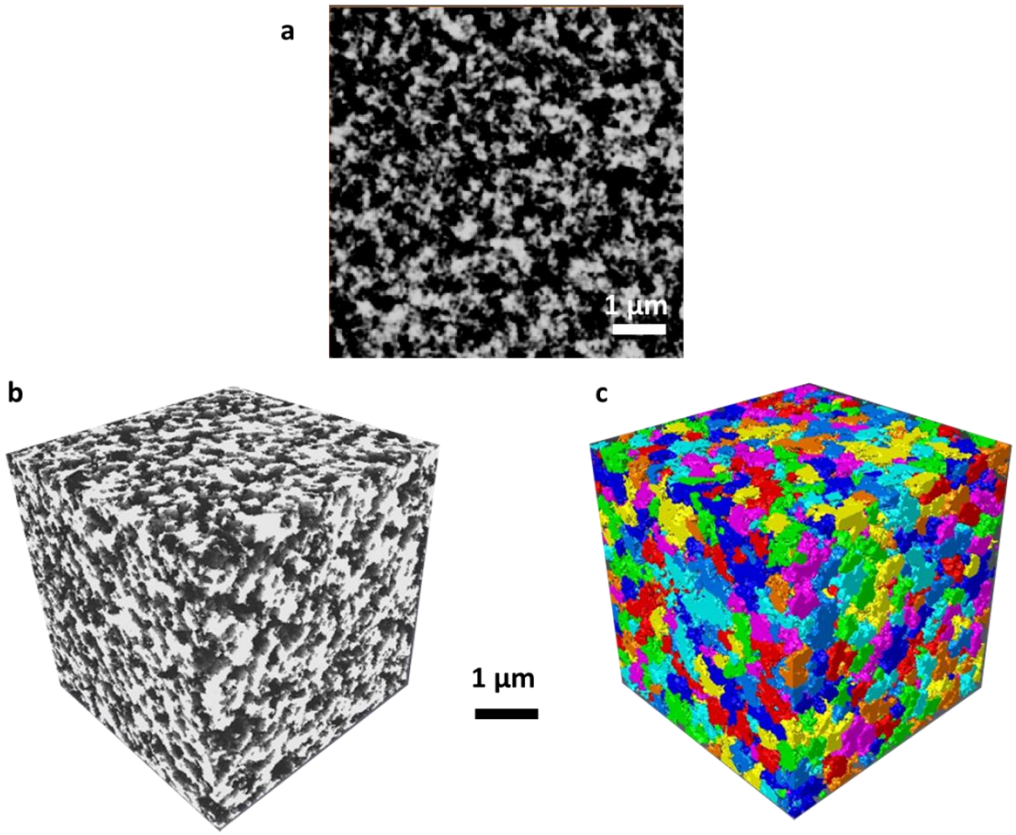

Figure 3.2. (a) Raw tomography slice through the imaged electrode. The brighter pixels represent the solid phase, and the darker pixels represent pore phase. (b) 3D volume rendering of a cropped volume of the imaged electrode segmented into solid (Pt/C/ionomer, shown in grey) and pore phase (shown in dark grey or black). (c) The volume rendering of the solid phase with the agglomerates separated and labeled as different colors.

The same intensity threshold was used on both the nano-CT images of the electrodes and morphological separation with the same parameter was applied to deconstruct the solid network into constituent agglomerates. The image analysis was performed using commercial software (Avizo Fire^{TM}, FEI). Figure 3.3 shows the size distribution of agglomerates based on effective diameter (calculated using $d_{eff} = 6V / A$;

where V and A are the volume and surface area of each labeled solid domains from the images). The B1 electrode shows a larger percentage of larger agglomerates, whereas the distribution is skewed towards smaller particle sizes for the B2 electrode. The porosity was computed to be 49% for both the samples. The porosities being similar, the poorer performance of the B1 electrode in the mass transport regime was not due to through-plane transport in the catalyst layer but due to increased mass transport loss within larger agglomerates arising from the increased oxygen diffusion distance to the Pt within the agglomerate interiors, as suggested by the agglomerate model [87], [88].

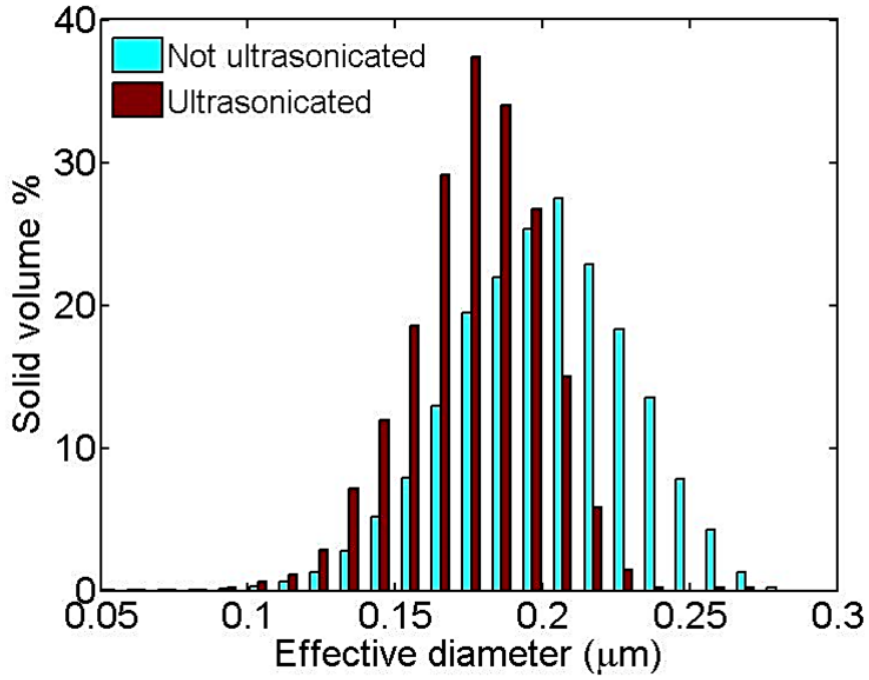

Figure 3.3. Size distribution of agglomerates in the catalyst layer of the two kinds.

We have also imaged the agglomerates in the dispersed phase obtained by drying a diluted catalyst ink on a Kapton® film to verify the agglomerate structure and size resolved using nano-CT against the corresponding 2D image using SEM. The dispersed agglomerate shapes and sizes were consistent with the ones obtained from the electrode

image as shown in Figure 3.4. The majority of agglomerates were found to have effective diameters ranging from 100-350 nm. Zoomed-in images of few agglomerates are shown in Figure 3.4(c). There were a few agglomerates captured in the dispersed layer, which might be a combination of a few smaller agglomerates.

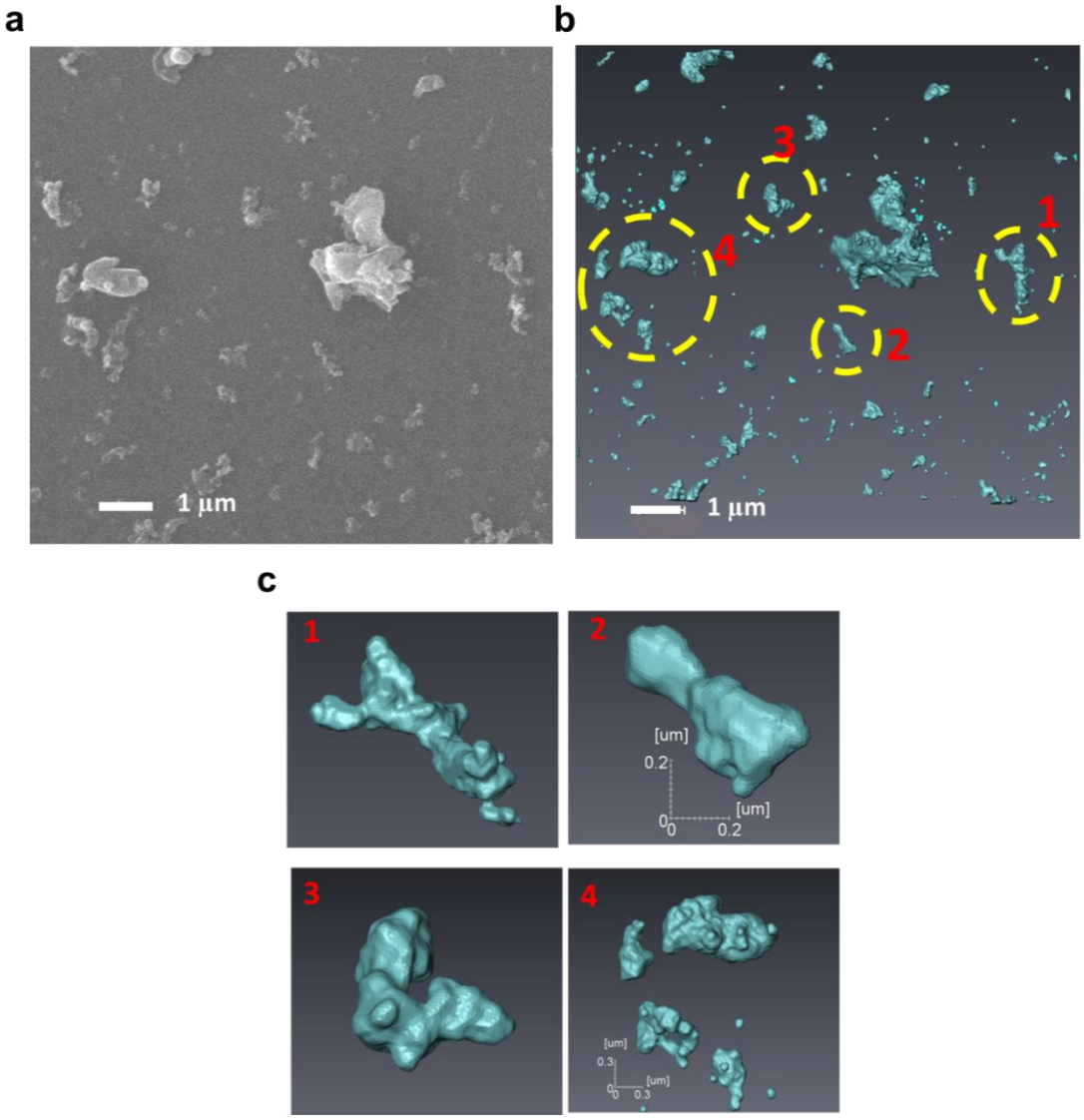

Figure 3.4. (a) SEM image of the dispersed catalyst ink on a Kapton® film (sputtered with 20 nm of gold). (b) 3D rendering of segmented agglomerate on the same region on the Kapton® film with dispersed catalyst ink, imaged using the nano-CT. (c) Zoomed in images of a few agglomerates present in the FOV of (a) and (b).

The agglomerate model gives us an estimate of the effectiveness factor of the catalyst layer, which can be defined as the ratio of the actual reaction rate to the ideal reaction rate, if transport was infinitely fast. It has a strong dependence on the size of the agglomerates, especially at higher overpotentials, i.e. at lower voltages or higher currents. The model assumes the agglomerates to be spherical with a uniform ionomer film on its surface. To compare our results to the agglomerate model, we used the volume averaged effective diameters of the two types of electrodes as the inputs and obtained the values of current density for both kinds of electrodes. The percentage difference in the power (or current density) generated by the cells with different representative agglomerate size in the cathodes: obtained from the model, and from the polarization curves, are plotted against the cell voltages in Figure 3.5. The experimental data is fairly consistent with the predictions of the model, implying the significance of nanoscale morphology of the electrodes. An increment in percentage loss in current density for the larger agglomerates with decreasing cell voltage is observed, indicating a higher contribution from smaller agglomerates at a high current operation, as reported by researchers earlier [88].

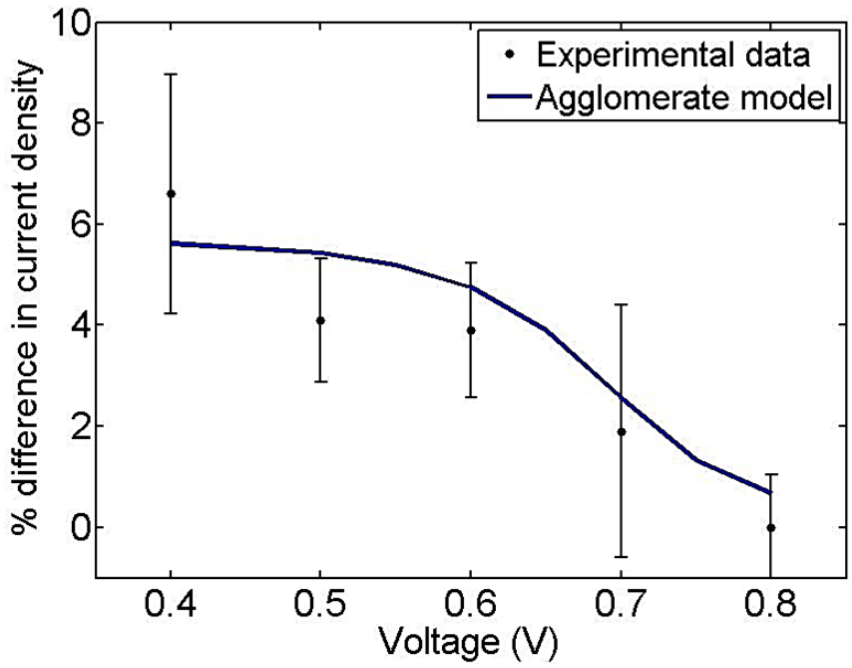

Figure 3.5. Validation of agglomerate model against the experimental data.

3.4. Discussion

In order to ensure high utilization of the expensive Pt catalyst, the electrode architecture has to be conducive to fast transport, including protonic, electronic and gaseous transport to the catalyst sites. High utilization of catalysts will lead to a decrease of catalyst loading, as per the DOE 2020 cost targets for a fuel cell stack for automotive application. However, as the Pt catalyst loading decreases, and with smaller agglomerate sizes, more surface area is created: the ionomer-catalyst interfacial resistances become more dominant [91]–[93], which limits the maximum power output of the cell. An alternative to developing low cost fuel cell stack for FCEVs is to eliminate precious metal based catalyst altogether and using non-precious metal catalyst in the cathode for ORR [78], [94]. [78].

3.4. Conclusion

The role of electrode microstructure in the maximum power output of the fuel cell has been elucidated in this chapter. The agglomerate model analysis demonstrated in this chapter provides some confirmation of the agglomerate model approach for modeling and simulating microstructural transport losses. The actual structure of the electrode, obtained using nano-CT can be used as a direct input to the computational analyses to study the electrochemical performance of a fuel cell coupled with the transport phenomena. This approach has also been useful for analysis the hierarchal structure that is found in the thick non-PGM cathode catalyst-layers. The correlation of electrode microstructure and catalyst agglomeration with the catalyst utilization and electrode performance has been implemented for elucidating the degradation mechanism in fuel cells, as has been described in the following Chapters of the dissertation.

Chapter 4

Degradation due to Cell Reversal

4.1. Introduction

A very severe cause of PEFC degradation is called “cell reversal” and it can result from partial to complete fuel starvation. Hydrogen starvation at the anode can arise from a malfunction of the hydrogen supply system or hydrogen passage blockage by foreign impurities, water flooding or ice formation (during winter) in the pores and/or in the fuel supply lines [33], [95]. Hydrogen starvation could be exacerbated when FCEVs are operated under transient conditions such as start-up and rapid load change (i.e. high accelerating conditions). Any delay in response of the fuel supply system under such conditions can lead to an insufficient amount of hydrogen reaching the anode. This has usually been observed to affect the cells downstream in a cell stack [65]. When the anode of a particular cell in the stack is starved of hydrogen, the anode is unable to perform the HOR to produce enough electrons and protons to support the load. The cell instead goes into a capacitive charging mode, where the other cells in the stack drive current through the starved cell. Thus, the anode of the starved cell has alternate reactions being driven in

order to produce electrons and protons and thus complete the load circuit. Initially, the anode undergoes the water electrolysis reaction with Pt catalyzing the reaction, but soon after, the carbon corrosion reaction takes over. The latter causes the anode to consume itself to sustain the load demand. The loss of carbon support causes collapse of the electrode structure: It causes Pt nanoparticles to agglomerate, hence reduces the electrochemical active surface area. Carbon corrosion also changes the hydrophobicity of carbon particles, collapses pores in the electrode and causes delamination at the membrane-electrode interface. Under prolonged hydrogen starvation, the carbon in the micro-porous layer of the gas diffusion layer can also be oxidized and lost. The high overpotentials of these reactions produce a lot of thermal losses. Local hydrogen starvation can lead to hot spots in the MEA, resulting in pin-holes through the membrane and GDL, shorting the two electrodes. The high potentials also aggravate ionomer degradation [52], [53], [57]. Thus, if cell reversal is not interrupted, it causes catastrophic cell failure. This would mean, a car will stop in the middle of highway traffic if such an event occurs, making it very dangerous for commercial implementation. However, severe hydrogen starvation events are rare. Nevertheless, a single event is enough to damage a fuel cell stack, thus indirectly increasing the lifetime cost of a FCEV.

The phenomenon of cell reversal caused by hydrogen starvation is sometimes confused with degradation phenomena at the start-up/shut-down of a fuel cell [48], [96]–[98]. During a fuel cell start-up, air is present in the anode and, if the air is not completely flushed out of the anode by hydrogen, before drawing power out of the cell or stack, an air-fuel boundary is formed at the anode, which in turn causes a spatial rise in potential in the cathode, resulting in carbon corrosion at the cathode until the air in the anode is

completely consumed or replaced by hydrogen. The same is true during shut-down, when the hydrogen supply to anode is terminated, after which ambient air fills the pores and supply lines of the anode. In both of these cases, the degradation due to carbon corrosion occurs at the cathode causing loss of Pt ECSA for the ORR, along with changes in hydrophobicity of carbon support and pore structures, interfering with the cell performance. Certain robust control strategies have been proposed, that can prevent a formation of an air-fuel boundary, thus eradicating degradation during such transients encountered in regular fuel cell operation [51], [99]–[101].

In this chapter, the electrochemical phenomena of cell reversal resulting in carbon corrosion at the anode are described.

4.2. Cell Reversal

When a current is drawn though a fuel cell starved of hydrogen, the water electrolysis reaction (oxygen evolution reaction: OER, Eq. 4.1) and carbon oxidation reactions (carbon corrosion reactions, Eqs. 4.2 and 4.3) are driven in the anode to produce electrons and protons. Both of these reactions are non-spontaneous, they consume energy from the fuel cell stack, i.e., the starved cell is consuming power instead of producing power. The thermodynamic equilibrium potential of water electrolysis reaction is 1.23 V. This leads to an increase in anode potential (E_{An}) relative to the cathode potential (E_{Ca}) until the cell potential (E_{Cell}) reverses ($E_{Cell} = E_{Ca} - E_{An} < 0$ V). Although the equilibrium potentials for carbon corrosion reactions are low, due to sluggish kinetics (high activation barriers), they usually set in when the electrode potential is above 1 V [33], [95], [102]–[105]. The negative cell potential resulting from hydrogen starvation at the anode is

termed cell reversal. A typical cell reversal response from a conventional PEFC is shown in Figure 4.1. The cell potential was found to become negative when the anode was starved of hydrogen. The first few seconds of starvation was accompanied by water electrolysis. Then the voltage plummeted down (i.e., the anode half-cell potential shot up) and carbon corrosion became the major reaction to sustain the load current. The load was terminated when the cell potential reached -2 V to prevent catastrophic failure of the cell. It is clear that, if the current load was higher than 0.2 A cm^{-2}, which was used for this particular test, the voltage reversal time (i.e. the starvation sustenance time) would have been much shorter.

$$2H_2O \leftrightarrows O_2 + 4H^+ + 4e^-,\ E^o = 1.232\ V\ (vs.\ SHE) \qquad [4.1]$$

$$C + 2H_2O \leftrightarrows CO_2 + 4H^+ + 4e^-,\ E^o = 0.207\ V\ (vs.\ SHE) \qquad [4.2]$$

$$C + H_2O \leftrightarrows CO + 2H^+ + 2e^-,\ E^o = 0.518\ V\ (vs.\ SHE) \qquad [4.3]$$

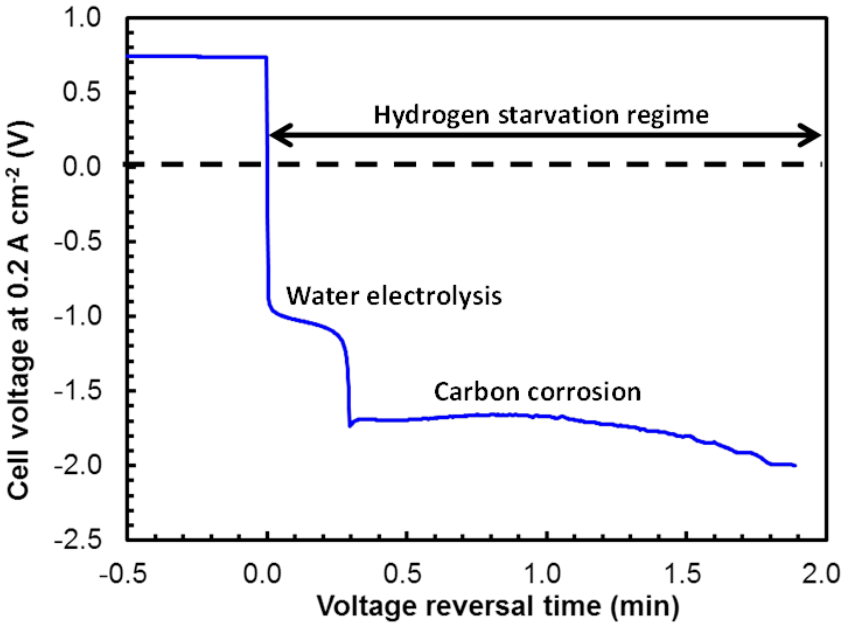

Figure 4.1. Cell voltage reversal of a conventional MEA with Pt/C anode.

Cell voltage reversal does not only bring the stack power output down but also causes severe and irreversible damage to the cell. The excessive heat generated and high potential can lead to pin holes in the electrolyte membrane, causing the MEA to be electrically shorted, eventually leading to catastrophic cell failure [33], [95], [104] unless the rise of the anode potential is intentionally stopped or delayed through system control strategies, such as cell voltage and exhaust gas monitoring [105], [106], flushing of the anode compartment with excess hydrogen to eliminate accumulated nitrogen and/or water, which have been employed on FCEVs over the last decade [107]. These electronic controls are, however, prone to faulty outputs and the best control strategy to control degradation due to cell reversal is a materials-based solution [33], [104].

4.3. Reversal Tolerant Anode

The existing concept for a materials-based solution involves adding a water electrolysis catalyst, i.e. an OER catalyst into the PEFC anode. This helps prolong the water electrolysis stage during hydrogen starvation and, in the process, prevent the anode half-cell potential increase beyond 1.8 V. Thus, the driving potential for carbon corrosion is maintained at a minimal value and the cell is protected from self-consumption of the anode while fuel-starved under load demand. These anodes are termed Reversal Tolerant Anodes (RTA). Figure 4.2 is a schematic of a cell reversal phenomenon, in the presence and absence of an RTA. RTAs reported in the literature use a variety of OER catalysts, such as IrO_2, RuO_2, TiO_2, $Ir_xSn_{1-x}O_2$, PtIr, IrRu, PtIrRu, etc. [33], [104], [105]. For this study, IrO_2 was selected as a representative model catalyst because it is known to be the most stable and active OER catalyst [108], [109]. Most of these catalysts have precious

metals as their major component, which makes RTAs expensive. FCEVs typically use a large-sized stack consisting of several hundreds of unit cells employing MEAs with an active area of several hundred square centimeters [110] and implementation of RTAs would increase the cost of these systems.

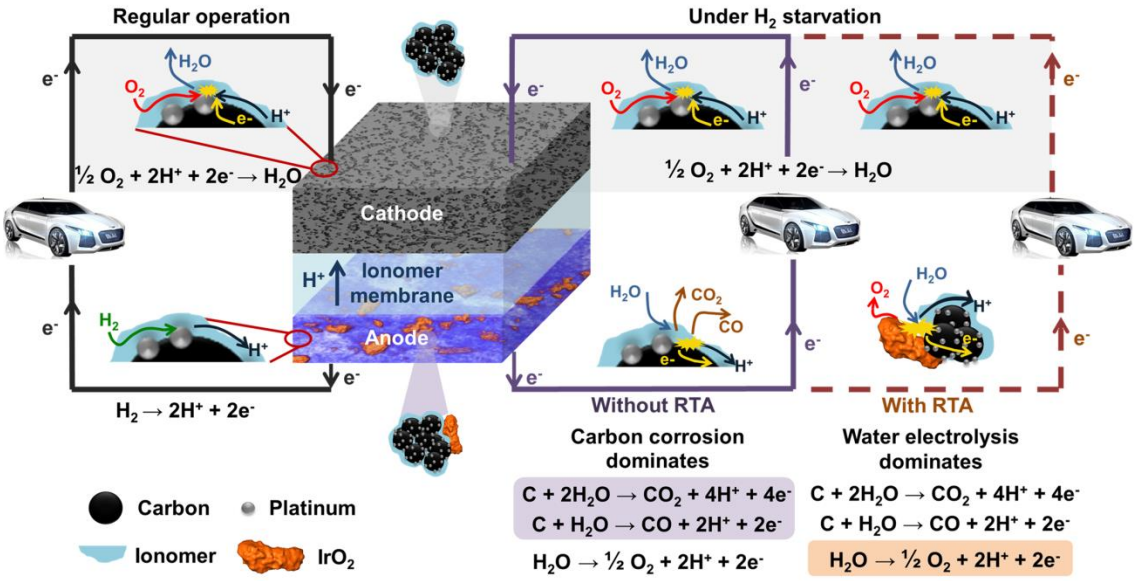

Figure 4.2. Schematic showing the major electrochemical reactions in a PEFC under regular operating condition and under hydrogen starvation condition (with RTA and without RTA).

This increasing durability of PEFCs along with cost optimization for automotive application necessitates a detailed fundamental understanding of cell reversal phenomena and degradation mechanisms to maximize the effectivity of the additional catalyst and/or enhanced cell design. Detailed studies on MEAs with RTAs and their performance and limitations will be discussed in the following Chapters.

Chapter 5

Effectiveness of Reversal Tolerant Anodes

5.1. Introduction

Addition of an OER catalyst into the electrode can ensure protection for the susceptible carbon catalyst support. An alternative strategy to adding an OER catalyst to the anode is to add voltage monitoring devices for each fuel cell in the stack to keep track of a reversed cell (i.e. a cell with depleted hydrogen supply) and bypass the current load to prevent further damage of the cell due to reversal. However, implementation of such a control system complicates the system design and also increases the lifetime maintenance cost. Moreover, electronic controls can be erroneous and any delay in response can still lead to permanent damage to the anode. Therefore, it is imperative to come up with a simpler robust method for mitigating the degradation. Adding a material that can spontaneously enhance the rate of the harmless OER reaction in hydrogen starved conditions, controlling the anode half-cell potential to low value, until sufficient hydrogen supply is resumed, at the anode is a robust strategy to prevent the catastrophic

failure of a cell. An analogous method has also been widely implemented at the cathode to protect the carbon support from corrosion during transience of start-up/shut-down and in open circuit conditions.

As discussed earlier in Chapter 1, the cost of a fuel cell stack is a barrier towards FCEV being a commercial success. Introduction of additional catalyst, which is mostly based on precious metals like iridium, further increases the cost of fuel cell MEAs. Thus, it is important to understand the mechanism of degradation due to cell reversal, the role of the OER catalyst in an RTA, and its effectiveness in that role. This will enable cost efficient and effective design of electrodes that will be less susceptible to degradation. With this objective, we have simulated well controlled cell reversal conditions for lab scale single MEA tests and performed in-situ electrochemical diagnostics and ex-situ morphological characterizations on the MEAs to elucidate the degradation phenomena and the role of RTA. The following section describes the details of the experimental procedure followed by discussion of the experimental observations and image analysis.

5.2. Electrochemical Diagnostics

5.2.1. MEA Fabrication

The MEAs used in the study were fabricated in the Hyundai Fuel Cell R&D facility. Nafion® 211 was used as the polymer electrolyte membrane (i.e. ionomer membrane) and the catalyst-layers were coated onto either sides of the membrane using the decal transfer method [13], [111] using a Kapton® film as the decal surface. The catalyst layers were fabricated with a carbon-supported platinum catalyst having 40 wt%

Pt (Pt/C: HISPEC4000® grade, Johnson Matthey, UK) and an ionomer binder (Nafion® D2021 grade, DuPont, USA) dispersed in a solvent based on DI water and IPA. The ionomer content in the electrode was 30 wt% with respect to the total solid content of a dried electrode. The Pt loadings of anode and cathode were 0.1 and 0.4 mg cm^{-2}, respectively. This implies that the anode catalyst layer was thinner than the cathode catalyst layer.

The water electrolysis catalyst, IrO_2, was synthesized by the Adams fusion method [112], [113]. The amount of IrO_2 in an anode was varied to be 5 and 50 wt%, with respect to the amount of Pt catalyst in the anode; i.e., the RTA 5 wt% MEA contained 0.005 mg cm^{-2} of IrO_2 and the RTA 50 wt% contained 0.05 mg cm^{-2} of IrO_2. The IrO_2 nanoparticles were mixed with the Pt/C catalyst and ionomer dispersion to make the catalyst ink, which was then coated onto the decal surface and transferred onto the ionomer membrane to form the reversal tolerant anodes. A TEM image of the IrO_2 used in the catalyst ink is shown in Figure 5.1.

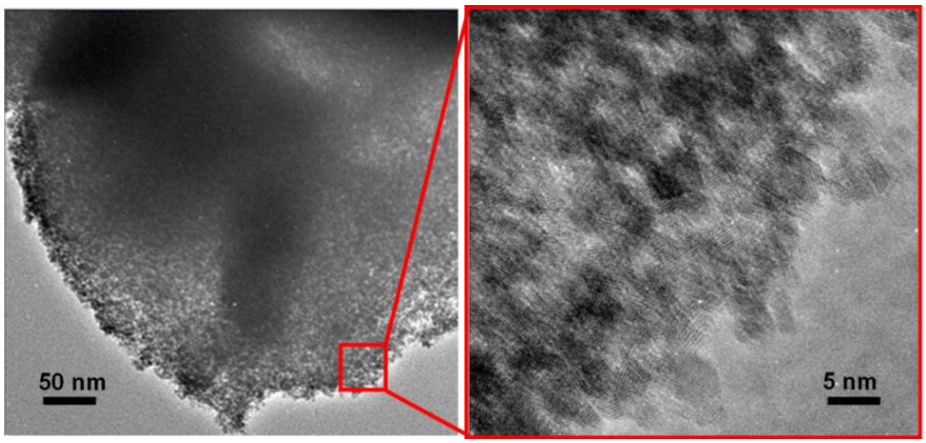

Figure 5.1. TEM image of an aggregate of IrO_2 nanoparticle synthesized using Adam's Fusion method. On the right is a higher resolution image (zoomed into the region marked in red on the left image) showing individual IrO_2 nanoparticles with particle diameter of ca. 5 nm.

Commercially available gas diffusion layers (25 BC GDL, SGL Carbon GmbH), which has microporous layers, were used for both the anode and the cathode. The catalyst coated membrane (CCM) and gas diffusion layer (GDL), on either sides of the cell were housed between two graphite bipolar plates, which had a serpentine flow channels (0.5 mm deep; 1 mm width). Non-compressible fiber-glass reinforced PTFE sheets were used as gaskets for both the anode and the cathode, such that the GDL compression was nearly 20%. The cell hardware was manufactured by Scibner Associates Inc.

The CCM obtained from Hyundai Research Laboratory were of 25 cm^2 area and we used 4 cm^2 MEAs by cutting 4 square pieces of the larger MEA and preparing the sub-gasket out of 25 µm Kapton® films with adhesive backing, such that 4 cm^2 of MEA area remained unmasked.

5.2.2. Experimental Procedure

We measured the beginning-of-life (BOL) polarization curves under a regular reactant gas supply (i.e., hydrogen at the anode and air at the cathode with flow rates of 0.13 and 0.43 slpm respectively) after the cell was fully activated. For activation, the cell was cycled at current densities of 0.05 to 1 A cm^{-2} for 8-10 hours, until the cell potential at each current density was stable. The cell operating temperature was $65^{o}C$ and the cell was kept at 100% relative humidity (RH), for all electrochemical measurements including cell reversals, polarization, EIS, and CV. The control of gas flow, humidity, heating and measurement of polarizations and conditioning of the cell was performed using the FCT-150S Fuel Cell Test Stand (Bio-Logic, France) and the cell reversal tests, EIS and CV measurements were performed using VSP Potentiostat (Bio-Logic, France).

After completing all electrochemical measurements at BOL, we subjected the cell to cell reversal conditions by simulating an extreme case of hydrogen starvation. First, a constant current of 0.2 A cm^{-2} was drawn from the cell while supplying sufficient hydrogen to the anode and air to the cathode. Then the hydrogen supply was switched to nitrogen after 0.5 min. The initial cell voltage (under hydrogen supply) was approximately 0.8 V. On replacing hydrogen by nitrogen, the cell voltage began to decrease gradually (still staying positive) until the residual hydrogen was used up. Then the cell potential sharply dropped to a negative voltage and plateaued at around -1.1 V (i.e. E_{An}~ 1.9 V), which has been attributed mainly to water electrolysis with traces of carbon corrosion [102], [114], [115]. This is followed by another decrease in potential and a, second plateau around -1.7 V (i.e. E_{An}~ 2.5 V) was observed, which represents the

major carbon corrosion regime [114]. A voltage cut-off of -2.0 V was used, to prevent the cell potential from plummeting down further, which can result in permanent cell failure, disallowing one to take electrochemical measurements at partially degraded states. The temporal voltage change in a conventional MEA (i.e. RTA 0 wt%) is depicted in Figure 5.2 (which is also Figure 4.1). The time for the cell voltage to reach from 0.0 to -2.0 V is defined as a voltage reversal time (VRT). After each reversal test, the cell was flushed with nitrogen (both anode and cathode) and left it idle overnight to allow the cell components to rehydrate and equilibrate. The following day polarization curves, EIS, and CV measurements were done on the cell using the same settings as in the BOL measurements. Afterwards, the reversal test was repeated. This process was continued until the cell performance at 1.2 A cm^{-2} dropped to nearly 35 % of its BOL performance. This was considered to be the end-of-life (EOL) state of the cell.

The first reversal for RTA 0 wt% is the first uninterrupted reversal test when the cell potential hit -2 V. For RTA 5 wt% and 50 wt% MEAs, however, the first reversal time corresponds to the sum of the reversal times until the cell potential reached -2 V. For these MEAs, the reversal tests were interrupted and the load was cut off at the time stamps of the reversal tests of RTA 0 wt% and RTA 5 wt% MEAs, in order to compare the durability of MEAs with RTA to the ones without and also to compare durability of two MEAs with different loadings of the OER catalyst.

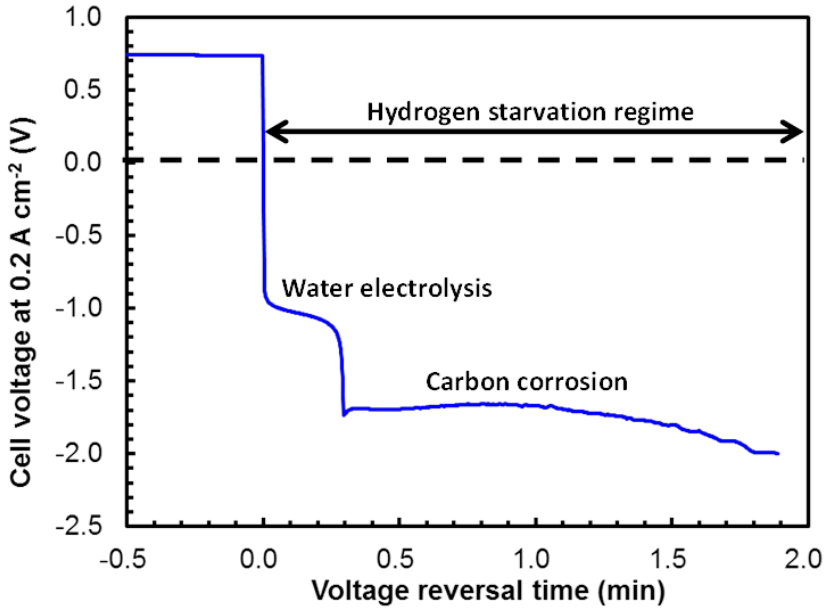

Figure 5.2. Voltage vs. time plot for first reversal of conventional MEA (i.e. MEA with RTA 0 wt%). The time has been denoted in terms of voltage reversal time (0 second corresponds to the cell potential becoming negative.)

During start-up of the cell after the end of each reversal test (which is followed by nitrogen purge through both electrodes), nitrogen was first purged through the electrodes to remove the air that would have displaced the nitrogen after the cell-shut down. Then, the cell was re-conditioned by applying loads in increasing steps for an hour. As the cell degraded after each reversal test, the maximum current load was limited such that the cell potential stayed above 0.3 V, to prevent any cell-aging during conditioning. In order to avoid any possible degradation at the cathode due to an air-fuel boundary caused by the presence of air in the anode, the nitrogen purge was essential. The hydrogen and air supplies were started five minutes before the load (or current) cycling was performed such that a stable OCV was recorded. The time for OCV hold was limited at five minutes,

thereby minimizing degradation when the cathode is held at a high potential that can itself cause carbon corrosion.

The re-conditioning was followed by recording of cell polarization in galvanostatic mode. The polarization curves were recorded 2 to 3 times (the signal was pretty stable). After polarization, EIS was performed on the cells at 0.1 A cm^{-2} and 0.4 A cm^{-2}, with an AC amplitude of 5% of the DC current and a frequency between 0.1 Hz to 100 kHz. CV was performed on the cathode to estimate the ECSA and any possible changes in the electrode and Pt/C catalyst in cathode due to cell reversal. The cell was purged with nitrogen at the cathode and hydrogen at the anode for an hour (when the OCV of the cell was nearly 0.01 V) and then then the voltage was scanned from 0.04 V to 1.2 V and back, at 50 mV s^{-1} scan rate. The CV sweeps were recorded for 30 times, such that successive CV curves overlapped. The gas flow rate was 0.13 slpm for both anode and cathode. This was followed by measurement of the anode CV, to study the changes in the anode catalyst layer. Before performing the voltage scans, the both the anode and cathode were purged with nitrogen for 30 min and then hydrogen was introduced to the cathode and nitrogen to anode and the cell was allowed to purge for 1 hour. The anode CV was then performed with 0.13 slpm gas flowrate. The long purge was required because of the large humidifier bottles within the test stand (which is equipped for 50 cm^2 fuel cells), which caused larger residual volume for the gases.

5.2.3. Electrochemical Measurement Results

The “first cell reversal” for RTA 0 wt%, 5 wt% and 50 wt% MEAs are shown in Figure 5.3(a). In the case of the RTA 0 wt% MEA, Pt/C catalyzes the water electrolysis

reaction for a brief moment until it gets deactivated and the reaction proceeds to carbon corrosion dominated regime. The duration of the water electrolysis plateau (E_{Cell} ~ -0.8 to -1.1 V) is much longer for the RTA 5 wt% and RTA 50 wt% MEAs and increases significantly with increasing amount of IrO_2 catalyst, making the MEA more durable and reversal tolerant. However, after a finite amount of time, the OER catalyst also appears to be deactivated for water electrolysis and the cell voltages of the RTA 5 and 50 wt% MEAs also plummet down to lower cell potentials, hitting the -2.0 V when the current load was removed.

After the first reversal, the successive reversal times were very short [14]. Figure 5.3(b) shows the first reversal and the second reversal (which eventually caused the cell to reach EOL) of RTA 0 wt% MEA. The first reversal has a water electrolysis regime which is lacking in the consecutive reversal test, implying that the electrolysis catalysis ceased after the first deactivation. The same phenomenon is observed for MEAs with RTA. The first voltage reversal signal and the two consecutive ones are shown in Figure 5.3(c). Even the carbon corrosion overpotential rises after the carbon oxidation plateau during the first reversal test (clearly seen in Figure 5.3(b)), resulting in fast cell potential drop to -2 V cut-off. The accumulated reversal time (ART) at each reversal is shown in the figure legends.

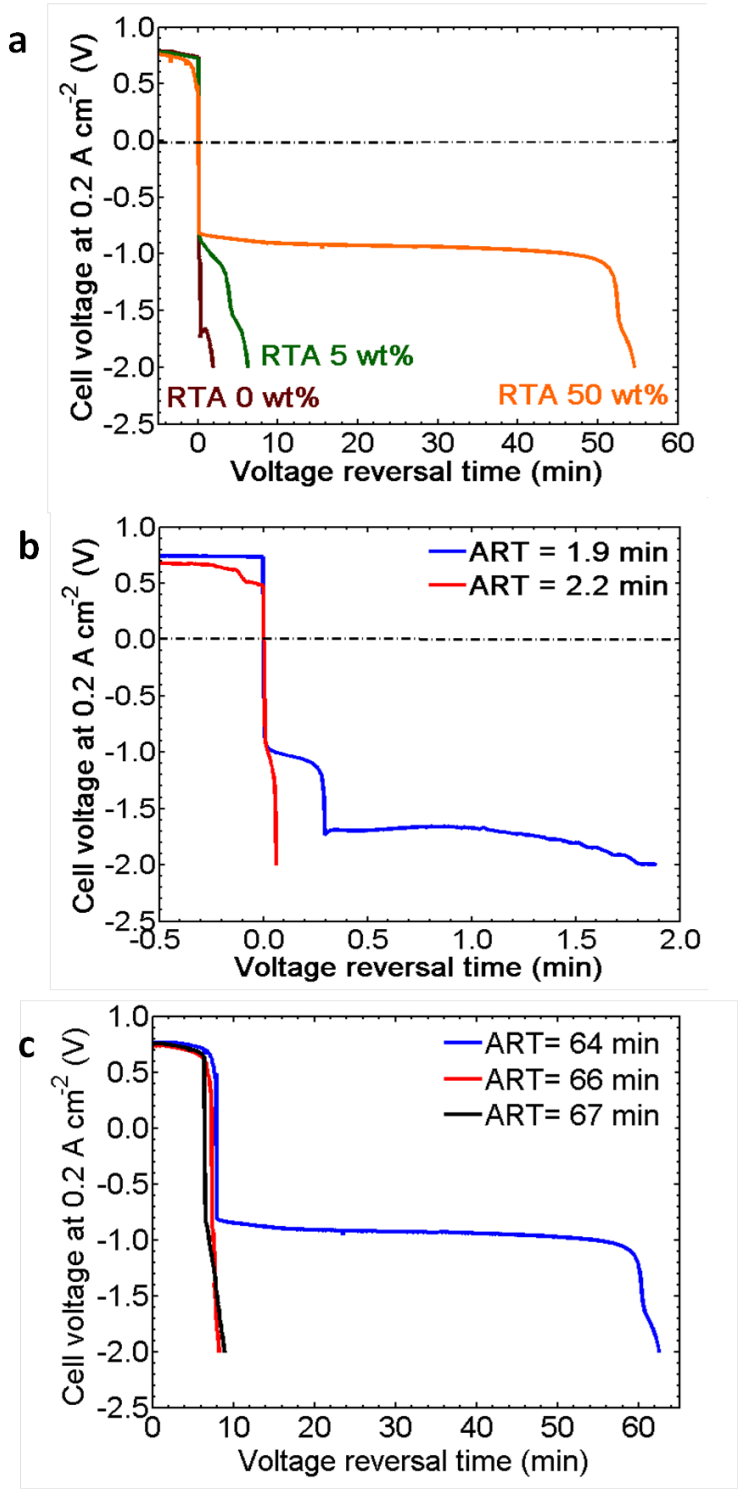

Figure 5.3. (a) First voltage reversal for MEAs with RTA (5 wt% and 50 wt%) along with MEA without RTA (0 wt%). (b) Voltage vs time plot for first and consecutive reversal tests in RTA 0 wt% and (b) RTA 50 wt% MEAs.

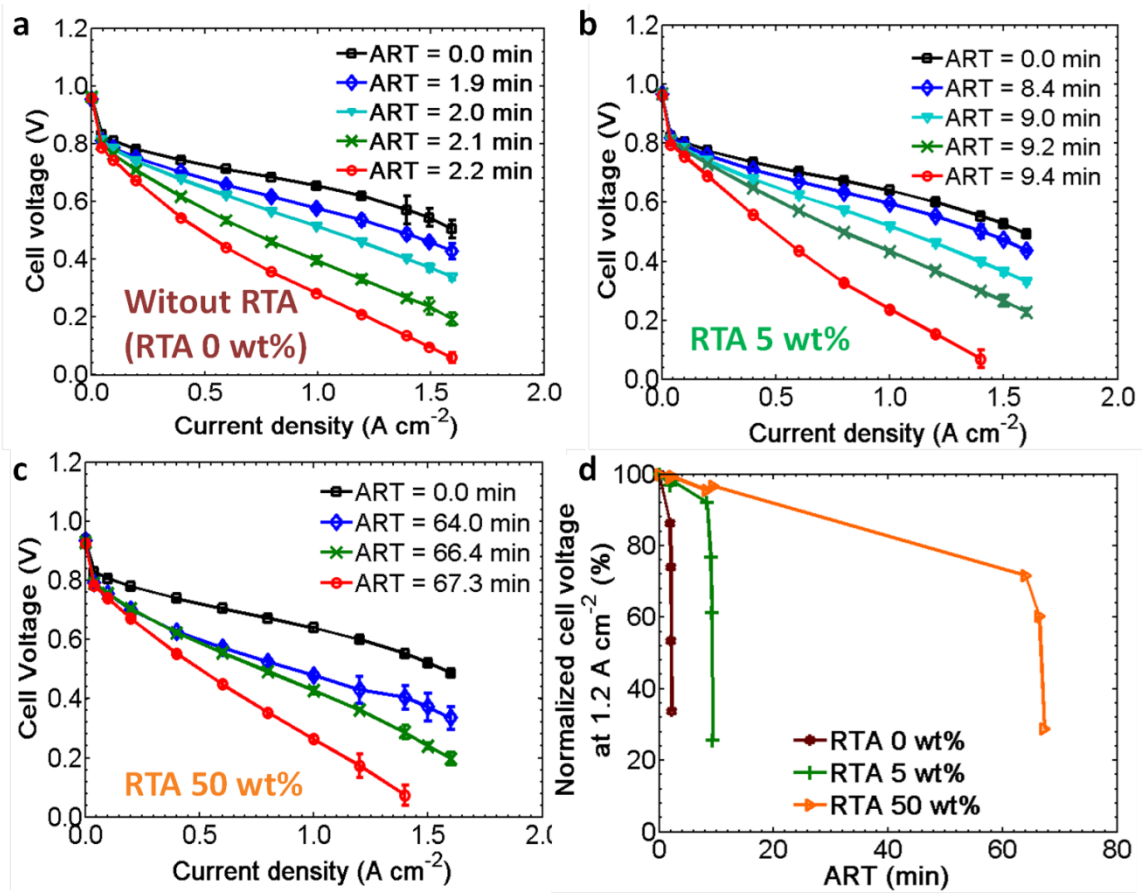

Figure 5.4. Performance degradation due to cell reversal in MEAs with RTA 0 wt% (a), RTA 5 wt% (b) and RTA 50 wt% (c) shown by polarization curves measured at BOL and after each reversal test (the accumulated reversal time, ART after which the polarization curve was recorded, is shown in the legends). (d) The cell performance is shown in terms of voltage recorded at 1.2 A cm^{-2} current shown as a percentage of BOL value for the three kind of MEAs.

The performance decay of the cell is evident from the polarization curves after the first and the consecutive reversals. Figure 5.4(a)-(c) shows the polarization curve at BOL and after first reversal test and the following reversal tests. The legend shows the accumulated reversal time after which each polarization measurement was recorded. In

Figure 5.4(d), we have plotted the cell voltage recorded at current density of 1.2 A cm^{-2} during polarization measurements vs. the reversal time (ART) as percentage w.r.t. BOL performance. This plot reflects the performance decay due to cell reversal. A similar trend in performance decay is observed in all the three cases with the difference in the time of reversal tolerance. The performance decrease appears gradual until the first reversal test, after which it accelerates with an increase in reversal time, which also corresponds to short reversal dwell time. The first reversal time (FRT) and the total reversal time (i.e. the time until the MEA reaches EOL, denoted at ERT) appears to scale with the amount of the OER catalyst in the anode, as seen in Figure 5.5.

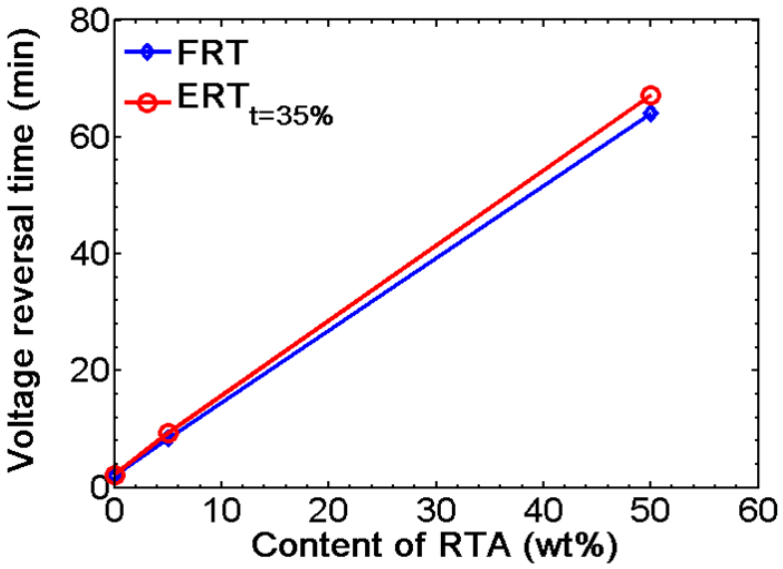

Figure 5.5. Reversal tolerance time of MEAs with different loadings of OER catalyst. FRT is the trace for first reversal test and $ERT_{t=35\%}$ is the total reversal time till EOL was reached (i.e. degradation to 35% of BOL performance).

Figure 5.6 elucidates the effectiveness of the RTA in the MEA. Figure 5.6(a) depicts the degradation rate after the first reversal time. It shows the percentage loss

(w.r.t BOL) of performance (quantified as voltage at 1.2 A cm^{-2}) after the first reversal divided by FRT. The lower the value, the better the reversal tolerance is. We can see that there is a huge benefit of adding OER catalyst from the steep drop in degradation rate from the MEA without RTA (RTA 0 wt%) to RTA 5 wt%. However, RTA 50 wt% shows only 2.2 times lower degradation rate than RTA 5 wt% in spite of having 10 times the amount of OER catalyst. Figure 5.6 (b) depicts the overall or average degradation rate due to cell reversal. It is the percentage loss of performance measured at EOL (measured as voltage loss at 1.2 A cm^{-2} at EOL w.r.t BOL divided) divided by the total reversal time. The overall degradation rate due to cell reversal decreases sharply from RTA 0 wt% to RTA 5 wt%. The OER catalyst at 50 wt% shows improved utilization as the reversal tests were repeated. The degradation rate was found to be 8 times lower than that of the RTA 5 wt% MEA. It indicates that the utilization of OER catalyst is higher at lower loading of OER catalyst during the first occurrence of cell reversal, while with repeated stress conditions, the utilization of the available OER catalyst in higher loading RTA increases to a certain extend.

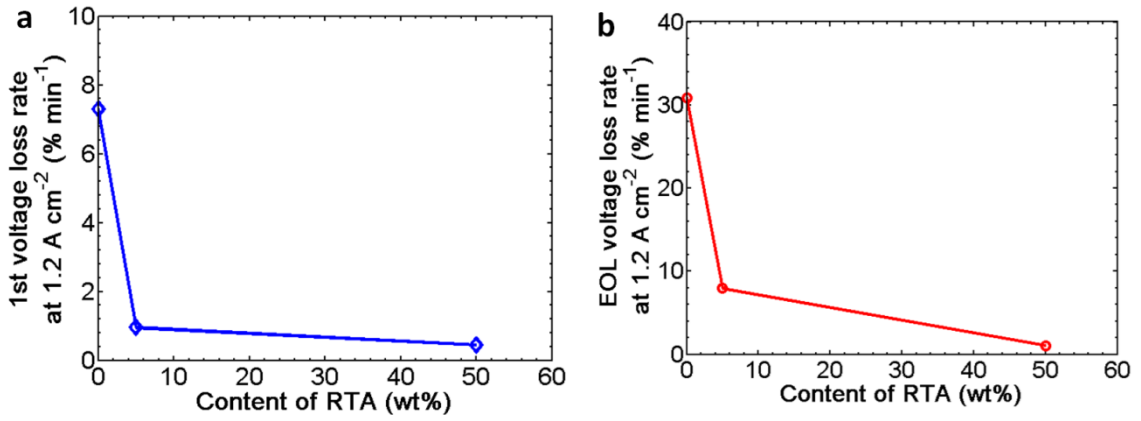

Figure 5.6. Cell performance degradation rate due to cell reversal after first reversal test (a) and average degradation rate over the total reversal time (b).

The degradation rate after the first reversal test is a very crucial durability quantification parameter for a fuel cell MEA, because it determines the fate of the fuel cell stack when it faces fuel starvation for the first time, and it also determines the time that can be allowed before actively mitigating the fuel starvation, so that the cell does not meet sudden death. In a practical application of a fuel cell stack for FCEV, a 20% loss in performance is considered end-of-life and the stack is replaced. Hence a short duration of cell reversal leading to cell degradation can be very detrimental to the lifetime of the stack and hence the cost.

EIS was performed at BOL and after every reversal tests. Fig. 5.7(a)-(c) are the EIS data obtained at 0.1 A cm^{-2} (activation regime) for each MEA. The Nyquist plots for EIS, recorded at BOL, after the first reversal and at EOL are shown in each plot. A significant increase in Ohmic resistance (R_{Ohm}) was observed, along with the increase in anode (R_{an}) and cathode (R_{ca}) charge transfer resistances. The values of R_{an} and R_{ca} were estimated by fitting the experimental data to a simple equivalent circuit model [15] (also described in Chapter 1). The magnitude increase of the resistances w.r.t. BOL resistances is shown in Fig. 5.7(d)-(f). All the resistances show a trend similar to that of the voltage degradation profiles with reversal time, with the increase in Ohmic resistance specially matching the sudden drop of performance (i.e. sudden increase in resistance) after the first reversal test. Thus, the increase in Ohmic resistance can be considered to be a major contributor to the cell performance decay.

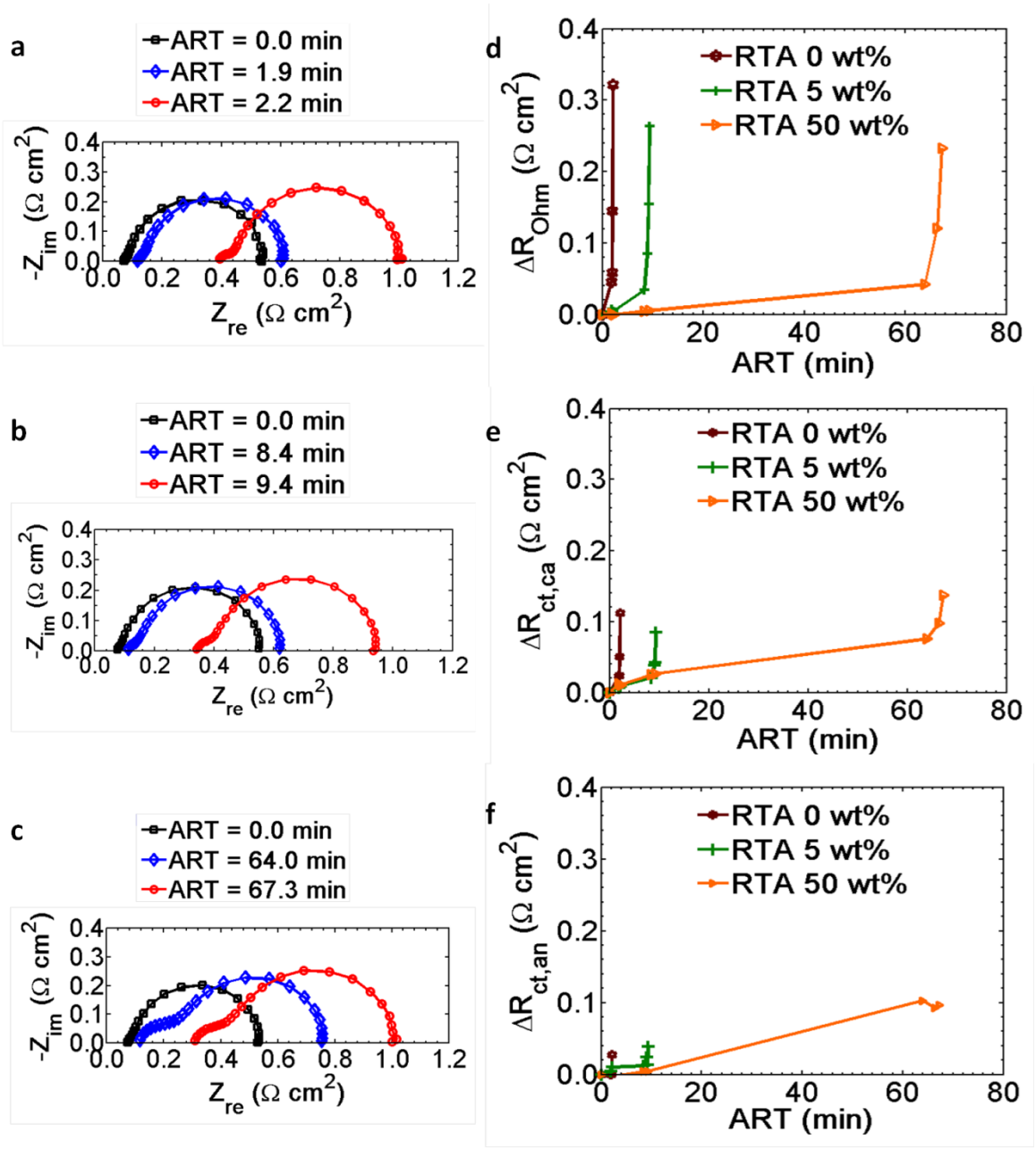

Figure 5.7. Nyquist plot from EIS measurements done of the RTA 0 wt% (a), RTA 5 wt% (b) and RTA 50 wt% (c)MEAs at BOL(black, squares), after first reversal test(blue, diamonds) and at EOL(red, circles). Change in Ohmic resistance (d), cathode charge transfer resistance (e) and anode charge transfer resistance (f) of the MEAs with increase in voltage reversal time.

Fig. 5.8(a)-(c) show the cathode CVs and Fig. 5.8(d)-(f) show the anode CVs of the three kinds of MEAs. For simplicity, only the measurements at BOL, after the first reversal test and at EOL are plotted here. The anode CV patterns show a gradual evolution from the first reversal test to the consecutive ones. The cathode CVs do not show much difference before and after reversals, except for a slight decrease in the electrochemical surface area (ECSA) of the Pt catalyst [14]. The change in ECSA for the MEAs with progressing reversal time is depicted in Figure 5.9. The slight decrease of ECSA, which scaled with the accumulated reversal time, might have been an effect of the repeated potential sweeps the cathode was subjected to after each reversal test [50], [57], [116]. The anode CVs on the other hand show significant changes after the reversal tests. Prominent new redox peaks evolved around 0.6 V which is characteristic of carbon oxidation/corrosion [50], [63], [117]. These peaks could have resulted from the surface oxide formation due to the hydroquinone-quinone (HQ-Q) redox reaction (Eq. 5) on the carbon support surface [50], [118].

$$C = O + e^- + H+ \rightarrow C{-}OH \qquad (5)$$

It is also interesting to observe that the redox peak current decreases gradually after the first reversal test; hence, the peak current is lower in the EOL CVs. It implies that the HQ-Q redox reaction is weaker after the first oxidative conditions were experienced, possibly due to loss of electroactive carbon surface.

A consistent change in the current densities at the hydrogen adsorption peaks for Pt in anode resulting from cell reversal is also detected. The switching of the current peaks corresponding to strongly and weakly adsorbed H on Pt in the CVs after reversal implies physio-chemical changes of Pt catalyst and changes in its crystal size [18]. The

difference between the peak currents corresponding to H-adsorption on Pt crystal surfaces is quantified and plotted as a function of voltage reversal time (Figure 5.10) and is also found to decrease, i.e., becomes negative after first reversal and decreases further with increasing reversal time.

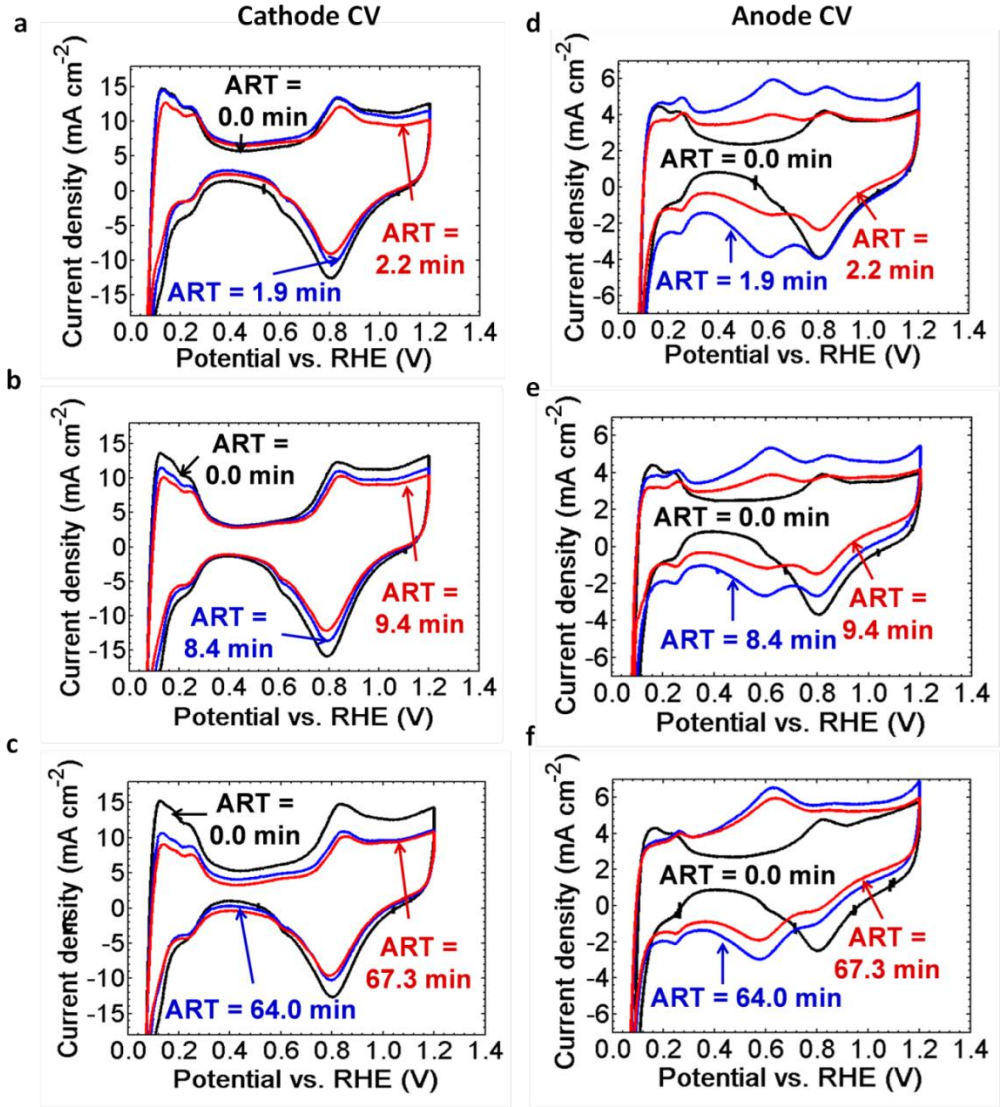

Figure 5.8.(a-c) Cathode CVs for RTA 0 et%, RTA 5 wt% and RTA 50 wt% respectively. (d-f) Anode CVs for RTA 0 wt%, RTA 5 wt% and RTA 50 wt% respectively. The three traces are for CVs measured at BOL, after first reversal test and after EOL is reached, with the total reversal time denoted in the figures.

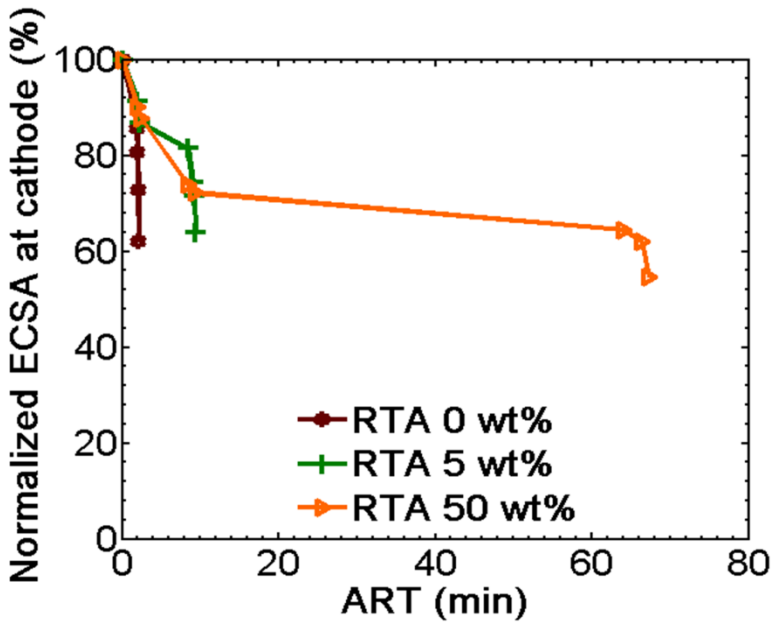

Figure 5.9. Change in ECSA of Pt catalyst in the cathode (estimated from cathode CV) shown as percentage w.r.t. to the ECSA at BOL for all the MEAs with increasing accumulated reversal time (ART).

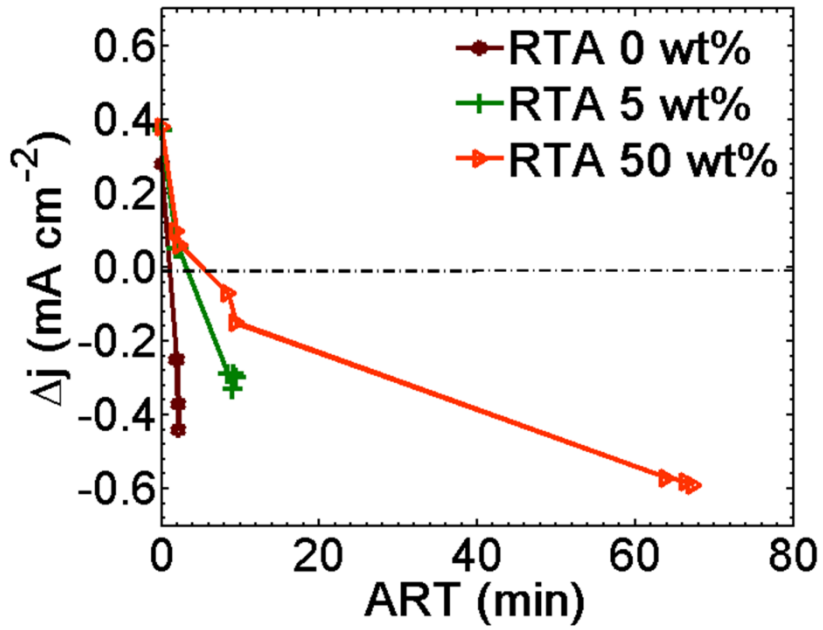

Figure 5.10. Change in the difference in the H-adsorption peak on Pt with accumulated reversal time, obtained from the anode CVs of the MEAs.

5.2. Morphological Analysis

The MEA samples were imaged in 3D in its pristine state and at EOL condition. The large-field-of-view (LFOV) absorption contrast mode (field-of-view of 65 µm with spatial resolution of 150 nm) was used for the tomography scans. In LFOV absorption mode, a direct mapping of the Pt catalyst distribution in the anode was obtained from the image intensity, although the macropores (~100 nm) pores were not resolved. The anode samples were extracted by laser ablation, such that the imaged volume remains untouched, making sure no artifacts were introduced from sample preparation method (further details in Chapter 2). Nano-CT is the perfect instrument to image internal structures in 3D non-destructively. Figure 5.11 presents an internal cropped volume of each reconstructed image of anodes in pristine and EOL states. The greyscale images shown on the right face of the 3D images represent a raw tomographic cross-section of the anodes, where the bright region represents the solid domain comprising Pt/C while the brightest zones (shown in orange in the volume renderings) are IrO_2 agglomerates. A significant loss in the anode thickness and corresponding increase in the intensity [14] of the anode in the EOL images w.r.t. pristine anode was observed. This clearly shows evidence of loss of carbon support from the anode. Careful observation of the pristine vs EOL anode structure, reveals that the low asperities on the top surface (resulted from decal transfer method of anode fabrication) of the anode is preserved in the EOL state despite the loss of carbon support. This suggests that carbon loss is more concentrated at the membrane-anode interface causing structural collapse and electrically and ionically disconnected volumes, resulting in a huge increase in Ohmic resistance, as shown in Figure 5.12.

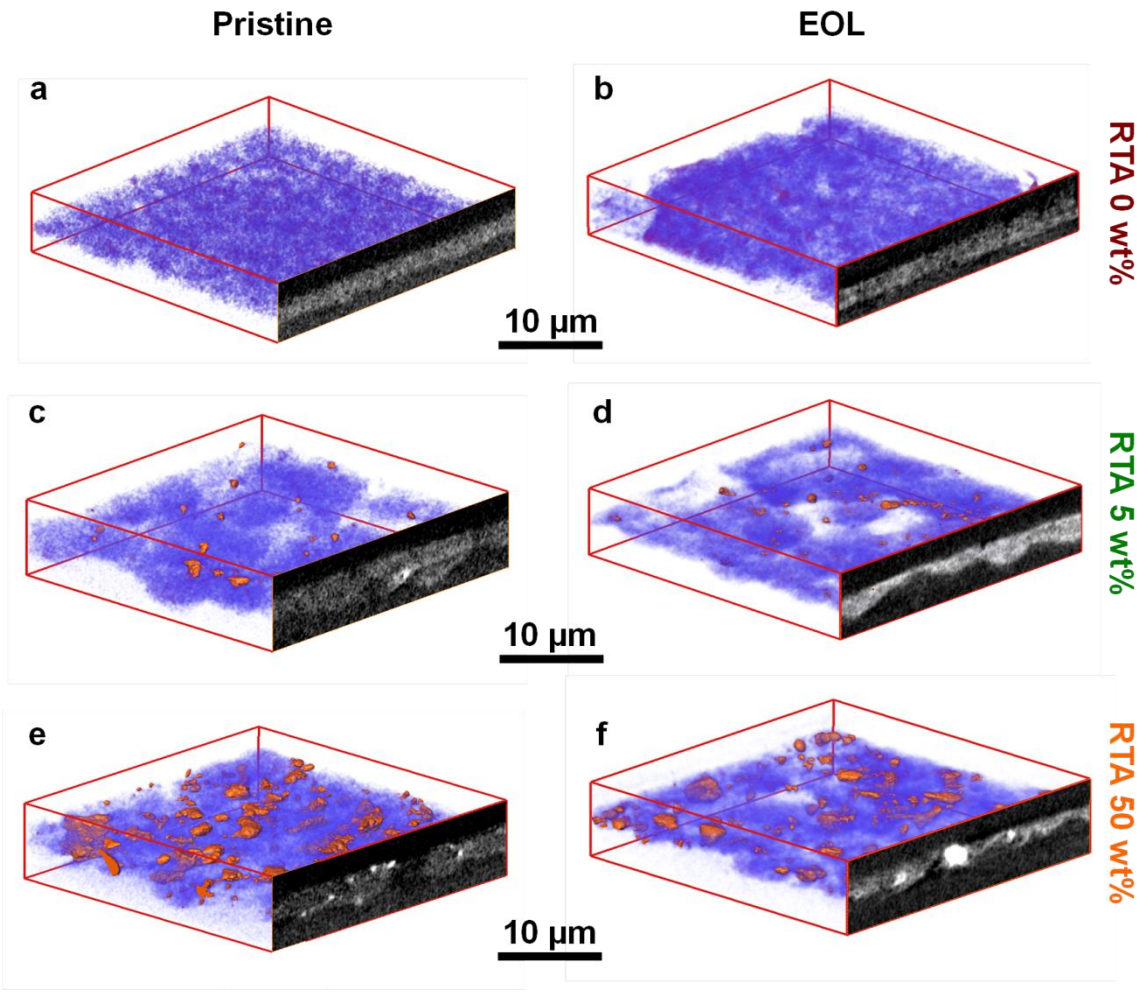

Figure 5.11. 3D volume renderings of the anodes in pristine state are shown on the left (a, c and e) and in the EOL state is shown on the right (b, d and f). The volume in purple/blue is the intensity based rendering of the raw image showing the porous matrix of Pt/C-ionomer. The IrO_2 is rendered in orange. The greyscale images, on the right of the volume renderings show a virtual cross-section (tomographic slice) through the imaged volume of the anode, in which, the bright zone is the anode. (The large bright parts are IrO_2 and the grey region is the Pt/C-ionomer matrix).

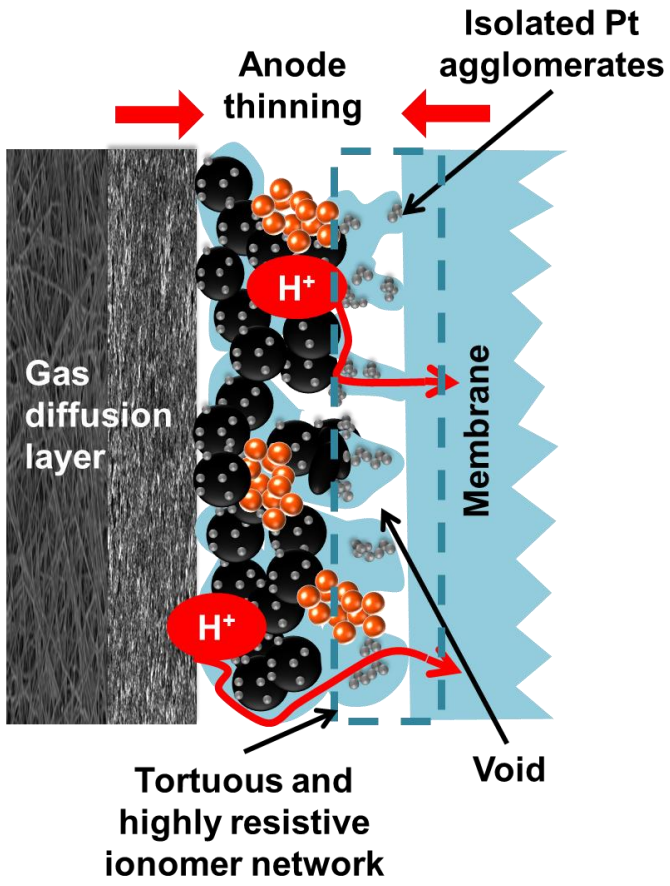

Figure 5.12. A schematic representation of a degraded RTA, showing carbon loss, Pt-catalyst agglomeration and isolation, and highly resistive ionomer network near the membrane.

The RTA 5 wt% (Figure 5.11(c) and (d)) and 50 wt% (Figure 5.11(e) and (f)) anodes show agglomeration of OER catalyst which limits the utilization of the expensive IrO_2. The images bear evidence that IrO_2 is physically still existent in the EOL anodes, although their OER functionality seems to be lost from the electrochemical measurements. This demands further studies to understand the deactivation of the RTA (discussed in Chapter 7).

The thickness of the anode was measured over the tomography slices through the internal volume of the imaged samples and the average thickness is shown in Figure 5.13 (a). The variation in the anode thickness across the imaged area is shown by the error bars indicating the standard deviation values. The IrO_2 agglomerates were segmented out of the greyscale 3D images (as shown in Figure 5.11 as well), labelled, and morphological data was characterized. The total volume and the total surface area of OER catalyst in the footprint of 36 µm × 36 µm of the RTA 5 wt% and RTA 50 wt% are shown in Figure 5.13 (b) and (c), respectively. Higher loading of IrO_2 lead to higher degree of agglomeration, resulting in loss of effectivity of the catalyst. The total volume of the catalyst in RTA 50 wt% is nearly 10 times that of RTA 5 wt%. However, the calculated surface area (which is not equivalent to the total electrochemically active surface area of the catalyst) is only about 5 times higher than that of RTA 5wt%. Larger agglomerates also cause an increase in the mass transport losses during the OER, as has been discussed in Chapter 3.

On comparing the pristine anode with the EOL anode, a significant loss of catalyst layer thickness is seen. The RTA 5 wt% seems to lose the highest amount of carbon support. The reason for retention of anode thickness in RTA 50wt% might have resulted from the huge IrO_2 catalyst boulders contributing to the average catalyst-layer thickness. Some loss in the OER catalyst volume and surface area is also evident. This might have resulted from loss or dissolution of IrO_2 itself (due to high range of potentials from 0 to 2.8 V it has been subjected to) and loss of internal porosity of the catalyst agglomerates [32], [119]–[122]. However a significant amount of IrO_2 is retained in the EOL state as well, which again reinforces the fact that the cessation of water electrolysis

was not due to complete disappearance of the OER catalyst, but there should be some kind of irreversible deactivation of the catalyst during cell reversal.

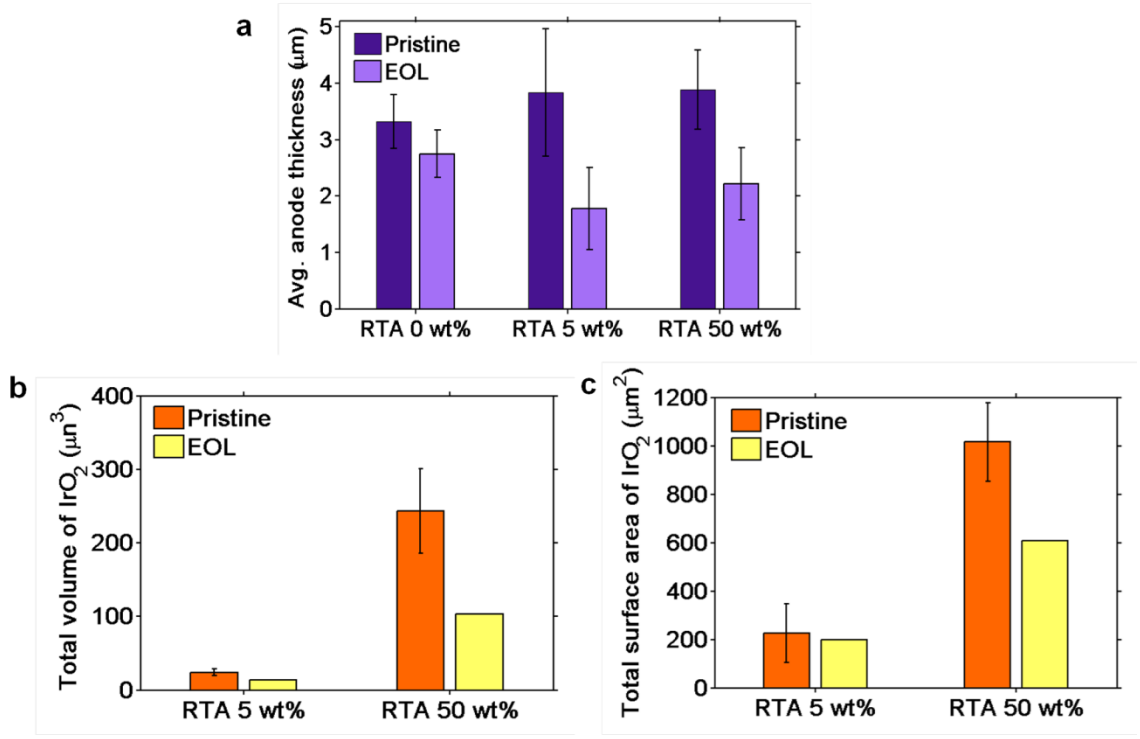

Figure 5.13. (a) Anode thickness in pristine and EOL state of the MEAs. (b) and (c) Total volume and surface area of the segmented IrO_2 agglomerates in the pristine and EOL of RTA 5 wt% and RTA 50 wt% specimens, respectively. The bars show average value and the error bars show the standard deviation in the values.

The cross-section of the pristine MEA and the MEA at EOL was also imaged using SEM and there was also no significant change observed in the PEM or the cathode of the MEAs (Figure 5.14). This suggests that all the changes in the anode led to the majority of performance loss. In order to verify any degradation of the ionomer (which is common at high potentials [53], [56]–[58], [123]), fluoride emission measurements (using Orion™ Fluoride Electrodes, Thermo Fisher Scientific, USA) were also performed on the effluent (or condensed) water from the anode and cathode exhaust, collected

during the cell reversal period and the following conditioning process (to allow the gases to leach any residual ionomer degradation species). However, there was no significant change in fluoride concentration from the regular operation to reversal state. Moreover, the variation in the concentration did not correlate with the loss in performance of the cell (Figure 5.15). The reason for detecting low concentration of fluoride ion compared to fluoride ion emission during accelerated stress tests of MEA (e.g., long-term OCV hold tests) could be the following: The high stoichiometry flow rates of gases resulted in higher amount of water being condensed from the excess gases and a very small amount of water is actually produced within the cell during ORR during the cell reversal conditions at low current density (the MEA active area was also small); the ionomer degradation must have been very low and limited to the dispersed ionomer within the electrode and not the bulk electrolyte membrane. This reinforces the fact that any damage to the ionomer membrane had only minor contribution to the overall loss of the cell performance. It is however interesting to note that, the fluoride emission rate is highest during the first reversal test although the degradation rate during the first reversal is lower than that during the following reversals. This indicates that cell reversal does lead to ionomer degradation to a small degree and the first time the reversal is experienced does the maximum damage to the ionomer.

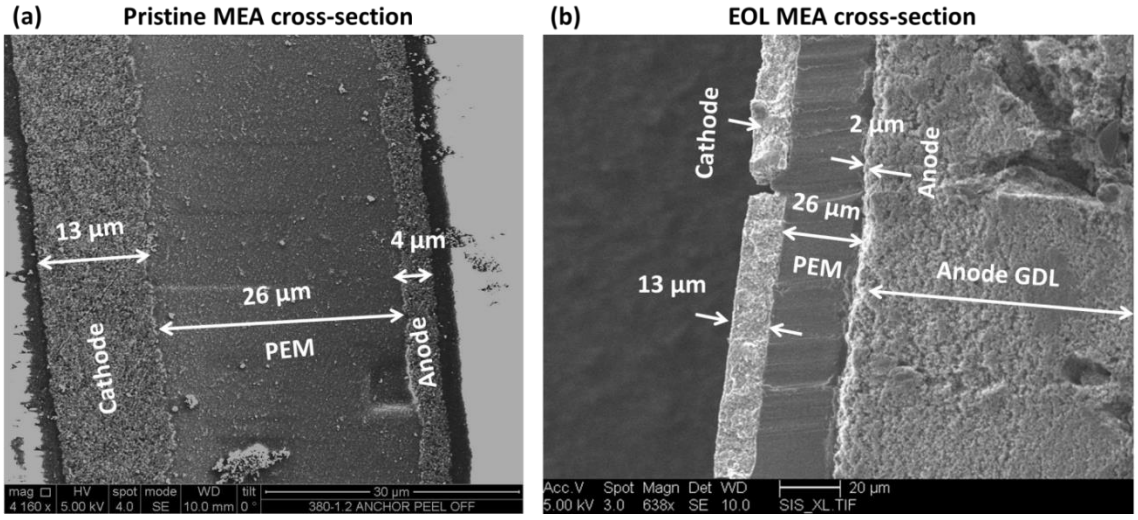

Figure 5.14. SEM images of MEA cross-sections: (a) MEA (RTA 0 wt%) in pristine condition and (b), an MEA (RTA 5 wt%) in EOL condition after several cell reversal tests.

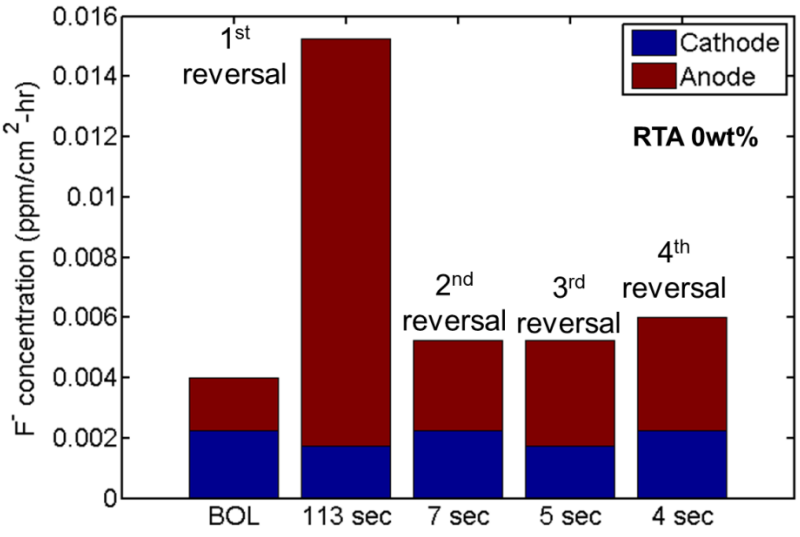

Figure 5.15. Fluoride emission rate during regular operation and during reversal tests measured from effluent water from anode and cathode of the RTA 0 wt% MEA.

5.3. Conclusion

The higher the loading of the OER catalyst in the anode, the higher was the tolerance to reversal and slower was the degradation rate. However, 50 wt% (w.r.t. Pt loading) of OER catalyst loading is a relatively high amount of precious metal-based catalyst, which increases the cost of a fuel cell stack. There exists a trade-off between increased durability of the cell and minimizing the cost. The current study revealed that the catalyst utilization in the RTA is low because of the high degree of agglomeration of the IrO_2 particles. A better design of the RTA can yield higher activity of the OER catalyst and ensure higher reversal tolerance capability with a reduced loading of the catalyst.

Chapter 6

Role of Water in Degradation due to Cell Reversal

6.1. Introduction

Chapter 5 depicted that water electrolysis is the basis for the durability of RTAs. Water is not only essential for the OER to proceed, but it is also a reactant in carbon corrosion reaction. Thus, water plays an important role in cell reversal phenomena. To ensure protection from cell reversal, an RTA needs to be effective under all operating conditions, including high temperature (i.e., > 80^{o}C) and high and low relative humidity (RH) conditions. In this Chapter, I will discuss the phenomena of cell reversal on MEAs with RTA 50 wt% under a range of RH conditions and at a high operating temperature. An operation of fuel cells at high temperature is preferred because it enhances the heat rejection capacity of the fuel cell system to the environment, thus reducing the radiator size in FCEVs leading to more compact designs [124], [125]. Non-intuitive behavior of

RTA at higher RH conditions has been found. In this chapter, the observations and critical vulnerability of RTA at high temperature have been discussed [126].

6.2. Electrochemical Diagnostics

6.2.1. MEA Fabrication and Experimental Procedure

The electrochemical diagnostics protocol was similar to that described in Chapter 5. The MEAs with RTA 50 wt% were used for the water-activity dependence tests. A new protocol was used for the reversal tests only. We simulated degradation due to cell reversal at high temperature for RTA 50 wt% MEAs by heating the cell to 90^0C and setting the reactant humidifier temperature at 46, 60, 65, 75 and 85^0C, to maintain the RH within the cell at 14%, 28%, 36%, 55%, 68% and 82% respectively for different sets of experiments. Relative humidity for both the anode and cathode was kept the same to avoid any uncertainties of water content in the reactant gases owing to intra-cellular water transport. The cell was conditioned at a high temperature and respective RH conditions for an hour before the cell reversal test was performed, to obtain a steady operation at those conditions. As described in Chapter 5, while conditioning the cell, the higher limit of the current at which the cell was operated was set such that the cell potential recorded was > 0.3 V. This would prevent any irreversible cell aging before and during the diagnostics itself. We measured the polarization curve, EIS and CV at a cell temperature of 65^0C and 100% RH to make the diagnostics consistent and eliminate effects of temperature and RH on the electrochemical measurements to yield reliable comparison of the degradation phenomena for different cases. The dry conditions in the

cell increase the ionic resistance in the cell which causes the cell potential to drop under fuel-supply as well as fuel starved condition. At lower RH, the overpotential for OER reaction also increased causing higher anode half-cell-potentials. In order to hit the second plateau in the voltage reversal pattern and allow longer reversal dwelling times (to make the degradation experiments faster), the voltage cut-off was decreased to -2.5 V. The reversal testing was repeated until the voltage at 0.4 A cm^{-2} (representing the cell performance) fell below roughly 30% of its BOL value and was then considered to be at the end-of-life (EOL) state. Unlike the protocol described in Chapter 5, the first reversal test was uninterrupted, i.e. for all the MEAs the load was not ceased under hydrogen starved condition until the voltage cut-off was reached.

6.2.2. Electrochemical Measurement Results

Figure 6.1(a) shows the first reversal behavior of the RTA MEAs under cell reversal at different RH conditions. The reversal behavior for intermediate RHs, i.e., 55–68% being similar, only the voltage reversal plot for 68% RH is shown for simplicity. Similarly, for the dry regime 28-36% RH cases, only a representative case of first reversal behavior at 28% RH is shown. Fig. 6.1(b) shows the duration of the first reversal (first reversal time, FRT) plotted as a function of RH. It summarizes the effect of RH on the durability of PEFCs with an RTA. The FRT is considered to be an important metric for the reliability of an RTA strategy, because the moment the water electrolysis regime transitions to carbon corrosion regime, the cell potential quickly drops to very low (i.e. high negative values) values and if the potential drop is not externally controlled, it leads to catastrophic failure of the cell.

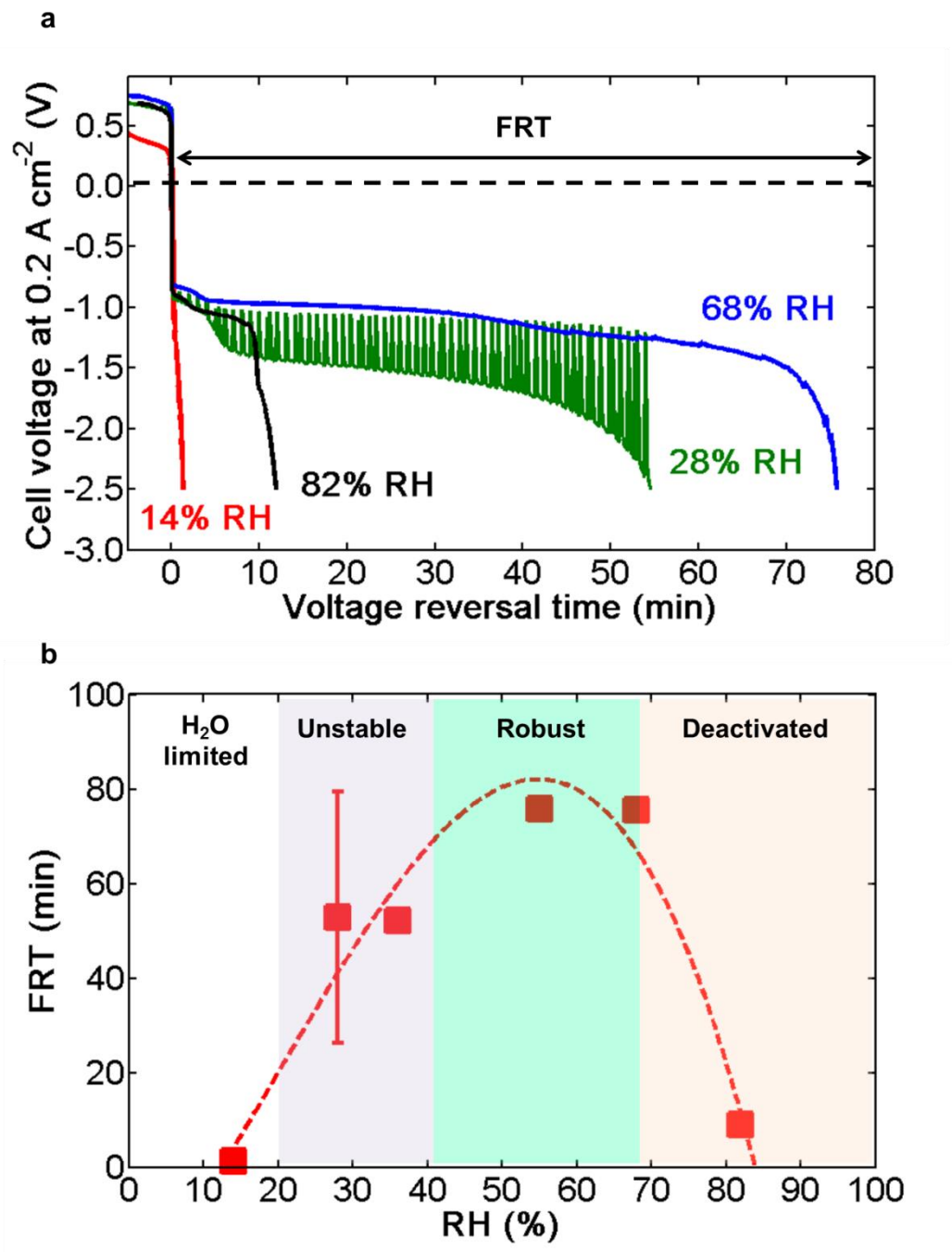

Figure 6.1. (a) First reversal behavior of RTA 50 wt% MEA undergoing cell reversal at different RH conditions. (b) First reversal time (FRT) as a function of the RH. The dotted line is used as a visual guide. The shaded regions denote operation regimes for an RTA.

From Figure 6.1, it is clear that at very dry conditions (e.g. at 14% RH), the cell environment is deficient of water in the anode for water electrolysis or carbon corrosion (resulting in high concentration overpotentials) to proceed and hence the anode potential rises (i.e. E_{Cell} drops) very fast to sustain the load resulting in a very short FRT. We call this regime as "H_2O limited", where the RTA is unable to protect the cell from failure in case of hydrogen starvation. The next zone around 28-36% RH shows very interesting behavior. As the tests were repeated with several cell builds, the FRT was found to vary by a large magnitude (25 to 79 min). Figure 6.1(b) depicts the average value for FRT along with the standard deviation for each RH case tested. The cell voltage under H_2 starvation condition also shows huge oscillating nature in this regime. It has been reported that the periodic build-up and removal of liquid water in the cell could cause unstable cell performance and the voltage oscillations could result from either poisoning effects of the catalysts or complex water dynamics [127]–[129]. In order to ensure if the oscillations resulted from changes in ORR potential due to ionomer hydration-dehydration induced water dynamics in the cathode, another cell was operated at 0.2 A cm^{-2} under 28% and 36% RHs while H_2 and air was supplied to the anode and cathode respectively. The magnitude of periodic oscillations observed in this condition was negligible (Figure 6.2) and the frequency was much lower than that observed at cell reversal condition (Figure 6.1(a)), which clearly indicates that the huge oscillations in reversal condition resulted from the interplay of ionomer-water dynamics with water electrolysis on IrO_2 and oxidation of carbon support in the anode. The unpredictable nature of this regime makes it unfavorable for vehicle operation and we term this regime as "Unstable".

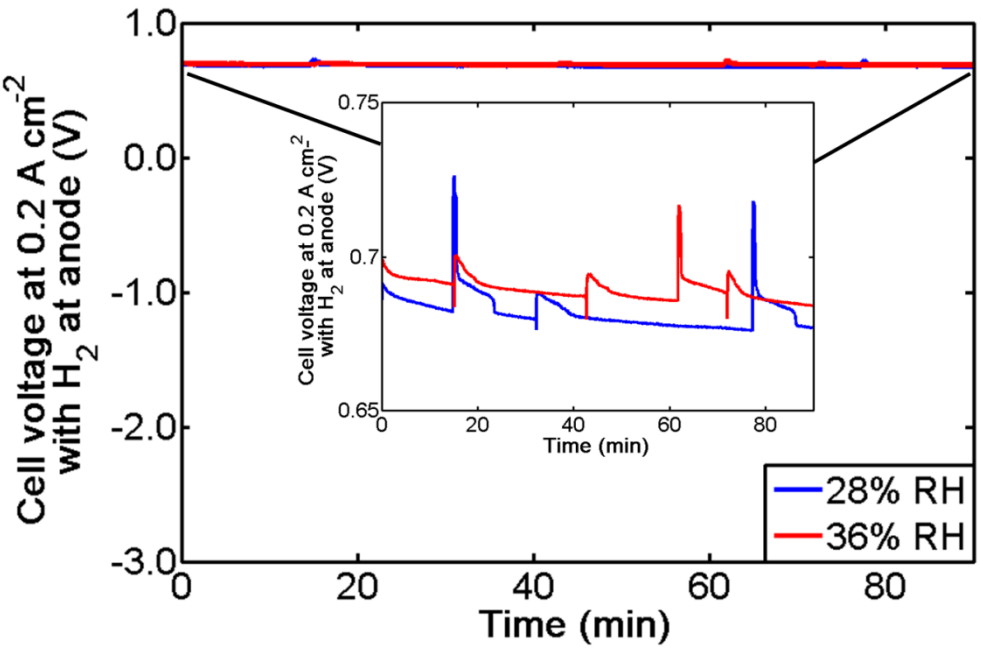

Figure 6.2. Cell potential measured at low RH under regular reactant gases (i.e. H_2 at anode and air at cathode) shown to the scale of the voltage reversal plots. The inset is a zoomed in version of the plot to show small fluctuation in the voltage measured.

The intermediate regime of 55%-68% RH was found to be most consistent with a small range of FRT variation, making the regime highly predictable w.r.t. the reversal dwelling time. This regime is thus coined as the "Robust" zone. The durability of the RTA at higher RH conditions was also tested by subjecting the cell to reversal condition at 82% RH. Higher RH means higher water activity, i.e., it is expected to provide a favorable condition for IrO_2 to facilitate water electrolysis under this condition. However, in contrary to our expectation, the FRT was much shorter than in the intermediate RH case (and also much shorter than 65^0C, 100% RH case, although higher temperature should increase the activity of OER catalyst [24]). This finding suggests that there is a complex interplay of the activity of IrO_2 as an OER catalyst and activity of carbon for

oxidation with the change in temperature and water activity, which is not well understood at the current state. The hypothesis to explain the phenomena has been described in Chapter 8. The faster deactivation of the RTA at higher RH and higher temperature conditions needs further investigation at a fundamental level. This zone is named "Deactivated" because of the short FRT and apparent deactivation of the OER, making the condition unfavorable for vehicle operation.

Figure 6.3(a) illustrates the polarization curve for 82% RH case, measured at BOL and after every reversal as a representative case. Only one set of polarizations curves is shown because the other cases exhibited similar degradation patterns. The cell performance was compared based on a cell potential when at 0.4 A cm^{-2}. When the cell performance decreased to around 30% of BOL performance the cell is considered to have reached EOL. The loss of performance with each reversal test for all the RH cases tested is shown in Figure 6.3(b). For the 28 and 82% RH experiments, the decay pattern for the most representative case (i.e., that had the FRT closest to the average of the repeated tests) case is included in this plot. From the slope of the decay curves, one can see the different rate of degradation at different RH conditions. In order to quantify the rate of degradation, the percentage loss in performance per reversal time has been plotted against the RH in Figure 6.4. It shows the rate of degradation until the first reversal test. During the first reversal test, the degradation is slower than the consecutive reversals. However, the first degradation rate is a crucial metric to standardize the effectiveness and durability of an RTA because the first event (when the cell potential hits -2.5 V) is enough to degrade the cell down by 20% (that too when the reversal is actively mitigated by using

voltage cut-off), which is practically EOL for real-life application in FCEVs, if it happens to all the cells in the stack.

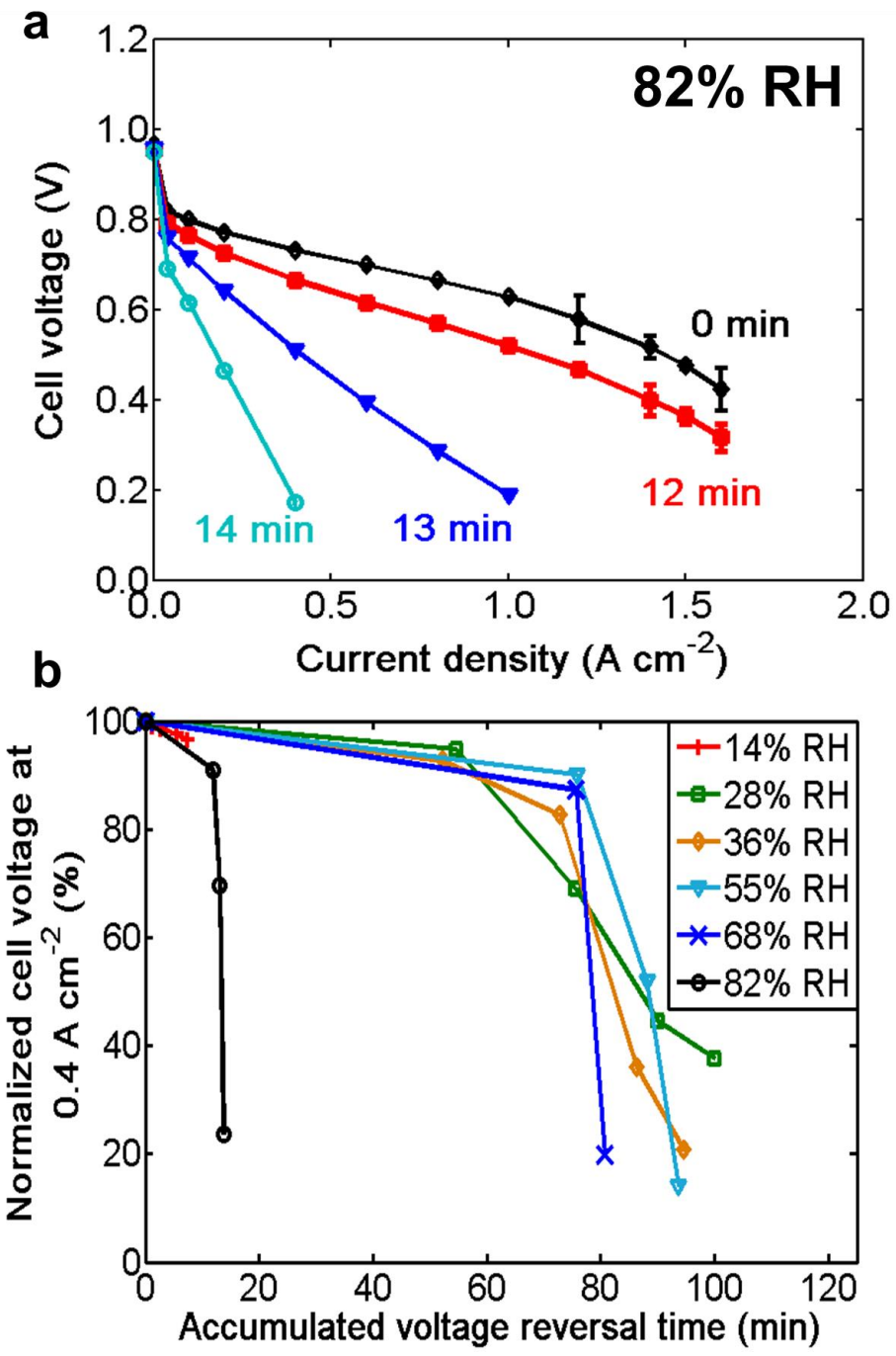

Figure 6.3. (a) Polarization curves measured at BOL and after each reversal test performed at 82% RH. (b) Performance decay of RTA MEAs due to cell reversal.

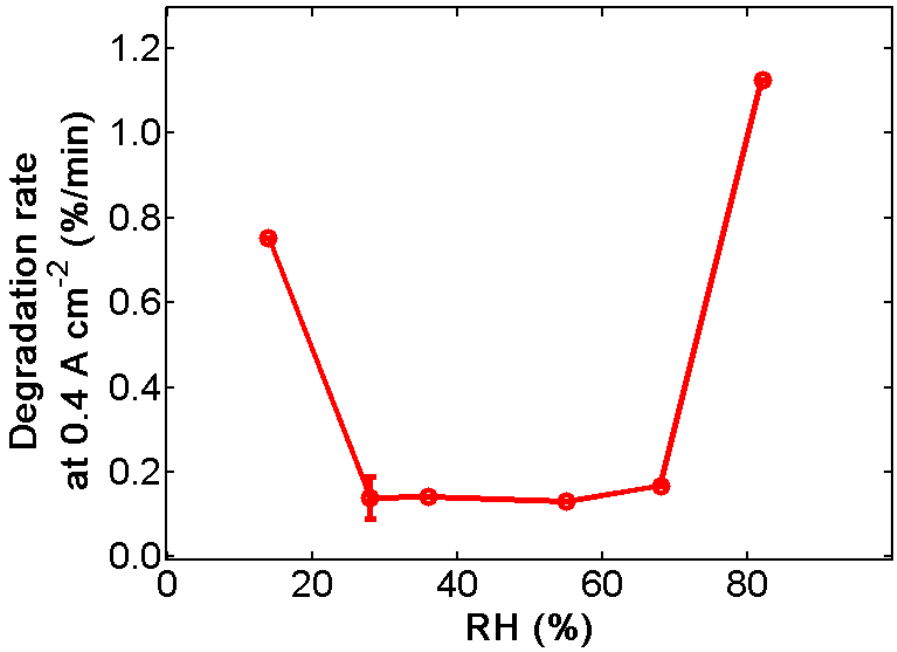

Figure 6.4. Degradation rate during first cell reversal at different RH conditions.

EIS was measured at BOL and after each reversal test for each of set of MEAs. Figure 6.5, shows the Nyquist plots obtained from EIS measurements for 28%, 68% and 82% RH cases as representative of the three possible regimes of vehicle operation. The Figure shows only the Nyquist plots for EIS measured at BOL, after first reversal and after EOL was reached. We can clearly see that the increase in Ohmic resistance (R_{Ohm}) is more pronounced as the RH for cell reversal increases and the increase in anode charge transfer resistance (R_{an}) becomes less pronounced. The prominent loop on the left (especially observed in the low to medium RH range), corresponding to R_{an} is very rare for a PEFC because of fast HOR kinetics and minimal mass transfer resistance in a regular fuel cell.

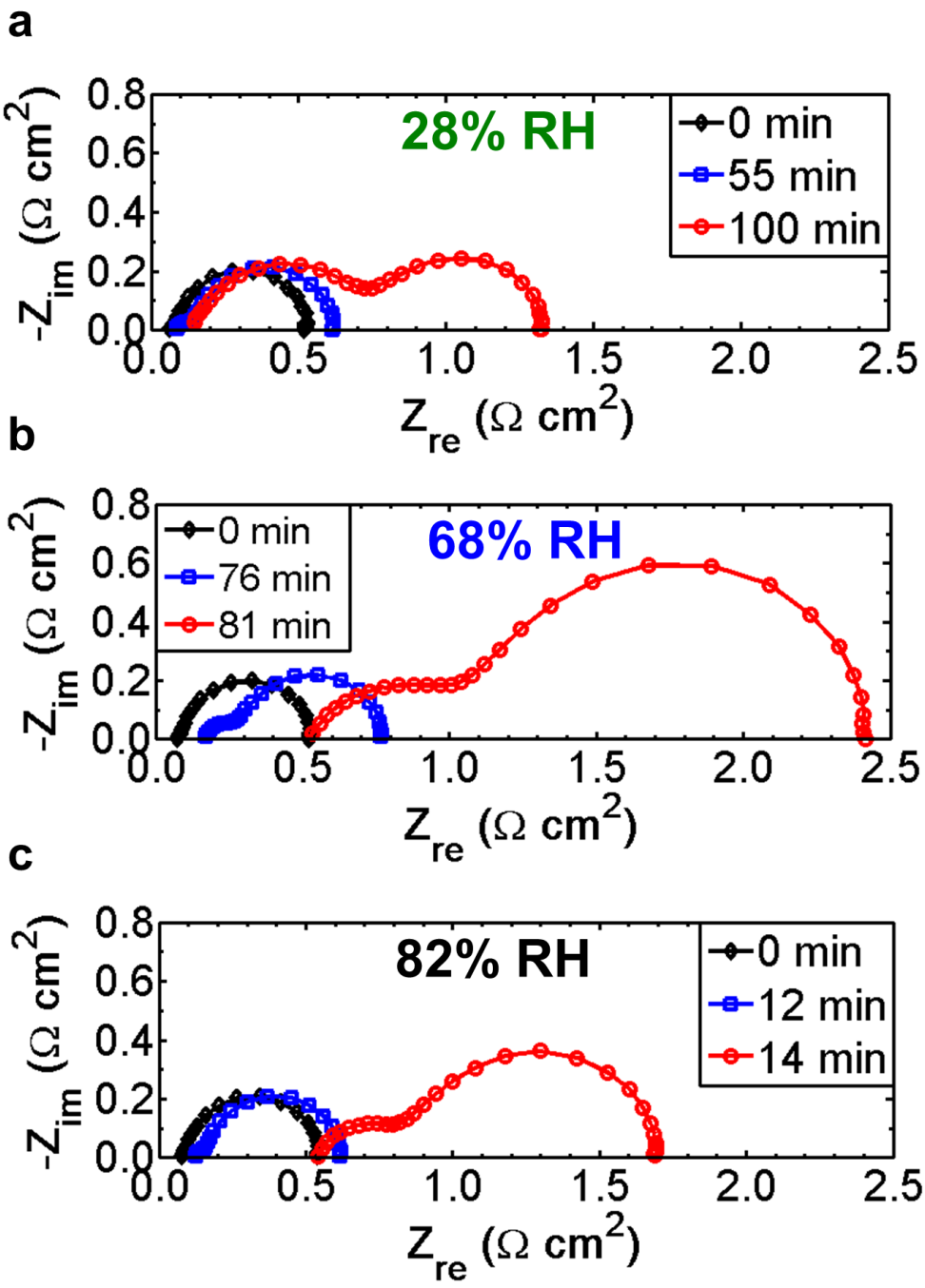

Figure 6.5. Nyquist plots for EIS measured at BOL (black-diamonds), after first cell reversal (blue-squares) and at EOL (red-circles) for MEAs that have undergone cell reversal at 28% RH (a), 68% RH (b), and 82% RH (c).

This suggests that there are subtle differences in the final degraded form of the anode as the cell reversal occurred at different RH ranges. An increase in cathode charge transfer resistance (R_{ca}) is also observed, especially in the medium to high RH regimes. The higher increase in the 68% RH case might be due to higher reversal dwelling time as compared to the 82% RH case.

The evolution of the anode CVs with cell reversal at different RH values also show a different trend (Figure 6.6). The anode CV for the 28% RH case (Figure 6.6(a)) appears to lose all the characteristic H-adsorption/desorption peaks, which suggests deactivation of Pt for the HOR or dissolution due to large magnitude potential cycling during cell reversal. The smaller increase in R_{Ohm} also correlates with lower carbon loss (represented as anode thickness loss in Fig. 6.7(a)) and absence of the carbon oxidation redox peaks around 0.6 V (likely to have resulted from HQ-Q redox reaction on the carbon catalyst support surface [50], [118]), which are present in the 68% and 82% RH after-reversal CVs. The relative change in the H-adsorption peak current densities are also present in the intermediate to high RH reversal cases as we observed in Chapter 5, implying a similar degradation mechanism for these cases despite the difference in reversal tolerance time altered by the elevated temperature and lower humidity of the gases. It is also interesting to notice the drop of the double layer capacitance and the carbon oxidation peaks as the reversal tests were repeated (as seen from the EOL CV in Figure 6.6). This implies that, despite the short lived cell reversals after the first reversal test, the carbon oxidation must have been aggravated and reduced in the amount of electrochemically active surface area of carbon. The reduction in the peak could also

have resulted from partial removal of the adsorbed organic species on repetitive cycling of the MEA for the electrochemical diagnostics.

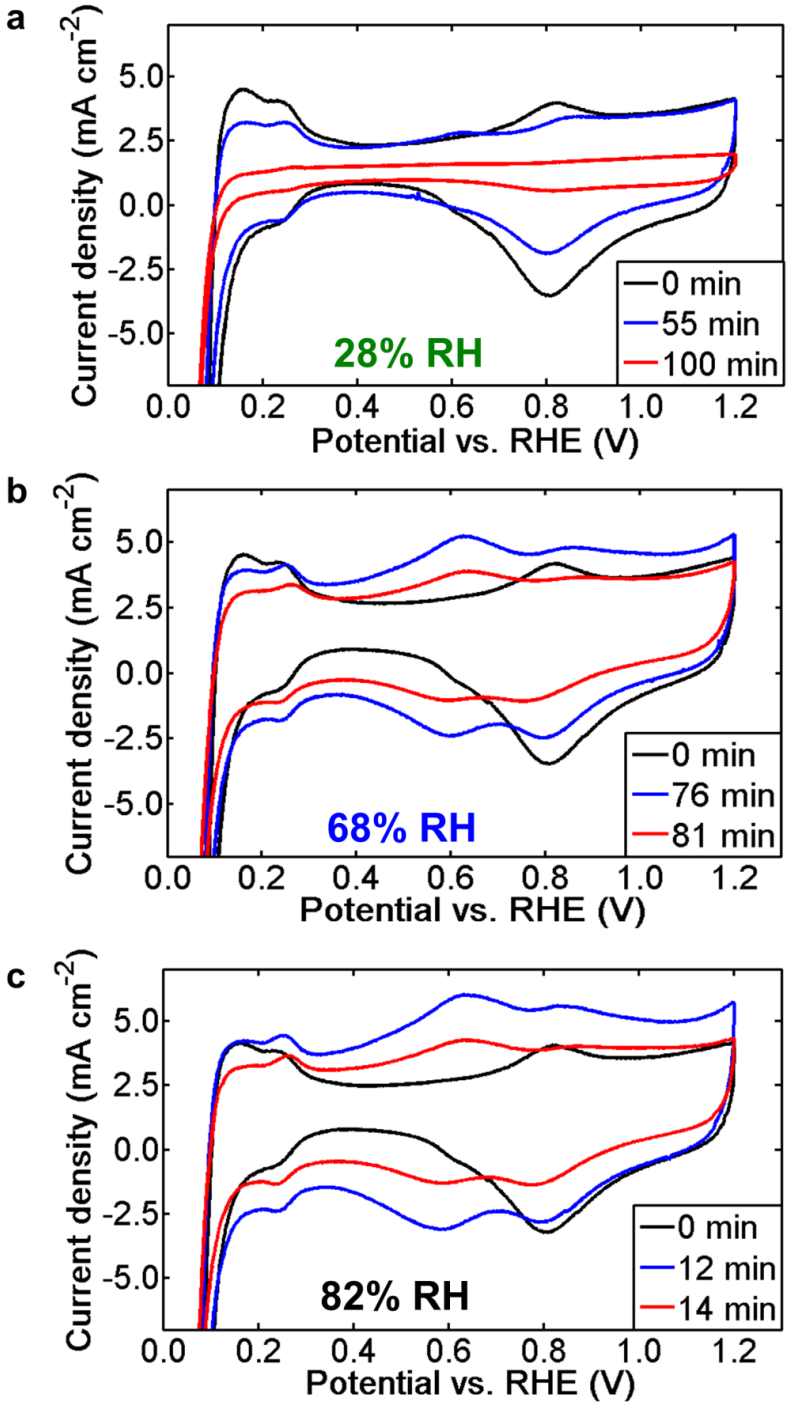

Figure 6.6. Anode CVs at BOL, after first cell reversal and at EOL for MEAs that have undergone cell reversal at 28% RH (a), 68% RH (b), and 82% RH (c).

6.3. Morphological Analysis

A section of the MEA was taken and the anode surface was imaged using a scanning electron microscope (SEM) (Quanta 200 FEG, FEI) with its back-scattered electron detector. The GDL was carefully separated from the degraded anode using tweezers to expose the anode's surface. Figure 6.7(a) shows the anode surface on the pristine MEA and Figure 6.7(b) shows the anode surface of the 68% RH EOL MEA. The bright zones in the SEM images are the agglomerates of IrO_2 in the anode. A very heterogeneous distribution of IrO_2 is observed. Comparing the pristine anode surface (Figure 6.7(a)) and the EOL anode surface (Figure 6.7(b)), no apparent change in the content or distribution of IrO_2 was found. The SEM images gave us only limited 2D information for the anodes. In order to obtain volumetric data , to characterize and analyze possible alteration in the morphology of the anode in three-dimensions (3D), we used nano-CT. Nano-CT also aided in inspecting the internal interfaces between components, such as void formation at the membrane-anode interface. It is well known that carbon corrosion can yield significant changes to PEFC electrode morphology due to the removal of the catalyst's carbon support and the collapse of the electrode [50], [54], [59], [117], [130]–[136]. Nano-CT provides the ability to image within samples in a non-invasive and non-destructive nature and has been previously used to investigate the 3D structure of fuel cell electrodes [12], [19], [89], [90]. In order to gain further insight into the nature of the reversal degradation, nano-CT analysis was performed on pristine anode samples and EOL anode samples after being tested at different RH conditions. Figure 6.8a shows the 3D images of the pristine anode and Figures 6.8 (b), (c) and (d) show the EOL anode for the 28%, 68% and 82% RH cases respectively. The pristine anode has a

significant amount of IrO_2 particles (rendered in orange color) distributed within the anode catalyst layer, which apparently remains similar in the EOL anode. The tomographic slice is shown on the right side (in greyscale) of the 3D renderings. These are the virtual cross-sections through the imaged volume of the anodes. The brightest phase represents IrO_2 agglomerates, while the grey region is the Pt/C porous network and dark phases indicate mainly ionomer binder and pores that have low X-ray absorption coefficient and hence low intensity values. The nano-CT images were obtained in the X-ray absorption mode with an FOV of 65 μm and a voxel resolution of 64 nm. After the reversal tests, it was observed that the thickness of the EOL anode decreased significantly. In particular, the cross-sectional tomograph of the EOL anode exhibits a thinner and brighter anode as compared to that of the pristine one, which is attributed to higher concentration of Pt catalysts in the anode, due to the loss of carbon support via carbon corrosion during the reversal tests. The morphological changes in the other EOL anode samples at 28% and 82% RHs appear similar to that at 68% RH.

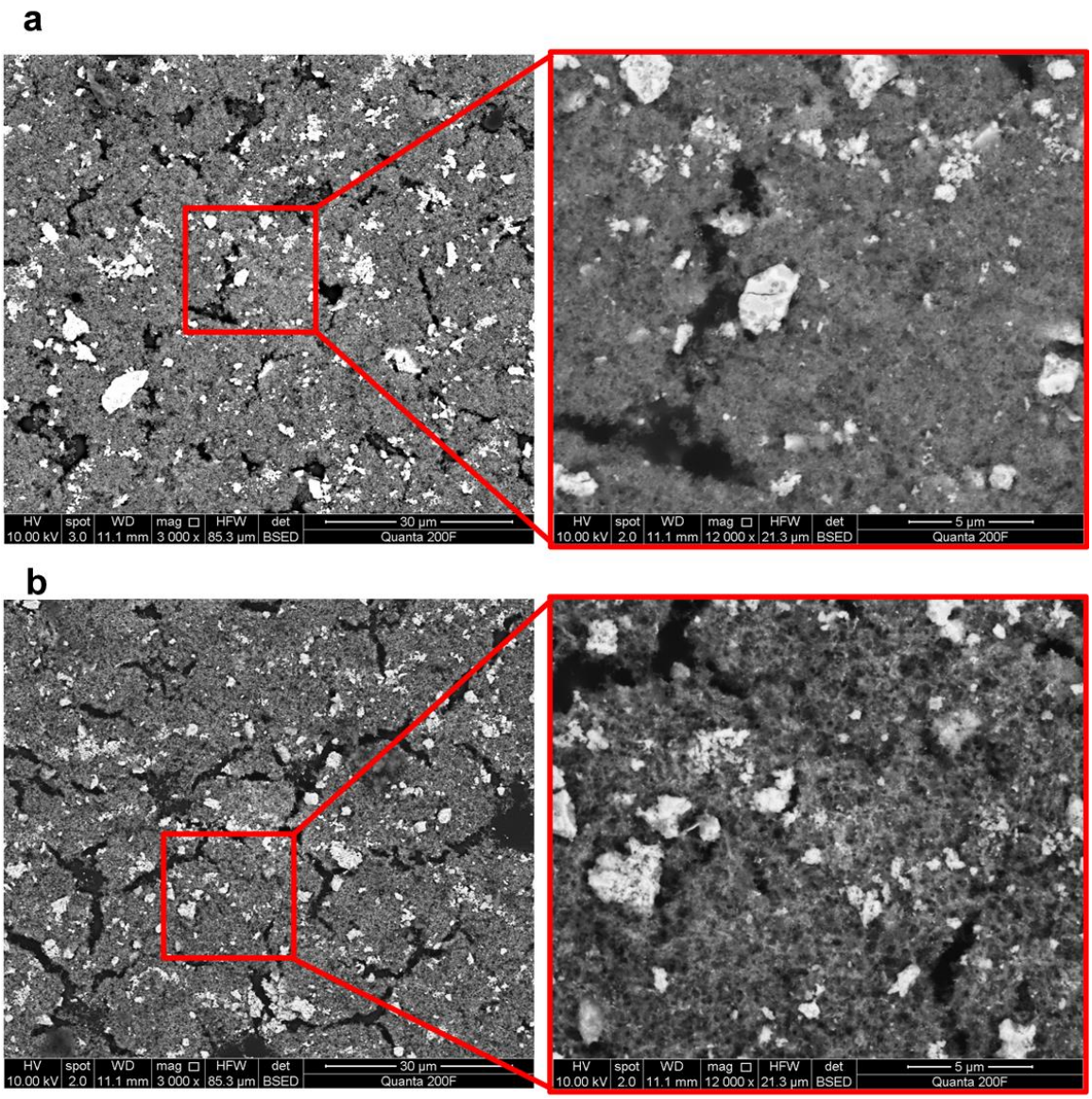

Figure 6.7. SEM images of anode surface of pristine MEA (a) and that of EOL MEA (i.e., catalyst layer-GDL interface) that has undergone cell reversal at 68% RH (b). The images on the right are the zoomed in images. The images were obtained using back-scatter electron detector. The brightest zones are IrO_2 agglomerates and the darkest regions are the pores and cracks on the anode surface. The medium greyscale intensity is the Pt/C/ionomer porous network.

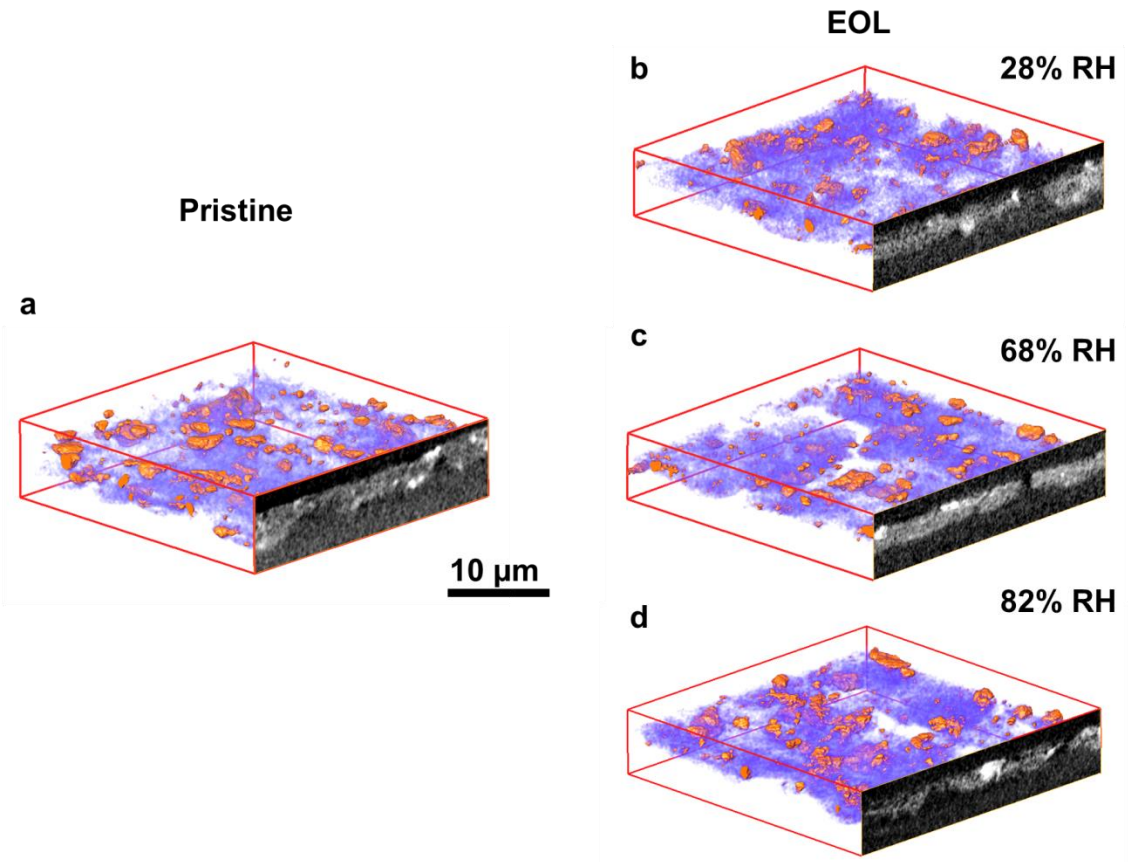

Figure 6.8.3D volume rendering of anode of pristine MEA (a) and EOL MEAs which have undergone cell reversal at 28% RH (b), 68% RH (c) and 82% RH (d). The grayscale image on the right face of the volume shows a virtual cross-section through the imaged anode volume. IrO_2 agglomerates have been segmented and rendered in orange in the 3D volume and they are the brightest phase in the tomographic slices shown. The intensity based rendering of the porous network of Pt/C/ionomer is shown in purple and is the bright layer in the tomographic slices. The footprint area of the anode volume rendered is 36 µm×36 µm.

Quantitative analysis of the 3D images (shown in Figure 6.9) reveals that the anode thicknesses, IrO_2 agglomerate volumes, and surface areas for all the EOL anodes at

28%, 68%, and 82% RHs generally decreased. The reduction of anode thickness resulted from severe carbon corrosion as well as microstructural collapse of the anode [99], [124], [125], [137], [138], while the decrease in IrO_2 volume and surface area might be attributed to the degradation, redistribution, or densification of the initially nanoporous IrO_2 catalysts during the reversal tests. It is noteworthy that the EOL anodes at all RHs retain a significant amount of IrO_2 catalysts. Thus, the eventual cessation of the water electrolysis cannot be attributed completely to the loss of IrO_2. Rather, there is some electrochemical deactivation mechanism, which needs to be further investigated. The volcano-type behavior of the reversal time with respect to the water-activity (proportional to RH) might have resulted from a competition between the increase of IrO_2 OER activity with higher RH and the opposing increase in the rate of deactivation with higher RH (which could be related to the carbon oxidation reaction's water activity dependence). The loss of anode thickness and the loss of OER catalyst are inversely correlated. The MEA undergoing cell reversal at 28% RH had the least loss of anode thickness, which is consistent with negligible increase in Ohmic resistance (Figure 6.5(a)) while the MEA undergoing cell reversal at 82% RH experienced highest loss of anode thickness which also correlates well with the increase in Ohmic resistance, likely to have been caused by a high resistance protonic network due to carbon loss near the membrane (explained in details in Chapter 7). However, the loss in IrO_2 was higher in case of 28% and 68% RH cases, which might have resulted from longer reversal time, although longer reversal time also means that the IrO_2 was active for water electrolysis for a longer duration at 58% RH but at 82% RH, it became deactivated faster.

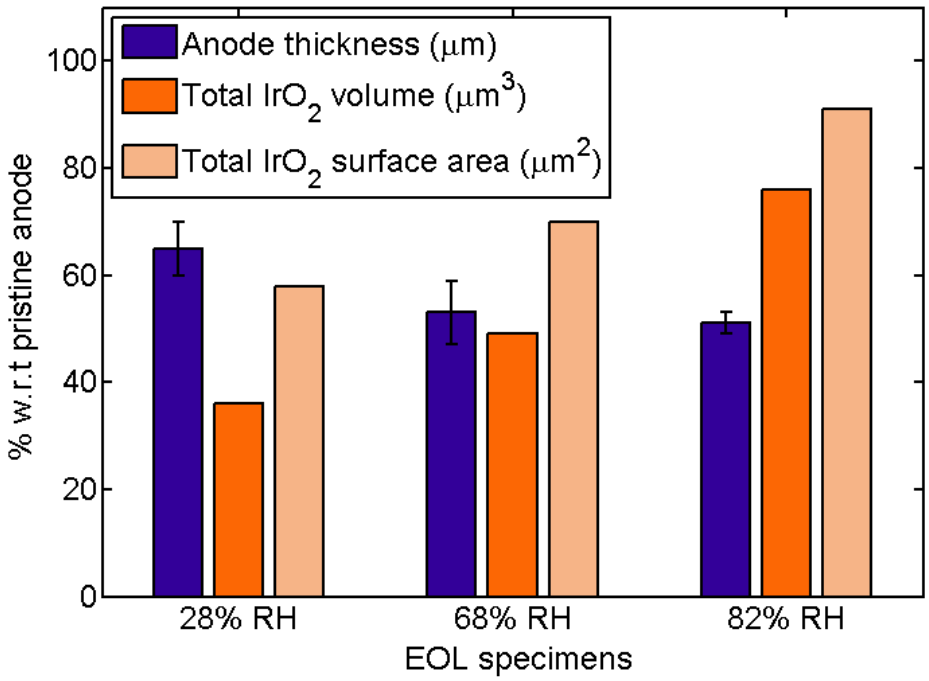

Figure 6.9. Anode thickness and the total volume and surface area of IrO_2 agglomerates present in the EOL MEA shown as percentage of the quantities in the pristine anode. The bar height for the anode thickness shows the average value measured over all the tomographic slices through 36 μm×36 μm footprint area of the imaged anode volume with the error-bars showing the standard deviation.

6.4. Conclusion

In this chapter, the durability of the RTA has been tested at different operating conditions. Besides, loss of durability and effectiveness of the OER catalyst at very low RH conditions, loss of durability was observed at high RH as well. The latter is considered anomalous because, high RH implied high water activity, which should promote OER. The shorter water electrolysis time at very low RH is intuitive because of non-availability of water as a reactant which makes the OER overpotentials high, thus the

anode quickly attains higher potentials. The deficit of water also impedes the carbon corrosion reaction. Hence, the loss of anode thickness was lower for the 28% RH case as compared to the 68% and 82% RH cases. The significant difference between the degradation characteristics of the water-deficient or "H_2O limited" regime with the "Robust" and water-excess or "Deactivated" regime, as observed from the EIS and CV measurements indicate that the role of water is very crucial to the effectiveness of an RTA. Besides managing the fuel cell operating conditions and/or design of the electrodes to ensure higher durability of a fuel cell stack, further investigation into the OER catalyst deactivation mechanisms is necessary to mitigate the degradation due to cell reversal.

Chapter 7

Limitation of Existing Reversal Tolerant Anodes

7.1. Introduction

Industry demands automotive polymer electrolyte fuel cells (PEFCs) that are universally robust and tolerant to random, unexpected occurrences and harsh operation. Although, advanced control schemes can enable this to a degree, it is preferred that the system's material set is sufficiently robust to all possible operating conditions. PEFCs are vulnerable and encounter rapid and catastrophic failure if there is hydrogen blockage and starvation. If unmitigated, the fuel cell will ultimately consume its anode via carbon corrosion, making the entire stack inoperable. Previous chapters discuss the strategy of implementing a material based solution of integrating a catalyst that promotes the harmless water electrolysis over carbon corrosion. Such an electrode, traditionally termed as an RTA, was fabricated by the addition of OER catalyst to the conventional Pt/C based anode. However, there exist challenges with the conventionally used RTA materials. The electrolysis catalyst additive in the RTA fails after only a short duration of cell reversal

(Chapter 5) and under certain conditions, its performance is highly impaired (Chapter 6). Moreover, the effective implementation of the RTA strategy of using a water electrolysis catalyst requires a continuous source of water. In freezing conditions, the mobility of the water may be highly restricted, which might limit the activity of OER catalyst towards water electrolysis. Very little is known about both of these issues. Based on these challenges, the primary objective was to investigate the cause of the failure of an RTA based on OER catalysis. The experiments conducted in this regard have been described in this chapter.

Our findings indicate that the current strategy of adding expensive OER catalysts in the anode, to enhance the durability of automotive fuel cells, is only a temporary solution. RTAs, with OER catalysts, show high vulnerability to temperature and humidity conditions. The interaction of the HOR catalyst, OER catalyst and the carbon support while operating PEFCs under stress conditions is not well understood. The failure of the RTA at water-excess (i.e., at high RH) conditions was unexpected because water is the key reactant for OER. There exist contradictory reports on the role of water on carbon corrosion as well [136], [139], [140]. The effect of water activity on co-existing carbon corrosion and water electrolysis reactions is complicated and has not been investigated before, to the best of our knowledge. The complexity of the electro-thermo-chemical phenomena occurring in a PEFC makes it difficult to pin-point the exact cause of degradation. In order to delineate the electrochemical phenomena under cell reversal conditions, we need to subject each material component of the RTA to the same stress conditions and study their behavior at various operating conditions, mimicking the stress conditions an FCEV can be subjected to. By gaining insight into how each of these

materials influence the overall degradation mechanism when put together in an RTA, we can eventually design a better RTA by engineering the material and the electrode architecture. Our research goals are to fundamentally probe the mechanisms of degradation due to cell reversal and to investigate the reason behind the loss of functionally of the OER catalyst, to enable us to propose an effective strategy to mitigate degradation in fuel cells.

7.2. Anomalous Behavior of OER Catalyst based Anodes

In a PEM electrolyzer, the OER catalysts (like IrO_2) remain active for 1000s of hours [109]. When the same OER catalysts were used within a PEFC anode, they were found to deactivate in about an hour (as for RTA 50 wt% MEAs) [126], [141]. The stability of IrO_2 in an acidic medium subjected to potentials ranging from 0-2.8 V (vs. SHE) is questionable [32], [109], [119], [120], however, from post-mortem analysis of the PEFC anodes, IrO_2 is found to exist in the electrodes even after they fail. Nevertheless, it failed to promote the OER during cell reversal tests for long. The cause of "sudden death" of the RTA after a certain duration of water electrolysis (during cell reversal) in-spite of the physical presence of the OER is unexplored and requires controlled experiments to investigate it

In addition to generally becoming deactivated, the OER catalyst also exhibited anomalous relation to water activity (which is a function of RH). The activity of IrO_2 towards OER should increase with increasing RH, due to higher availability of the reactant (i.e., water). This trend was true through medium RH values (50-70% RH), but the trend was reversed beyond that. We observed a decline in the OER activity and faster

deactivation of the IrO_2 in the PEFC anode at high RH (>70% RH). Higher operating temperature also surprisingly deteriorated the RTA performance. If we compare the total time of first reversal (i.e. water electrolysis time) at 65°C to that at 90°C at similar RH conditions, the latter was found to last for a shorter duration than the former , as shown in Figure 7.1. This was opposite to the trend of increasing catalytic activity with increasing temperature.

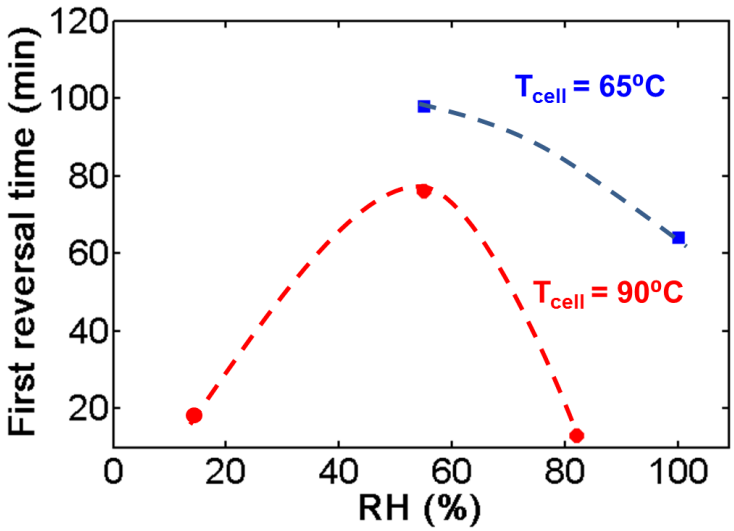

Figure 7.1. The first reversal time for RTA 50 wt% MEAs subjected to cell reversal at 65C and 90C, at medium to high RH conditions. The data points are shown with blue squares and red circles respectively. The dotted lines are trend lines used as visual guides.

In order to identify the cause of the RTA's failure after extended period of cell voltage reversal, the following hypotheses are proposed as the mechanisms for the failure of RTAs:

1. Poisoning of the OER catalyst by organic species generated by minor amounts of carbon corrosions during cell reversal while the anode was still in the electrolysis potential regime.
2. Electronic disconnection of the OER catalyst during reversal due to minor amounts of carbon corrosion in the water electrolysis potential window, which causes the OER catalyst to become electronically insulated.

The anomalous behavior of the OER catalyst (resulting in volcano-type behavior of reversal time with increasing RH) could have the following hypothesized mechanism:

1. There is a competition between the consumption of water for OER and carbon oxidation reaction. The rate of increase in activity of carbon towards oxidation surpasses the rate of increase in activity of IrO_2 towards OER with increasing water activity (or RH) after a certain threshold. A schematic is shown in Figure 7.2(a).

2. The distribution of ionomer, which transports the water to the catalyst and to the carbon support for the reactions, is not uniform. There is a possibility that the ionomer (Nafion®) does not coat the IrO_2 agglomerates as well as it coats the Pt/C nanoparticles, resulting in better water access to the carbon and facilitating higher rate of carbon corrosion at high RH instead of OER at IrO_2. A schematic for the hypothesis is shown in Figure 7.2(b).

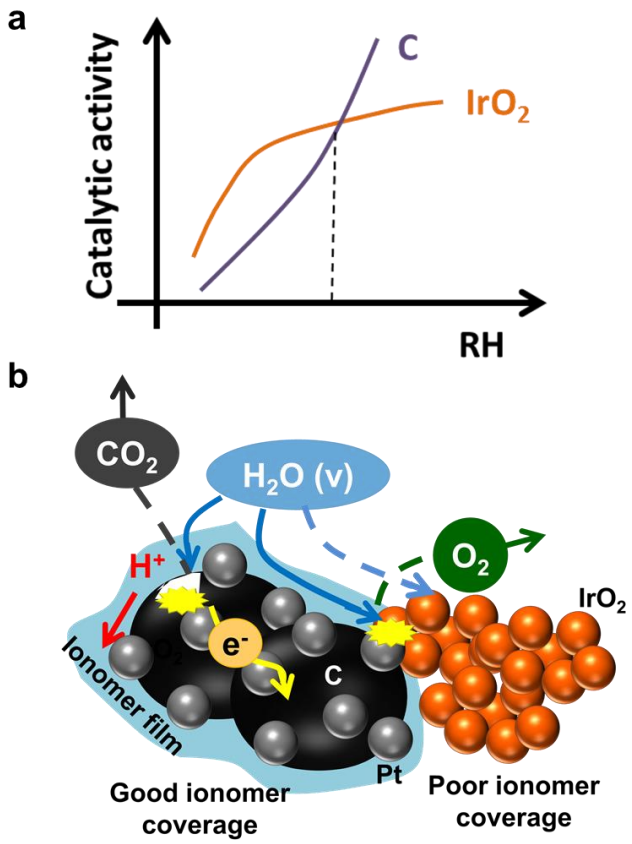

Figure 7.2 (a) Hypothesized trend for the dependence of the rate of OER activity of IrO_2 and the activity of carbon towards carbon oxidation (or corrosion), on water activity (i.e., RH).(b) A schematic for the hypothesis of non-uniform ionomer coverage on IrO_2 particles (or agglomerates) as compare to that on Pt/C.

It is necessary to test the hypotheses in order to mitigate the failure of RTAs. Anodes with each material component of the RTA or with a combination of two components were designed and tested as MEAs in electrolyzer mode. The electrochemical response recorded and the ex-situ elemental and structural mapping, indicated the possible mechanisms for the failure of an OER catalyst in an RTA.

7.3. *In-situ* Electrochemical Diagnostics

The experimental set up and MEAs were designed to simulate the cell reversal conditions on anodes which were fabricated out of one or a combination of components (materials) of conventional RTA anode, so as to delineate the role of each material in degradation due to cell reversal. The composition of the cathode was kept similar to that used for the earlier studies. One set of anodes were fabricated out of IrO_2 in order to test if the OER catalyst tends to get deactivated on its own and was used as a control case to compare the other results. Next, an anode that was fabricated with a combination of IrO_2/C was tested to validate our hypothesis of IrO_2 deactivation in an RTA because of carbon oxidation species. We used Nafion® as the ionomer binder for all anodes to make the transport processes (mainly water and gases) in these systems analogous to that in the MEAs with an RTA. The catalyst ink was prepared such that the volume percentage in the electrode was same as that in the RTA MEAs tested earlier. This would ensure similar ionomer coverage on the catalyst particles.

A fuel cell hardware (designed in-house by former PhD student, Dr. William Epting) was used with certain modifications for the electrochemical diagnostics. The hardware was equipped with a 1 cm^2 serpentine flow field machined on graphite plates. The end plates were made up of aluminum and were paired with gold-plated copper current collectors. Rectangular silicone rubber 15 W (AC) heaters (SRFG-103, Omega, USA) were attached on both the end plates to control the cell temperature. Temperature of the cell was managed using PID controllers with Omega's self-adhesive thermocouple temperature sensors for the temperature input. The thermocouple was attached to the

graphite flow-field of the cathode. A snapshot of the disassembled cell hardware is shown in Figure 7.3. The cell can be operated in either electrolyzer or fuel cell mode. In electrolyzer mode, the anode was supplied with inert gas (e.g. N_2) at varied RH, to replicate the electrochemical test conditions of our prior work. Water electrolysis and/or carbon oxidation will take place at the anode depending of the components in the anode. In order to eliminate carbon from the anode completely, a titanium mesh was used as the GDL instead of a carbon based GDL for the anode, which also served as the flow field. The copper current collector on the anode side was replaced by a titanium sheet (100 µm thick), because of the corrosion resistant nature of Ti; and paired with another piece of Ti sheet with gas inlet and outlet ports and alignment holes machined onto it. In electrolyzer mode, the cathode will receive protons from the anode through the PEM (Nafion® 211, same as that used for the RTA MEAs) and support hydrogen evolution reaction (HER). In fuel cell mode, the cathode can perform ORR while under "cell reversal" conditions. However, the overpotentials in the cathode due to ORR will affect the cell potential while operating the cell at different RH conditions and introduce artifacts in the anode potential reading if the anode and cathode potential is not monitored separately. However, if the cell is operated in electrolyzer mode, the cathode potential will be nearly 0 V (vs. SHE) due to low overpotentials associated with HER. Thus, the cell potential will be equivalent to the anode potential. Monitoring the cell potential while operating the cell in galvanostatic mode will give us insight on the electrochemical activity of each component towards OER and/or carbon oxidation. The individual catalyst/element testing as the anode will also give us a direct evidence of the deactivation of the IrO_2 as well as that of Pt for OER, in the presence or absence of carbon. The following sub-sections

describe the tests that have been performed and the preliminary results, as well as the challenges faced and discussion of the possible solutions.

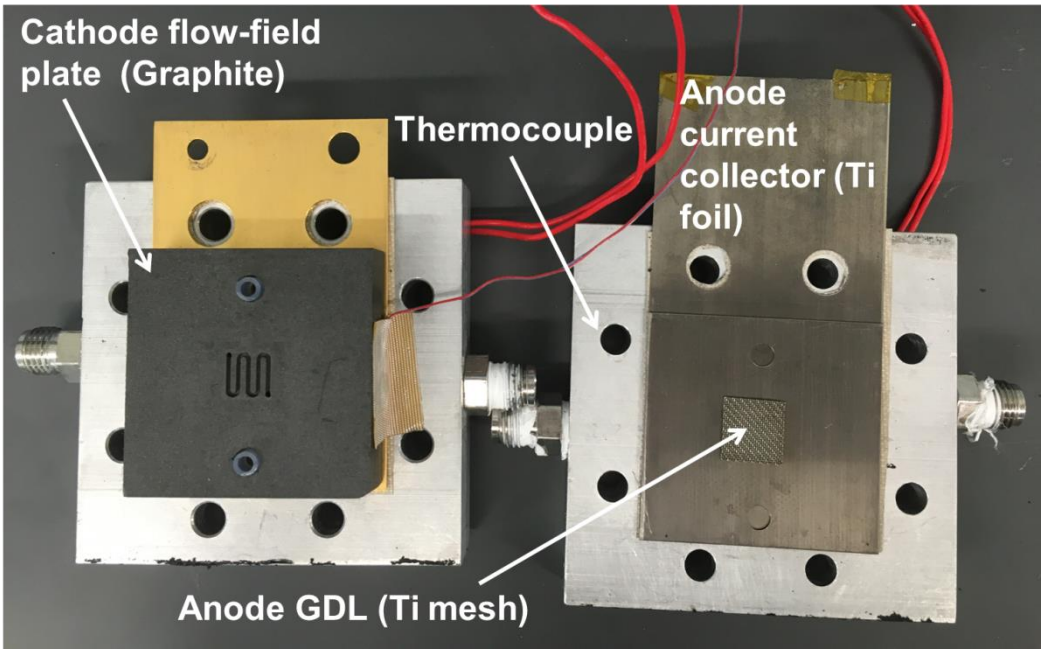

Figure 7.3. Image of the disassembled electrolysis cell hardware.

7.3.1. Electrolyzer with IrO_2 and IrO_2/C Anodes

Two batches of electrodes were prepared to test our first set of hypotheses for OER catalyst deactivation. One batch contained IrO_2 (99.9% purity, Sigma-Aldrich) mixed with 5 wt% Nafion® dispersion (D521, Alfa Aesar) and additional deionized (DI) water such that the solvent was 4:1 DI water: isopropanol (IPA). The solid percentage in the catalyst ink was 5 wt%. The ink was dispersed by 30 min ultrasonication (using a sonic bath) and stirred for 24 hours on a magnetic stirrer before coating a glass-fiber reinforced PTFE film. A 9 cm^2 area was coated with the catalyst ink and allowed to dry in ambient conditions for 24 hours. The amount of ink applied to the PTFE film was predetermined to obtain a loading of 5 mg of IrO_2 on a 1 cm^2 area of the electrode (The

loading was also verified by measuring the film before and after decal transfer). The film was then cut into 1 cm × 1 cm pieces to be used for decal transfer [13], [111], [142] onto a Nafion® membrane to fabricate the electrolyzer anode (details in Appendix I). An identical protocol was used for the IrO_2/C anode fabrication. The amount of carbon (Vulcan XC 72R) in the catalyst ink was calculated such that the electrode would have 10% by volume of carbon and 5 mg/cm^2 of IrO_2. A commercial GDE (Fuel Cell Store, Texas, USA) with 0.3mg/cm² Pt loading (using 40% Pt/C catalyst) was coated on a Sigracet 29BC Carbon Paper GDL was used as the cathode. PTFE based gaskets were used for both the anode and the cathode. The cathode GDE was heat-pressed onto the PEM to ensure low contact resistance at the cathode-membrane interface. The MEA with 1 cm^2 active area was then assembled into the cell hardware (with Ti mesh as anode GDL).

The cell was heated to 65°C and a constant current of 0.2 A was applied to the cell while recording the cell voltage. This mimicked the case of fuel starvation and cell reversal for the PEFCs tested. 100% water-saturated N_2 (inert) gas was supplied to both the anode and cathode at a constant flow rate of 0.1 slpm (high-stoichiometric flow rate). The MEA with only IrO_2 as the anode was conditioned by cycling the anode through 0.01 to 0.2 A current in steps for 8 hours before the chronopotentiometric test. The gas flow rate and humidification was controlled using the fuel cell test stand (850e, Scribner Associates Inc., USA) and the electrochemical tests were performed using a potentiostat (VSP, Bio-Logic, France). The conditioning step was skipped for the IrO_2/C MEA to prevent any interference with the quantification of the total OER time at a current density of 0.2 A/cm^2, so that we can compare it with the PEFC reversal time. Polarization curve

for the IrO_2 anode was also measured before and after the chrono-potentiometric test and a negligible change in the performance was observed. The overpotentials for the PEM electrolyzer however, were pretty high (i.e. poor performance w.r.t conventional PEM electrolyzers [109], [143]) and it could have resulted from poor electronic conductivity and mass transport resistances. The performance could be improved by optimizing the anode fabrication method and cell assembly. Figure 7.4 shows the duration of OER for the two kinds of MEAs with the upper bound for anode potential (~ cell potential) being 6 V (the highest anode potential limit set for the RTA tests was 3.3 V). The IrO_2 anode sustained OER with anode potential of <2 V for more than 100 hours which was >100 times the total cell reversal time survived by RTA 50 wt% MEA (given that the loading of IrO_2 in the electrolyzer anode was 100 times). This indicated that IrO_2 does not deactivate for water electrolysis on its own. However, the anode with carbon had its potential rise beyond 3.3 V in about 10 min. The potential ascent was steep, similar to that observed in PEFCs during cell reversal. The initial anode potential for OER was also higher than that of the IrO_2 anode. This observation suggests that the presence of carbon triggers the deactivation of IrO_2 towards the OER and increases the anode potential, which can lead to catastrophic failure of the PEFC. The use of 10 vol% of carbon ensured that the carbon is not the backbone of electronic connectivity of the IrO_2 particles. Hence, we can conclude that the failure of the electrolysis cell was not due to carbon corrosion or carbon loss leading to electronically isolated IrO_2 agglomerates. One of the possible reasons for failure could be: some carbon oxidation species poisoning the IrO_2 catalyst to render it electrochemically inactive for OER. X-ray photoelectron spectroscopy on the failed anodes can provide information of the poisoning species. Similar to the RTA

MEAs, on repeating the test, the low potential dwelling time was even shorter; the cell reached the potential cut-off in a minute. A second possibility could be poor mass transport characteristics of the anode with the ionomer preferentially coating the carbon instead of the IrO_2 agglomerates. Another MEA with the same anode failed to sustain OER for longer than 10 minutes (i.e., maintain low anode potentials) even when a lower current of 0.1 A cm^{-2} was drawn through the electrolysis cell.

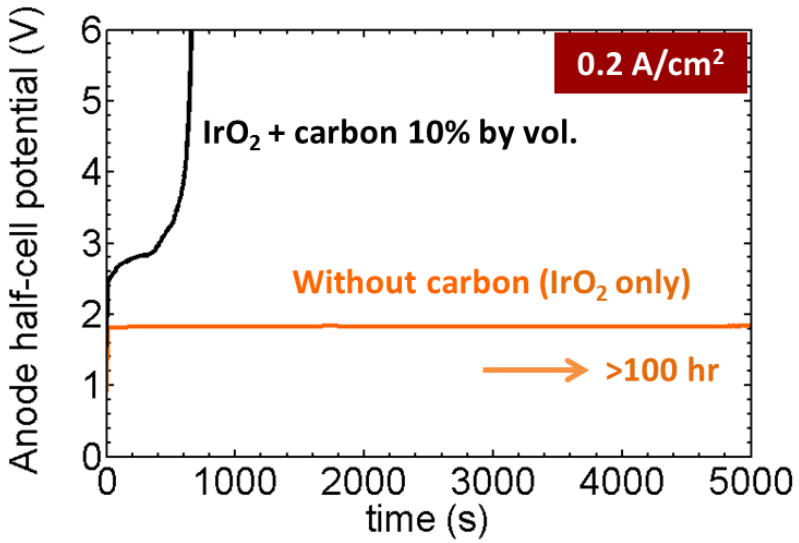

Figure 7.4. Cell potential (equivalent to anode half-cell potential) during OER in PEM electrolyzer operated at 0.2 A cm^{-2}.

The irreversibility of such a poisoning was confirmed when the OER dwelling time was not affected even after subjecting the anode to a reducing environment and potential cycling during CV measurements. CV measurements were done on both kinds of anodes at the beginning of life condition and after the test (in case of IrO_2/C anode, after failure and in case of IrO_2 after 10 hours of OER). The CVs are shown in Figure 7.4. For the CV measurement, H_2 was supplied to the cathode and N_2 at the anode at 0.1 slpm with the cell at 65°C and 100% RH. The CV pattern of the IrO_2 anode at BOL shows

significant IrO_2 electrochemical surface area. The surface area reduces by a small amount after 10 hours of OER, which is due to instability and dissolution of IrO_2 in acidic medium of the PEM electrolyzer. The IrO_2/C anode, however, did not show any significant IrO_2 surface area even at BOL, and the area within the CV curve reduced further on use, showing almost no electrochemical surface area of the catalyst [109], [143], [144]. The BOL CV shows Ohmic characteristics. This could have possibly been caused by non-uniform and poor ionomer distribution leading to low electrochemically active surface area and poor protonic conductivity as well.

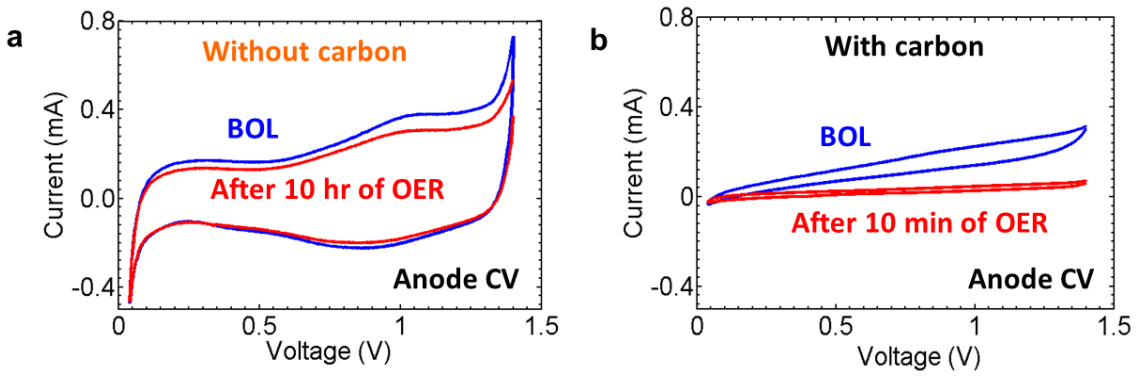

Figure 7.5 (a) Anode CVs at BOL and after 10 hr of OER in MEA with IrO_2 anode (b) Anode CVs at BOL and after 10 min of OER (i.e. after failure) of MEA with IrO_2/C anode.

Anodes fabricated using the same composition and protocol were tested with lower RH (60% RH), however the potential recorded was unsteady and, even for the IrO_2 anode, the cell potentials recorded were higher than 3 V from the beginning of the current-hold test. This disallowed us to test the second set of hypotheses to unravel the cause of the volcano-type dependence of RTA durability with increasing RH.

7.3.2. Challenges for In-house Electrolyzer and Possible Solutions

The possibility of poor ionomer distribution in the electrolyzer anode was verified using SEM and Energy-dispersive X-ray spectroscopy (EDX). The IrO_2 in the anode was heavily agglomerated (shown in Figure 7.6), which reduces the utilization of the OER catalyst.

The ionomer coating on the agglomerates also appeared scarce. The EDX signal obtained from F, Ir, O, and C for an area on the IrO_2/C anode surface is shown in Figure 7.7. The signal intensity of F and Ir appears complementary to each other; implying that, the ionomer (PFSA) coating on the IrO_2 agglomerates was poor. The C and F signal appears to overlap in the images, indicating preferential coating of the carbon particles. This explains the poor OER performance of the IrO_2 anode as well as the Ohmic nature of the IrO_2/C anode and high overpotentials for OER reaction. Poor distribution of ionomer not only increases the Ohmic resistance due to poor proton conductivity, but also increases mass transport losses because the water in vapor form needs to diffuse through the ionomer to reach the catalytic surface for OER to take place. This issue is not encountered for conventional PEM electrolyzers, because they use liquid water as the reactant [143], [145]–[148]. The same reason resulted in unsuccessful experiments for investigating the anomalous behavior of IrO_2 with lower RH. When the RH was reduced below 100%, the OER potential increased to above 3 V even for the IrO_2 anode. Using current densities as low as 0.05 A cm^{-2}, the anode could sustain the OER at potentials around 2 V. However, that was not enough to perform rigorous experiments to measure the activity of the catalyst at different RH.

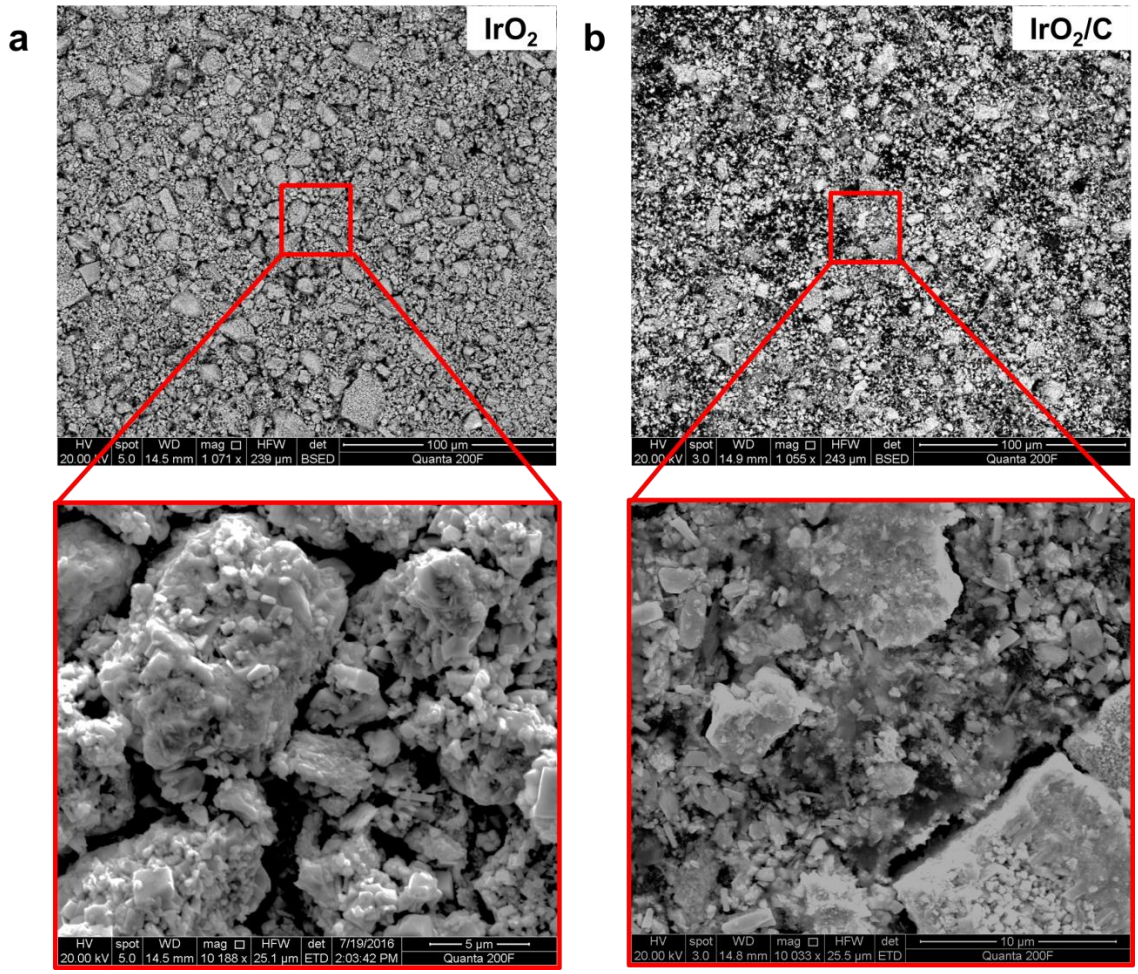

Figure 7.6. SEM images of electrolyzer anode surfaces with IrO_2 (a) and IrO_2/C (b). The zoomed in images of the red box bounded areas are shown below the corresponding images. Secondary electron detector was used. The bright agglomerated volumes were primarily composed of IrO_2.

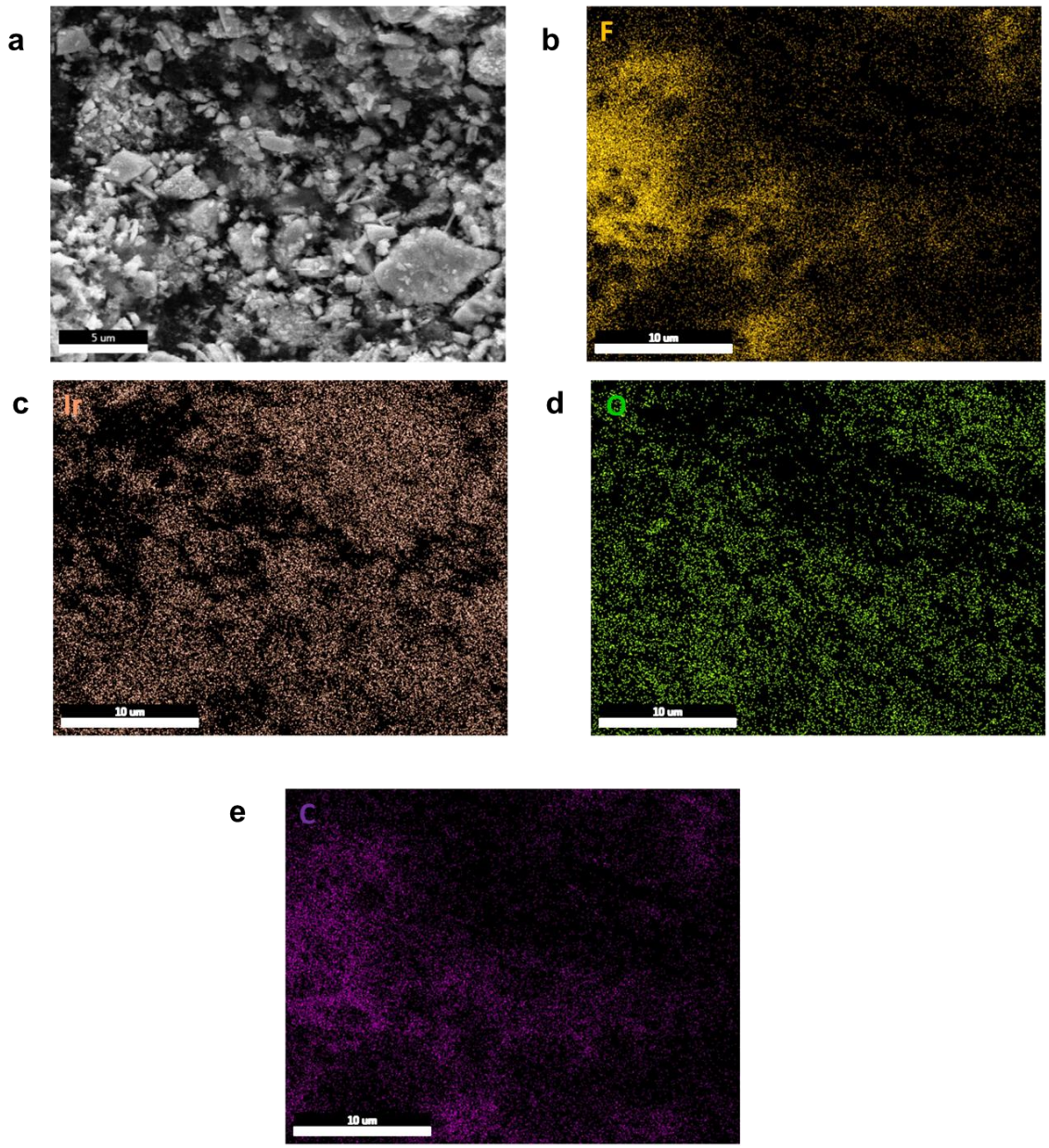

Figure 7.7. Areal elemental map of IrO2/C anode obtained from EDX. (a) SEM image of the area mapped. (b)-(e) Map for F, Ir, O and C respectively.

A way to alleviate the current challenges is to ensure good catalyst ink dispersion. The high-energy sonicator, e.g. an ultrasonication probe might have been useful to obtain

a better dispersion of the ionomer as well as reduce the agglomerate size, making the OER catalyst more effective. The cell assembly should also be optimized to reduce the contact resistances. For this study, the gasket thickness for the anode was selected such that it was 5% lower than the average thickness of the Ti mesh, which was used as the GDL; in order to ensure good contact between the incompressible Ti mesh and the Ti current collector.

When a steady voltage measure can be successfully obtained from the electrolyzer MEAs, polarization curves can be measured for IrO_2 anode at different RH and temperature conditions, from which the catalytic activity of IrO_2 can be obtained as a function of temperature and RH. Similar activity function can be obtained for carbon for carbon corrosion reaction, but using a carbon anode without any catalyst. This will shed light on the reason behind the anomalous volcano type behavior of the RTA MEA with increasing RH.

7.4. Conclusion

The deactivation of OER catalyst for water electrolysis in a PEFC electrode after short time duration was caused by the presence of carbon. The potentials of water electrolysis are conducive to carbon oxidation. The carbon oxidative species could have possibly poisoned the catalyst critically. Any species irreversibly adsorbed onto the OER catalyst surface could also have reduced the electrochemically active surface area of the catalyst. It was also found that the tendency of IrO_2 to agglomerate into large particles reduces the utilization of the catalyst. The ionomer distribution also plays an important role in increasing the effectiveness of the OER catalyst by providing a low resistive

pathway for proton transport. The durability of an RTA which uses OER catalyst can be improved by optimizing the electrode fabrication and catalyst ink formulation such that a better dispersion, smaller agglomerates and good ionomer coverage of the catalyst is obtained.

Chapter 8

Conclusions and Future Directions

8.1. Summary

In this dissertation, one of the degradation phenomenon that affect the durability of a PEM fuel cell has been investigated. Cell reversal, which is an outcome of hydrogen starvation at the anode, causes severe degradation and eventually leads to cell failure. A single cell failure in a fuel cell stack used in an FCEV will shut down the whole stack power. Hence, it is necessary to implement a strategy to prevent catastrophic cell failure. System-level control strategies interfere with the operation of the fuel cell stack and challenge the reliability of the operation; hence, a material based solution has been implemented for the current study. In this dissertation, a water-electrolysis (i.e., OER) catalyst has been added to a conventional anode, in order to promote water-electrolysis and prevent carbon corrosion during hydrogen starvation. This slowed down the rate of degradation of the cell performance and made the cell tolerant to reversal conditions for 10 to 30 times longer than a conventional PEFC anode. However, in order to ensure 5000+ hours of life of a fuel cell stack for a mid-size vehicle, the target is to make a cell

survive at least 10 hours of cell reversal conditions, which has not been achieved yet. Increasing the loading of the OER catalyst increases the reversal tolerance time[14], [126], [149], but, as a result of these catalysts being based on precious metals, the system cost increases, making it even more challenging to meet the DOE cost target for PEFCs. Moreover, from the current study, it was found that, although the increase in reversal tolerance time scaled with the increase in loading, it did not scale well with the rate of degradation during cell reversal. This was because of inefficient distribution of the catalyst particles in the electrode. The OER catalyst forms large agglomerates when used in high loading in the electrodes. Agglomeration leads to low utilization of the catalyst as well as high mass transport losses. This was similar to the relation of the cathode catalyst-layer structure to the transport characteristics affecting the overall cell performance.

The anodes with OER catalyst additions were also tested for their effectiveness in different fuel cell operating conditions. The role of relative humidity (i.e., water activity) was found to be very crucial to the performance of the catalyst, which in-turn determines the reversal tolerance of the cell. A volcano-type relation was observed for the OER catalyst used in the RTAs with respect to the water activity, though the cause is not fully clear. These are useful for designing the anodes and determining favorable operating conditions for the fuel cell stack.

Mechanisms for deactivation of the OER catalyst in an RTA have been proposed and experiments were designed to validate the hypotheses. It was found that the presence of carbon in the electrode, severely limits the water-electrolysis activity of the OER catalyst. The morphology of the electrode was again found to be significantly affecting the performance of the PEM electrolyzer anodes that were tested for validating the

proposed mechanisms. Some of the hypotheses could not be successfully tested because of poor ionomer coverage on the OER catalyst particles, severely limiting the OER activity when water is supplied in vapor form.

Further optimization of the in-house electrode fabrication method is required to test all the hypotheses. An efficient strategy to mitigate degradation due to cell reversal can be achieved after gaining a complete understanding of the deactivation mechanism of the OER catalyst. Besides, investigating and implementing better electrode architecture and material, other possible means of protecting the fuel cell from carbon corrosion are discussed in the following section.

8.2. Future directions

The primary goal should be to achieve longer durability along with cost optimization. The low utilization of expensive OER catalyst in an RTA can be minimized by preventing agglomeration of the catalyst particles and thus increasing the electrochemically active surface area and improving catalyst utilization. OER catalysts, like IrO_2, are very prone to aggregation and hence, the catalyst-layer fabrication method would need to be modified for making the RTAs. High energy dispersion for the catalyst ink will help break the agglomerates in solution before coating it on the membrane, GDL or decal substrate. The ultrasonicator-bath used for the in-house electrode for the experiments described in Chapter 7 was not capable of preventing agglomeration, as was observed from the SEM images, which depicted the micron sized IrO_2 agglomerates in the anode catalyst-layer. A sonication probe which can be dipped within the ink in a vial to agitate and mix the dispersion could have been more efficient in reducing

agglomeration. Likewise, the fabrication method of the RTAs should be optimized to obtain a better distribution of the OER catalyst and thus prolong its durability. Besides high-energy dispersion of catalyst ink, the solvent can be modified and surfactants can be added to the catalyst ink formulation that will refrain the catalyst nanoparticles from aggregating.

From Chapter 7, it was also found that the IrO_2 agglomerates have poor ionomer coverage, which increases the OER overpotential for low RH operation of the cell. In the fuel cell MEAs with RTA, the Nafion® is likely to form a uniform coating on the Pt/C catalyst particles rather than on the IrO_2 agglomerates. This makes water transport to the OER sites at low humidity conditions difficult. Assuming that IrO_2 is most active for OER when water is available in liquid form, the OER activity will be poor at low humidity conditions. Nafion® is believed to transport water through the PFSA network and polymer nano-channels in liquid form[25], [150], [151]. The lack of Nafion® coverage on IrO_2 agglomerate, while the Pt/C has good coverage, can also explain the reduced reversal time at high RH conditions. At high RH, the water transport rate to the carbon might have been faster than that to the IrO_2, thus the protonic and reactant transport resistances being lower for carbon corrosion reaction than OER, the anodes degraded faster resulting in shorter reversal time. It is hence crucial to ensure good ionomer coverage on the OER catalysts to reduce the reactant diffusion and protonic transport resistances for OER at low activation losses during cell reversal. The ionomer dispersion can be improved by changing the solvent for catalyst ink dispersion [152]–[154]. Pre-treated OER catalyst particles can be employed, such that the ionomer film coats them. The catalyst-layer fabrication can also be done by hot-pressing dry-ink

dispersion onto the PEM [155], [156]. The morphology of the electrodes should be characterized in order to find the best method of fabricating the RTAs.

After the OER catalyst utilization is improved by better electrode designing strategies, the effectiveness of the RTA should be tested for freeze start conditions as well. The possibility of fuel starvation is higher when an FCEV is subjected to freezing temperatures, when frozen water can cause blockage in fuel channels or anode pores. Low temperature (below - 20°C) can cause water to be immobilized within the ionomer as well as in the electrode pores [157]. The activity of OER catalyst at such low temperatures with mobilized or immobilized water needs to be investigated in a PEFC electrode, to develop degradation mitigation strategies for freezing temperatures.

The root cause of cell failure due to cell reversal, electrocatalyst degradation in cathode and anode due to transients during fuel cell operation is carbon corrosionas depicted in Figure 8.1 (a). Thus using a corrosion resistant catalyst support can alleviate the cause of degradation. Carbon based catalyst support, such as carbon-nanotubes, carbon-nanofibers, modified graphene, surface-functionalized carbon, etc. that are more resistant to corrosion than Vulcan XC-72R which is the most commonly used carbon support in PEFCs [157], [158], should be used. An example of a well-dispersed OER catalyst with good ionomer coverage and possibly supported on a low-surface area carbon nanoparticles is shown in Figure 8.1 (b).

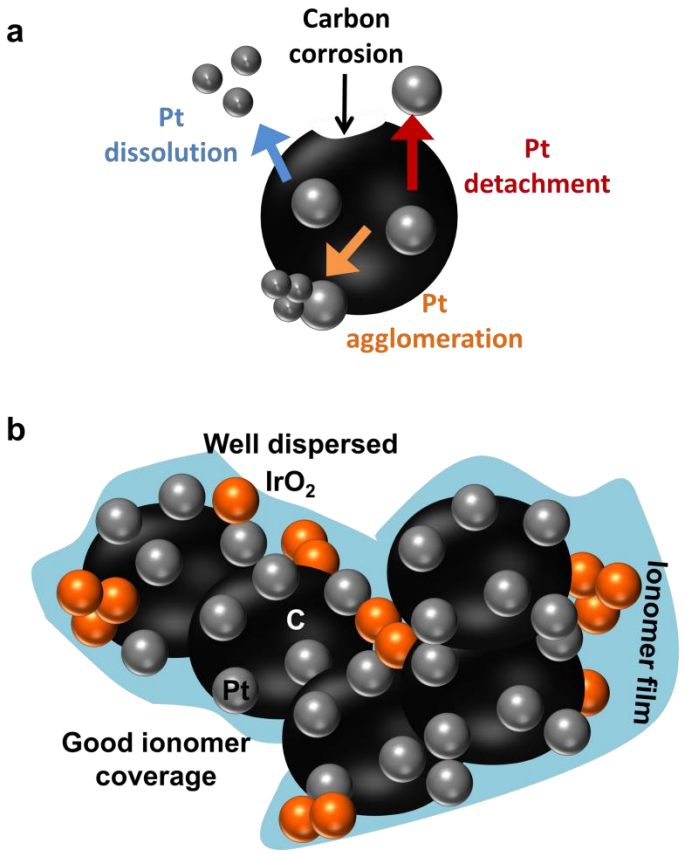

Figure 8.1. (a) Schematic of catalyst degradation caused by carbon loss due to the carbon corrosion reaction. (b) Schematic of a well-dispersed OER catalyst (IrO_2), in a Pt/C matrix with good ionomer coverage for an effective RTA design.

There exist studies in literature, proposing the use of metal oxide based support for Pt catalyst, such as SnO_2, TiO_2, IrO_2, TiB_2, ITO, etc., which are not only corrosion resistant, but can also support OER for sustaining the load during fuel starvation without degrading the electrode structure and components [159]–[162]. However, most of the oxide-supports suffer from poor electronic conductivity and lower surface area than the porous carbon support that are currently highly developed and is the state-of-the-art catalyst support for PEFCs, for providing highest Pt activity, ECSA and stability [157].

Some researchers have proposed a hybrid catalyst support by pairing corrosion resistive carbon support with oxides, such that high surface area with several catalyst loading sites and good electronic conductivity are available along with the protection from corrosion due to preferential OER on the metal-oxides or other OER catalyst used [158]. There are however very few studies on alternative catalyst support for use in PEFC electrodes to prevent degradation due to catalyst support corrosion, and the new materials need to be optimized and tested for long term durability and catalytic activity retention in form of an MEA before it can be implemented commercially. The cost of production of such supports also needs to be substantially lowered for industrial adoption of the materials. Moreover, the GDL, which has carbon in it, is also susceptible to carbon corrosion. Removing carbon from the electrode will not be sufficient to prevent degradation due to cell reversal, load cycling and start-up/shut-down of fuel cell stacks. The GDL also needs to be engineered or the carbon GDL could be completely replaced by metal-oxide foam, which has its own limitations due to high material and manufacturing costs as well has high bulk and contact resistances [157].

References

[1] H. He, S. Averick, P. Mandal, H. Ding, S. Li, J. Gelb, N. Kotwal, A. Merkle, S. Litster, and K. Matyjaszewski, "Multifunctional Hydrogels with Reversible 3D Ordered Macroporous Structures," *Adv. Sci.*, vol. 2, no. 5, p. n/a–n/a, 2015.

[2] *Monthly Energy Review October 2015*. U.S. Energy Information Administration, 2015.

[3] D. Papageorgopoulos, "Fuel Cells Program -Plenary Presentation," *Fuel Cell Technol. Off.*, 2015.

[4] S. Litster and G. McLean, "PEM fuel cell electrodes," *J. Power Sources*, vol. 130, no. 1–2, pp. 61–76, 2004.

[5] A. P. Mandal, W. K. Epting, A. Kumar, S. K. Babu, and S. Litster, "Morphological Characterization of Energy Materials using Nanoscale X-ray CT," p. 8511.

[6] J. Larminie and A. Dicks, *Fuel Cell Systems Explained*, vol. 93. 2001.

[7] J. T. Gostick, M. a. Ioannidis, M. D. Pritzker, and M. W. Fowler, "Impact of Liquid Water on Reactant Mass Transfer in PEM Fuel Cell Electrodes," *J. Electrochem. Soc.*, vol. 157, no. 4, p. B563, 2010.

[8] K. Seidenberger, M. Klages, F. Wilhelm, and J. Scholta, "Investigations on the Morphology and Water Inventory of GDLs Using µ-Computer Tomography and Monte Carlo Modeling," *ECS Trans.*, vol. 42, no. 1, pp. 179–190, 2012.

[9] T. Sasabe, P. Deevanhxay, S. Tsushima, and S. Hirai, "Investigation on the effect

of microstructure of proton exchange membrane fuel cell porous layers on liquid water behavior by soft X-ray radiography," *J. Power Sources*, vol. 196, no. 20, pp. 8197–8206, 2011.

[10] S. Kim, B.-H. Jeong, B. K. Hong, and T.-S. Kim, "Effects of hydrophobic agent content in macro-porous substrates on the fracture behavior of the gas diffusion layer for proton exchange membrane fuel cells," *J. Power Sources*, vol. 270, pp. 342–348, 2014.

[11] T. Kotaka, O. Aoki, T. Shiomi, Y. Fukuyama, N. Kubo, and Y. Tabuchi, "The Influence of Micro Structure of the GDL and MPL on the Mass Transport in PEFC," *ECS Trans.*, vol. 41, no. 1, pp. 439–448, 2011.

[12] S. Mandal, Pratiti, Litster, "Morphological analysis of polymer electrolyte fuel cell electrode using high resolution X-ray computed tomography and subsequent performance analysis," *ECS Trans.*, vol. 58, no. 1, pp. 481–488, 2013.

[13] M. S. Saha, D. K. Paul, B. A. Peppley, and K. Karan, "Fabrication of catalyst-coated membrane by modified decal transfer technique," *Electrochem. commun.*, vol. 12, no. 3, pp. 410–413, 2010.

[14] S. Mandal, Pratiti, Hong, Bo Ki, Oh, Jong-Gil, Litster, "3D Imaging of Fuel Cell Electrode Structure Degraded Under Cell Voltage Reversal Conditions Using Nanoscale X-ray Computed Tomography Pratiti Mandal," vol. 69, no. 17, pp. 443–453, 2015.

[15] F. B. O'Hayre, Ryan, Cha, Suk-Won, Colella, Whitney, Prinz, *Fuel Cell*

Fundamentals, 2nd ed. John Wiley & Sons, 2009.

[16] J. Wu, X. Yuan, H. Wang, M. Blanco, J. Martin, and J. Zhang, "Diagnostic tools in PEM fuel cell research: Part I Electrochemical techniques," *Int. J. Hydrogen Energy*, vol. 33, no. 6, pp. 1735–1746, Mar. 2008.

[17] I. A. Schneider, D. Kramer, A. Wokaun, and G. G. Scherer, "Effect of inert gas flow on hydrogen underpotential deposition measurements in polymer electrolyte fuel cells," *Electrochem. commun.*, vol. 9, no. 7, pp. 1607–1612, Jul. 2007.

[18] K. Punyawudho, D. A. Blom, J. W. Van Zee, and J. R. Monnier, "Comparison of different methods for determination of Pt surface site concentrations for supported Pt electrocatalysts," *Electrochim. Acta*, vol. 55, no. 19, pp. 5349–5356, Jul. 2010.

[19] W. K. Epting, J. Gelb, and S. Litster, "Resolving the three-dimensional microstructure of polymer electrolyte fuel cell electrodes using nanometer-scale X-ray computed tomography," *Adv. Funct. Mater.*, vol. 22, no. 3, pp. 555–560, 2012.

[20] S. Zhang, R. Klimentidis, and P. Barthelemy, "Porosity and permeability analysis on nanoscale FIB-SEM 3D imaging og shale rock," *Int. Symp. Soc.*, pp. 1–12, 2011.

[21] Y. Katayanagi, T. Shimizu, Y. Hashimasa, N. Matsushita, Y. Yamazaki, and T. Yamaguchi, "Cross-sectional observation of nanostructured catalyst layer of polymer electrolyte fuel cell using FIB/SEM," *J. Power Sources*, vol. 280, pp. 210–216, 2015.

[22] K. Punyawudho, N. Vorayos, Y. Zhang, S. Shimpalee, and J. R. Monnier,

"Identification and quantification of performance losses for PEM fuel cells as determined by selective chemisorption and ESA measurements," *Int. J. Hydrogen Energy*, vol. 39, no. 21, pp. 11110–11119, 2014.

[23] D. a. Blom, J. R. Dunlap, T. a. Nolan, and L. F. Allard, "Preparation of Cross-Sectional Samples of Proton Exchange Membrane Fuel Cells by Ultramicrotomy for TEM," *J. Electrochem. Soc.*, vol. 150, p. A414, 2003.

[24] M. Lopez-Haro, L. Guétaz, T. Printemps, A. Morin, S. Escribano, P.-H. Jouneau, P. Bayle-Guillemaud, F. Chandezon, and G. Gebel, "Three-dimensional analysis of Nafion layers in fuel cell electrodes," *Nat. Commun.*, vol. 5, p. 5229, 2014.

[25] S. Yakovlev, N. P. Balsara, and K. H. Downing, "Insights on the study of nafion nanoscale morphology by transmission electron microscopy," *Membranes (Basel).*, vol. 3, no. 4, pp. 424–439, 2013.

[26] D. Bessarabov, D. S. Afcc, and D. G. Inrs, "STXM - in situ applications • Motivation • Eectrochromic devices As 2p XRF-XAS stack," *Fuel Cells*, no. May, 2011.

[27] a. P. H. and J. S. D. Susac, V. Berejnov, "STXM Characterization of PEM Fuel Cell Catalyst Layers," *ECS Trans.*, vol. 50, no. 2, pp. 405–413, 2012.

[28] D. Susac, V. Berejnov, A. P. Hitchcock, and J. Stumper, "STXM Study of the Ionomer Distribution in PEM Fuel Cell Catalyst Layers," *ECS Trans.*, vol. 41, no. 1, pp. 629–635, 2011.

[29] D. Guay, J. Stewart-Ornstein, X. Zhang, and A. P. Hitchcock, "In Situ Spatial and

Time-Resolved Studies of Electrochemical Reactions by Scanning Transmission X-ray Microscopy," *Anal. Chem.*, vol. 77, no. 11, pp. 3479–3487, 2005.

[30] R. Sivakumar, R. Gopalakrishnan, M. Jayachandran, and C. Sanjeeviraja, "Investigation of x-ray photoelectron spectroscopic (XPS), cyclic voltammetric analyses of WO 3 films and their electrochromic response in FTO / WO 3 / electrolyte / FTO cells," *Smart Mater. Struct.*, vol. 15, no. 3, pp. 877–888, 2006.

[31] T. J. Schmidt, M. Noeske, H. A. Gasteiger, R. J. Behm, P. Britz, and H. Bonnemann, "PtRu alloy colloids as precursors for fuel cell catalysts - A combined XPS, AFM, HRTEM, and RDE study," *J. Electrochem. Soc.*, vol. 145, no. 3, pp. 925–931, 1998.

[32] E. Ortel, T. Reier, P. Strasser, and R. Kraehnert, "Mesoporous IrO_2 films templated by PEO-PB-PEO block-copolymers: Self-assembly, crystallization behavior, and electrocatalytic performance," *Chem. Mater.*, vol. 23, no. 13, pp. 3201–3209, 2011.

[33] A. Taniguchi, T. Akita, K. Yasuda, and Y. Miyazaki, "Analysis of electrocatalyst degradation in PEMFC caused by cell reversal during fuel starvation," *J. Power Sources*, vol. 130, no. 130, pp. 42–49, 2004.

[34] S. Litster, K. Hess, W. Epting, and J. Gelb, "Catalyst Layer Analysis: Nanoscale X-ray CT, Spatially-Resolved In Situ Microscale Diagnostics, and Modeling," *ECS Trans.*, vol. 41, no. 1, pp. 409–418, 2011.

[35] E. C. S. Transactions and T. E. Society, "Catalyst layer analysis: Nanoscale X-ray

CT, spatially-resolved," vol. 41, no. 1, pp. 409–418, 2011.

[36] Y. Wang, Y. K. Chen, and W. K. Chiu, "In Situ 3D Imaging and Characterization of Nano-Structures with X-ray Nano-CT Technique," *ECS Trans.*, vol. 35, no. 24, pp. 21–29, 2011.

[37] N. Khajeh-Hosseini-Dalasm, T. Sasabe, T. Tokumasu, and U. Pasaogullari, "Effects of polytetrafluoroethylene treatment and compression on gas diffusion layer microstructure using high-resolution X-ray computed tomography," *J. Power Sources*, vol. 266, pp. 213–221, 2014.

[38] K. B. Wiles, F. Wang, and J. E. McGrath, "Directly copolymerized poly(arylene sulfide sulfone) disulfonated copolymers for PEM-based fuel cell systems. I. Synthesis and characterization," *J. Polym. Sci. Part A Polym. Chem.*, vol. 43, no. 14, pp. 2964–2976, Jul. 2005.

[39] R. Hiesgen, S. Helmly, I. Galm, T. Morawietz, M. Handl, and F. K. Andreas, "Microscopic analysis of current and mechanical properties of nafion?? studied by atomic force microscopy," *Membranes (Basel).*, vol. 2, no. 4, pp. 783–803, 2012.

[40] D. A. Bussian, J. R. O'Dea, H. Metiu, and S. K. Buratto, "Nanoscale current imaging of the conducting channels in proton exchange membrane fuel cells," *Nano Lett.*, vol. 7, no. 2, pp. 227–232, 2007.

[41] T. Awatani, H. Midorikawa, N. Kojima, J. Ye, and C. Marcott, "Morphology of water transport channels and hydrophobic clusters in Nafion from high spatial resolution AFM-IR spectroscopy and imaging," *Electrochem. commun.*, vol. 30,

pp. 5–8, 2013.

[42] Y. Wang, “High-Resolution 3D Imaging and Material Analysis with Transmission X-ray Microscopy and Nano-CT,” *Charact. Mater.*, pp. 1–10, 2012.

[43] I. V. Zenyuk, D. Y. Parkinson, G. Hwang, and A. Z. Weber, “Probing water distribution in compressed fuel-cell gas-diffusion layers using X-ray computed tomography,” *Electrochem. commun.*, vol. 53, pp. 24–28, Apr. 2015.

[44] R. Satija, D. L. Jacobson, M. Arif, and S. A. Werner, “In situ neutron imaging technique for evaluation of water management systems in operating PEM fuel cells,” *J. Power Sources*, vol. 129, no. 2, pp. 238–245, Apr. 2004.

[45] T. A. Trabold, J. P. Owejan, D. L. Jacobson, M. Arif, and P. R. Huffman, “In situ investigation of water transport in an operating PEM fuel cell using neutron radiography: Part 1 – Experimental method and serpentine flow field results,” *Int. J. Heat Mass Transf.*, vol. 49, no. 25–26, pp. 4712–4720, Dec. 2006.

[46] J. P. Owejan, T. A. Trabold, D. L. Jacobson, D. R. Baker, D. S. Hussey, and M. Arif, “In situ investigation of water transport in an operating PEM fuel cell using neutron radiography: Part 2 – Transient water accumulation in an interdigitated cathode flow field,” *Int. J. Heat Mass Transf.*, vol. 49, no. 25–26, pp. 4721–4731, Dec. 2006.

[47] J. B. Siegel, X. Lin, A. G. Stefanopoulou, D. S. Hussey, D. L. Jacobson, and D. Gorsich, “Neutron Imaging of Lithium Concentration in LFP Pouch Cell Battery,” *J. Electrochem. Soc.*, vol. 158, no. 5, p. A523, 2011.

[48] R. T. Atanasoski, D. a. Cullen, G. D. Vernstrom, G. M. Haugen, and L. L. Atanasoska, “A Materials-Based Mitigation Strategy for SU/SD in PEM Fuel Cells: Properties and Performance-Specific Testing of IrRu OER Catalysts,” *ECS Electrochem. Lett.*, vol. 2, no. 3, pp. F25–F28, 2013.

[49] S. Maass, F. Finsterwalder, G. Frank, R. Hartmann, and C. Merten, “Carbon support oxidation in PEM fuel cell cathodes,” *J. Power Sources*, vol. 176, no. 2, pp. 444–451, 2008.

[50] J. Wang, G. Yin, Y. Shao, S. Zhang, Z. Wang, and Y. Gao, “Effect of carbon black support corrosion on the durability of Pt/C catalyst,” *J. Power Sources*, vol. 171, no. 2, pp. 331–339, 2007.

[51] R. Borup, J. Meyers, B. Pivovar, Y. S. Kim, R. Mukundan, N. Garland, D. Myers, M. Wilson, F. Garzon, D. Wood, P. Zelenay, K. More, K. Stroh, T. Zawodzinski, J. Boncella, J. E. McGrath, M. Inaba, K. Miyatake, M. Hori, K. Ota, Z. Ogumi, S. Miyata, A. Nishikata, Z. Siroma, Y. Uchimoto, K. Yasuda, K. I. Kimijima, and N. Iwashita, “Scientific aspects of polymer electrolyte fuel cell durability and degradation,” *Chem. Rev.*, vol. 107, no. 10, pp. 3904–3951, 2007.

[52] S. A. Vilekar and R. Datta, “The effect of hydrogen crossover on open-circuit voltage in polymer electrolyte membrane fuel cells,” *J. Power Sources*, vol. 195, no. 8, pp. 2241–2247, 2010.

[53] V. O. Mittal, H. R. Kunz, and J. M. Fenton, “Effect of Catalyst Properties on Membrane Degradation Rate and the Underlying Degradation Mechanism in PEMFCs,” *J. Electrochem. Soc.*, vol. 153, no. 9, p. A1755, 2006.

[54] A. Capelo, M. A. Esteves, A. I. de Sá, R. A. Silva, L. Cangueiro, A. Almeida, R. Vilar, and C. M. Rangel, “Stability and durability under potential cycling of Pt/C catalyst with new surface-functionalized carbon support,” *Int. J. Hydrogen Energy*, vol. 41, no. 30, pp. 12962–12975, 2016.

[55] S. Kundu, M. Cimenti, S. Lee, and D. Bessarabov, “Fingerprint of automotive fuel cell cathode catalyst degradation: Pt band in PEMs,” *Membr. Technol.*, vol. 2009, no. 10, pp. 7–10, 2009.

[56] V. a. Sethuraman, J. W. Weidner, A. T. Haug, M. Pemberton, and L. V. Protsailo, “Importance of catalyst stability vis-à-vis hydrogen peroxide formation rates in PEM fuel cell electrodes,” *Electrochim. Acta*, vol. 54, no. 23, pp. 5571–5582, 2009.

[57] B. Wu, M. Zhao, W. Shi, W. Liu, J. Liu, D. Xing, Y. Yao, Z. Hou, P. Ming, J. Gu, and Z. Zou, “The degradation study of Nafion/PTFE composite membrane in PEM fuel cell under accelerated stress tests,” *Int. J. Hydrogen Energy*, vol. 39, no. 26, pp. 14381–14390, 2014.

[58] F. Wang, H. Tang, M. Pan, and D. Li, “Ex situ investigation of the proton exchange membrane chemical decomposition,” *Int. J. Hydrogen Energy*, vol. 33, no. 9, pp. 2283–2288, 2008.

[59] C. H. Bartholomew, “Mechanisms of catalyst deactivation,” *Appl. Catal. A Gen.*, vol. 212, no. 1–2, pp. 17–60, 2001.

[60] T. Ous and C. Arcoumanis, “Degradation aspects of water formation and transport

in Proton Exchange Membrane Fuel Cell: A review," *J. Power Sources*, vol. 240, pp. 558–582, 2013.

[61] M. Eikerling, "Water Management in Cathode Catalyst Layers of PEM Fuel Cells. A Structure-Based Model," *J. Electrochem. Soc.*, vol. 153, no. 3, pp. E58–E70, 2006.

[62] A. Li and S. H. Chan, "Understanding the role of cathode structure and property on water management and electrochemical performance of a PEM fuel cell," *Int. J. Hydrogen Energy*, vol. 38, no. 27, pp. 11988–11995, 2013.

[63] X.-G. Yang, Q. Ye, and P. Cheng, "In-plane transport effects on hydrogen depletion and carbon corrosion induced by anode flooding in proton exchange membrane fuel cells," *Int. J. Heat Mass Transf.*, vol. 55, no. 17–18, pp. 4754–4765, 2012.

[64] C. M. Rangel, R. A. Silva, M. A. Travassos, T. I. Paiva, and V. R. Fernandes, "Fuel Starvation : Irreversible Degradation Mechanisms in PEM Fuel Cells Fuel Starvation : Irreversible Degradation Mechanisms in PEM Fuel Cells," vol. 78, 2010.

[65] M. a. Travassos, V. V. Lopes, R. a. Silva, a. Q. Novais, and C. M. Rangel, "Assessing cell polarity reversal degradation phenomena in PEM fuel cells by electrochemical impedance spectroscopy," *Int. J. Hydrogen Energy*, vol. 38, no. 18, pp. 7684–7696, 2013.

[66] M. Kim, N. Jung, K. Eom, S. J. Yoo, J. Y. Kim, J. H. Jang, H. J. Kim, B. K. Hong,

and E. Cho, “Effects of anode flooding on the performance degradation of polymer electrolyte membrane fuel cells,” *J. Power Sources*, vol. 266, pp. 332–340, 2014.

[67] E. a. Wargo, T. Kotaka, Y. Tabuchi, and E. C. Kumbur, “Comparison of focused ion beam versus nano-scale X-ray computed tomography for resolving 3-D microstructures of porous fuel cell materials,” *J. Power Sources*, vol. 241, pp. 608–618, 2013.

[68] J. Gelb, M. Feser, A. Tkachuk, G. Hsu, S. Chen, H. Chang, T. Fong, L. Hunter, I. Goldberger, S.-H. Lau, and W. Yun, “Sub-micron X-ray Computed Tomography for Non-Destructive 3D Visualization and Analysis,” *Microsc. Microanal.*, vol. 15, no. S2, pp. 618–619, Jul. 2009.

[69] P. R. Shearing, R. S. Bradley, J. Gelb, F. Tariq, P. J. Withers, and N. P. Brandon, “Exploring microstructural changes associated with oxidation in Ni-YSZ SOFC electrodes using high resolution X-ray computed tomography,” *Solid State Ionics*, vol. 216, pp. 69–72, 2012.

[70] B. Hornberger, H. Bale, A. Merkle, M. Feser, W. Harris, S. Etchin, M. Leibowitz, W. Qiu, A. Tkachuk, A. Gu, R. S. Bradley, X. Lu, P. J. Withers, A. Clarke, K. Henderson, N. Cordes, and B. M. Patterson, “X-ray microscopy for in situ characterization of 3D nanostructural evolution in the laboratory,” *X-Ray Nanoimaging Instruments Methods Ii*, vol. 9592, p. 95920Q, 2015.

[71] A. Schneider, C. Wieser, J. Roth, and L. Helfen, “Impact of synchrotron radiation on fuel cell operation in imaging experiments,” *J. Power Sources*, vol. 195, no. 19, pp. 6349–6355, 2010.

[72] J. Evan, James E., Blackborow, Paul, Horne, Stephen F., Gelb, “WHOLE CELL TOMOGRAPHY/MOLECULAR BIOLOGY/STRUCTURAL BIOLOGY: Affordable x-ray microscopy with nanoscale resolution,” *BioOptics World*, 2013.

[73] S. H. Lau, G. Wang, M. Chandrasekeran, V. Fan, M. Nazrul, H. Chang, T. Fong, J. Gelb, M. Feser, and W. Yun, “Multiscale 3D Bioimaging: from cell, tissue to whole organism,” *Soc. Photo-Optical Instrum. Eng. Conf. Ser.*, vol. 7378, p. 73781V–73781V–9, 2009.

[74] A. Tkachuk, F. Duewer, H. Cui, M. Feser, S. Wang, and W. Yun, “X-ray computed tomography in Zernike phase contrast mode at 8 keV with 50-nm resolution using Cu rotating anode X-ray source,” *Zeitschrift fur Krist.*, vol. 222, no. 11, pp. 650–655, 2007.

[75] M. D. Bartlett, A. Fassler, N. Kazem, E. J. Markvicka, P. Mandal, and C. Majidi, “Stretchable, High-k Dielectric Elastomers through Liquid-Metal Inclusions,” *Adv. Mater.*, pp. 3726–3731, 2016.

[76] A. S. Kumar, P. Mandal, Y. Zhang, and S. Litster, “Image segmentation of nanoscale Zernike phase contrast X-ray computed tomography images,” *J. Appl. Phys.*, vol. 117, no. 18, p. 183102, 2015.

[77] S. Komini Babu, A. I. Mohamed, J. F. Whitacre, and S. Litster, “Multiple imaging mode X-ray computed tomography for distinguishing active and inactive phases in lithium-ion battery cathodes,” *J. Power Sources*, vol. 283, pp. 314–319, Jun. 2015.

[78] S. Komini Babu, H. T. Chung, G. Wu, P. Zelenay, and S. Litster, “Modeling

Hierarchical Non-Precious Metal Catalyst Cathodes for PEFCs Using Multi-Scale X-ray CT Imaging," *ECS Trans.*, vol. 64, no. 3, pp. 281–292, 2014.

[79] P. Krüger, S. Niese, E. Zschech, J. Gelb, M. Feser, I. McNulty, C. Eyberger, and B. Lai, "Improved Scanning Geometry to Collect 3D-Geometry Data in Flat Samples," 2011, pp. 258–260.

[80] A. T. Naseri, B. A. Peppley, J. G. Pharoah, P. Mandal, S. Litster, and N. Abatzoglou, "X-ray tomography-based analysis of transport and reaction in the catalyst coating of a reformer," *Chem. Eng. Sci.*, vol. 138, pp. 499–509, 2015.

[81] P. R. Shearing, J. Gelb, and N. Brandon, "Characterization of SOFC Electrode Microstructure Using Nano-Scale X-ray Computed Tomography and Focused Ion Beam Techniques: a Comparative Study," *ECS Trans.* , vol. 19 , no. 17 , pp. 51–57, 2009.

[82] Z. Liang, Y. Guan, G. Liu, R. Bian, X. Zhang, Y. Xiong, and Y. Tian, "Reconstruction of limited-angle and few-view nano-CT image via total variation iterative reconstruction," *X-Ray Nanoimaging: Instruments and Methods*, vol. 8851, p. 885113, 2013.

[83] P. Oliveira, "Adaptative Total Variation Image Deblurring : A Majorization-Minimization Approach," pp. 1–25.

[84] P. Choi, V. Kedlaya, P. Mandal, S. Frisco, J. Whitacre, and S. Litster, "In-Operando Imaging of Electrodeposition and Dendrites Using Nanoscale X-Ray Computed Tomography," *ECS Trans. Abstr.*, vol. PRiME 2016, pp. 4–5, 2016.

[85] Z. Xia, Q. Wang, M. Eikerling, and Z. Liu, “Effectiveness factor of Pt utilization in cathode catalyst layer of polymer electrolyte fuel cells,” *Can. J. Chem.*, vol. 86, no. 7, pp. 657–667, Jul. 2008.

[86] P. P. Mukherjee and C.-Y. Wang, “Direct numerical simulation modeling of bilayer cathode catalyst layers in polymer electrolyte fuel cells,” *J. Electrochem. Soc.*, vol. 154, no. 11, pp. B1121–B1131, 2007.

[87] W. Sun, B. A. Peppley, and K. Karan, “An improved two-dimensional agglomerate cathode model to study the influence of catalyst layer structural parameters,” *Electrochim. Acta*, vol. 50, no. 16–17, pp. 3359–3374, 2005.

[88] W. K. Epting and S. Litster, “Effects of an agglomerate size distribution on the PEFC agglomerate model,” *Int. J. Hydrogen Energy*, vol. 37, no. 10, pp. 8505–8511, 2012.

[89] S. Litster, W. Epting, and E. Wargo, “Morphological Analyses of Polymer Electrolyte Fuel Cell Electrodes with Nano- Scale Computed Tomography Imaging,” *Fuel Cells*, no. 4, 2013.

[90] R. Thiele, S., Severin, Vierrath, Klingele, Matthias, Zengerle, “Tomographic Analysis of Polymer Electrolyte Fuel Cell Catalyst Layers: Methods, Validity and Challenges,” *ECS Trans.*, vol. 69, no. 17, pp. 409–418, 2015.

[91] A. Kongkanand and M. F. Mathias, “The Priority and Challenge of High-Power Performance of Low-Platinum Proton-Exchange Membrane Fuel Cells,” *J. Phys. Chem. Lett.*, vol. 7, no. 7, pp. 1127–1137, 2016.

[92] H. Liu, W. K. Epting, and S. Litster, “Gas Transport Resistance in Polymer Electrolyte Thin Films on Oxygen Reduction Reaction Catalysts,” *Langmuir*, vol. 31, no. 36, pp. 9853–9858, 2015.

[93] A. Z. Weber and A. Kusoglu, “Unexplained Transport Resistances for Low-Loaded Fuel-Cell Catalyst Layers,” *J. Mater. Chem. A*, vol. 2, no. c, pp. 17207–17211, 2014.

[94] R. Bashyam and P. Zelenay, “A class of non-precious metal composite catalysts for fuel cells,” *Nature*, vol. 443, no. 7107, pp. 63–66, Sep. 2006.

[95] T. R. Ralph and M. P. Hogarth, “Catalysis for Low Temperature Fuel Cells,” *Reading*, vol. 46, no. January, pp. 117–135, 2002.

[96] H. A. Gu, Wenbin, Yu, Paul T., Carter, Robert N., Makharia, Rohit, Gasteiger, “Modeling ofMembrane-Electrode-Assembly Degradation in Proton-Exchange-Membrane Fuel Cells – Local H2 Starvation and Start–Stop Induced Carbon-Support Corrosion,” in *Modeling and Diagnostics of Polymer Electrolyte Fuel Cells, Modern Aspects of Electrochemistry*, vol. 49, C.-Y. Pasaogullari, Ugur, Wang, Ed. Springer Science+Business Media, LLC, 2010, pp. 45–87.

[97] J. Dillet, D. Spernjak, A. Lamibrac, G. Maranzana, R. Mukundan, J. Fairweather, S. Didierjean, R. L. Borup, and O. Lottin, “Impact of flow rates and electrode specifications on degradations during repeated startups and shutdowns in polymer-electrolyte membrane fuel cells,” *J. Power Sources*, vol. 250, pp. 68–79, 2014.

[98] J. Durst, A. Lamibrac, F. Charlot, J. Dillet, L. F. Castanheira, G. Maranzana, L.

Dubau, F. Maillard, M. Chatenet, and O. Lottin, “Degradation heterogeneities induced by repetitive start/stop events in proton exchange membrane fuel cell: Inlet vs. outlet and channel vs. land,” *Appl. Catal. B Environ.*, vol. 138–139, pp. 416–426, 2013.

[99] L. Dubau, L. Castanheira, F. Maillard, M. Chatenet, O. Lottin, G. Maranzana, J. Dillet, A. Lamibrac, J. C. Perrin, E. Moukheiber, A. Elkaddouri, G. De Moor, C. Bas, L. Flandin, and N. Caqué, “A review of PEM fuel cell durability: Materials degradation, local heterogeneities of aging and possible mitigation strategies,” *Wiley Interdiscip. Rev. Energy Environ.*, vol. 3, no. 6, pp. 540–560, 2014.

[100] N. Yousfi-Steiner, P. Moçotéguy, D. Candusso, and D. Hissel, “A review on polymer electrolyte membrane fuel cell catalyst degradation and starvation issues: Causes, consequences and diagnostic for mitigation,” *J. Power Sources*, vol. 194, no. 1, pp. 130–145, Oct. 2009.

[101] Y. Yu, H. Li, H. Wang, X.-Z. Yuan, G. Wang, and M. Pan, “A review on performance degradation of proton exchange membrane fuel cells during startup and shutdown processes: Causes, consequences, and mitigation strategies,” *J. Power Sources*, vol. 205, pp. 10–23, May 2012.

[102] F. Zhou, S. J. Andreasen, S. K. Kær, and D. Yu, “Analysis of accelerated degradation of a HT-PEM fuel cell caused by cell reversal in fuel starvation condition,” *Int. J. Hydrogen Energy*, vol. 40, no. 6, pp. 2833–2839, 2015.

[103] Z. J. Mellinger and J. G. Chen, *Electrocatalysis in Fuel Cells*, vol. 9. 2013.

[104] R. T. Atanasoski, A. L. L., and C. D. A., “Efficient Oxygen Evolution Reaction Catalysts for Cell Reversal and Start/Stop Tolerance,” in *Electrocatalysis in Fuel Cells: A Non- and Low Platinum Approach,* M. Shao, Ed. London: Springer Science+Business Media, LLC, 2013.

[105] S. Ye, “Reversal-tolerant catalyst layers,” in *PEM Fuel Cell Electrocatalyts and Catalyst Layers: Fundamentals and Applications*, J. Zhang, Ed. London: Springer-Verlag, 2008.

[106] R. H. Barton, “Cell voltage monitor for a fuel cell stack.” Google Patents, 20-Apr-2004.

[107] I. C. Halalay, S. Swathirajan, B. Merzougui, M. P. Balogh, G. C. Garabedian, and M. K. Carpenter, “Anode Materials for Mitigating Hydrogen Starvation Effects in PEM Fuel Cells,” *J. Electrochem. Soc.* , vol. 158 , no. 3 , pp. B313–B321, Mar. 2011.

[108] S. Trasatti, “Physical electrochemistry of ceramic oxides,” *Electrochim. Acta,* vol. 36, no. 2, pp. 225–241, 1991.

[109] A. Marshall, “Electrocatalysts for the Oxygen Evolution Electrode in Water Electrolysers using Proton Exchange Membranes : Synthesis and Characterisation,” Norwegian University of Science and Technology, Trondheim, 2005.

[110] H. A. Gasteiger, J. E. Panels, and S. G. Yan, “Dependence of PEM fuel cell performance on catalyst loading,” *J. Power Sources,* vol. 127, no. 1–2, pp. 162–

171, Mar. 2004.

[111] H. J. Cho, H. Jang, S. Lim, E. Cho, T. H. Lim, I. H. Oh, H. J. Kim, and J. H. Jang, "Development of a novel decal transfer process for fabrication of high-performance and reliable membrane electrode assemblies for PEMFCs," *Int. J. Hydrogen Energy*, vol. 36, no. 19, pp. 12465–12473, 2011.

[112] R. Adams and R. L. Shriner, "PLATINUM OXIDE AS A CATALYST IN THE REDUCTION OF ORGANIC COMPOUNDS. III. PREPARATION AND PROPERTIES OF THE OXIDE OF PLATINUM OBTAINED BY THE FUSION OF CHLOROPLATINIC ACID WITH SODIUM NITRATE1," *J. Am. Chem. Soc.*, vol. 45, no. 9, pp. 2171–2179, Sep. 1923.

[113] J.-G. Oh, W. H. Lee, and H. Kim, "The inhibition of electrochemical carbon corrosion in polymer electrolyte membrane fuel cells using iridium nanodendrites," *Int. J. Hydrogen Energy*, vol. 37, no. 3, pp. 2455–2461, 2012.

[114] K. Kinoshita, "Application of Carbon in Electrochemical Systems.," in *Carbon: Electrochemical and Physiochemical Properties*, New York: John Wiley & Sons, 1988.

[115] Z. Zhao, L. Castanheira, L. Dubau, G. Berthomé, A. Crisci, and F. Maillard, "Carbon corrosion and platinum nanoparticles ripening under open circuit potential conditions," *J. Power Sources*, vol. 230, pp. 236–243, 2013.

[116] T. Kim, T. Xie, W. Jung, F. Gadala-Maria, P. Ganesan, and B. N. Popov, "Development of catalytically active and highly stable catalyst supports for

polymer electrolyte membrane fuel cells," *J. Power Sources*, vol. 273, pp. 761–774, 2015.

[117] L. M. Roen, C. H. Paik, and T. D. Jarvi, "Electrocatalytic Corrosion of Carbon Support in PEMFC Cathodes," *Electrochem. Solid-State Lett.*, vol. 7, no. 1, p. A19, 2004.

[118] K. H. Kangasniemi, D. a. Condit, and T. D. Jarvi, "Characterization of Vulcan Electrochemically Oxidized under Simulated PEM Fuel Cell Conditions," *J. Electrochem. Soc.*, vol. 151, no. 4, pp. E125–E132, 2004.

[119] S. a. Grigoriev, K. a. Dzhus, D. G. Bessarabov, and P. Millet, "Failure of PEM water electrolysis cells: Case study involving anode dissolution and membrane thinning," *Int. J. Hydrogen Energy*, vol. 39, no. 35, pp. 1–7, 2014.

[120] N. Danilovic, R. Subbaraman, K.-C. Chang, S. H. Chang, Y. J. Kang, J. Snyder, A. P. Paulikas, D. Strmcnik, Y.-T. Kim, D. Myers, V. R. Stamenkovic, and N. M. Markovic, "Activity−Stability Trends for the Oxygen Evolution Reaction on Monometallic Oxides in Acidic Environments," *J. Phys. Chem. Lett.*, vol. 5, pp. 2474–2478, 2014.

[121] J. Juodkazyte, B. ??ebeka, I. Valsiunas, and K. Juodkazis, "Iridium anodic oxidation to Ir(III) and Ir(IV) hydrous oxides," *Electroanalysis*, vol. 17, no. 11, pp. 947–952, 2005.

[122] J. Horkans, "An Investigation of the Electrochemistry of a Series of Metal Dioxides with Rutile-Type Structure: MoO[sub 2], WO[sub 2], ReO[sub 2],

RuO[sub 2], OsO[sub 2], and IrO[sub 2],” *J. Electrochem. Soc.*, vol. 124, no. August, pp. 1202–1207, 1977.

[123] S. Xiao and H. Zhang, “The investigation of resin degradation in catalyst layer of proton exchange membrane fuel cell,” *J. Power Sources*, vol. 246, pp. 858–861, 2014.

[124] S. D. Knights, K. M. Colbow, J. St-Pierre, and D. P. Wilkinson, “Aging mechanisms and lifetime of PEFC and DMFC,” *J. Power Sources*, vol. 127, no. 1–2, pp. 127–134, 2004.

[125] Y. Shao, G. Yin, Z. Wang, and Y. Gao, “Proton exchange membrane fuel cell from low temperature to high temperature: Material challenges,” *J. Power Sources*, vol. 167, no. 2, pp. 235–242, 2007.

[126] S. Hong, Bo Ki; Mandal, Pratiti; Oh, Jong-Gil; Litster, “On the impact of water activity on reversal tolerant fuel cell anode performance and durability,” *J. Power Sources*, vol. (In Press), 2016.

[127] D. G. Sanchez, D. G. Diaz, R. Hiesgen, I. Wehl, and K. A. Friedrich, “Oscillations of PEM fuel cells at low cathode humidification,” *J. Electroanal. Chem.*, vol. 649, no. 1–2, pp. 219–231, 2010.

[128] R. Lin, C. Cao, J. Ma, E. Gülzow, and K. Andreas Friedrich, “Optimizing the relative humidity to improve the stability of a proton exchange membrane by segmented fuel cell technology,” *Int. J. Hydrogen Energy*, vol. 37, no. 4, pp. 3373–3381, 2012.

[129] K. A. F. Daniel G. Sanchez , Alfredo Ortiz, “Oscillation of PEFC under Low Cathode Humidification: Effect of Gravitation and Bipolar Plate Design Daniel G. Sanchez,” *J. Electrochem. Soc.*, vol. 160, no. 6, pp. F636–F644, 2013.

[130] H. Schulenburg and B. Schwanitz, “3D imaging of catalyst support corrosion in polymer electrolyte fuel cells,” *J. Phys. Chem. C*, vol. 115, pp. 14236–14243, 2011.

[131] J. H. Ohs, U. S. Sauter, and S. Maass, “Degradation Caused by Dynamic Operation and Starvation Conditions,” in *Fuel Cell Science and Engineering: Materials, Processes, Systems and Technology*, 1st ed., D. Stolten and B. Emonts, Eds. Wiley-VCH Verlag GmbH & Co. KGaA, 2012.

[132] F. Maillard, A. Bonnefont, and F. Micoud, “An EC-FTIR study on the catalytic role of Pt in carbon corrosion,” *Electrochem. commun.*, vol. 13, no. 10, pp. 1109–1111, 2011.

[133] C. H. Bartholomew, A. Caroline, R. Eric, M. Nicolas, P. Millet, G. Cell, V. Sources, P. E. Membrane, F. Cell, O. E. Electrode, A. Malolepszy, M. Mazurkiewicz, L. Stobinski, B. Lesiak, L. Kövér, J. Tóth, B. Mierzwa, A. Borodzinski, F. Nitze, T. Wågberg, C. Rozain, E. Mayousse, N. Guillet, P. Millet, M. I. T. Student, X.-G. Yang, Q. Ye, P. Cheng, and V. Venezlan, “‘ INNER ’ AND ‘ OUTER ’ ACTIVE SURFACE ELECTRODES OF RuO ,” *Appl. Catal. A Gen.*, vol. 55, no. 22, pp. 1–10, 2015.

[134] H. L. Xin, J. A. Mundy, Z. Liu, R. Cabezas, R. Hovden, L. F. Kourkoutis, J. Zhang, N. P. Subramanian, R. Makharia, F. T. Wagner, and D. A. Muller,

"Atomic-resolution spectroscopic imaging of ensembles of nanocatalyst particles across the life of a fuel cell.," *Nano Lett.*, vol. 12, no. 1, pp. 490–7, 2012.

[135] W. Chao, J. Kim, S. Rekawa, P. Fischer, and E. H. Anderson, "Demonstration of 12 nm resolution Fresnel zone plate lens based soft x-ray microscopy.," *Opt. Express*, vol. 17, no. 20, pp. 17669–17677, 2009.

[136] J. H. Kim, Y. Yeon Jo, E. A. Cho, J. H. Jang, H. J. Kim, T.-H. Lim, I.-H. Oh, J. J. Ko, and I. J. Son, "Effects of Cathode Inlet Relative Humidity on PEMFC Durability during Startup–Shutdown Cycling," *J. Electrochem. Soc.*, vol. 157, no. 5, pp. B633–B642, 2010.

[137] L. Dubau, L. Castanheira, M. Chatenet, F. Maillard, J. Dillet, G. Maranzana, S. Abbou, O. Lottin, G. De Moor, A. El Kaddouri, C. Bas, L. Flandin, E. Rossinot, and N. Caqu??, "Carbon corrosion induced by membrane failure: The weak link of PEMFC long-term performance," *Int. J. Hydrogen Energy*, vol. 9, 2014.

[138] R. Lin, B. Li, Y. P. Hou, and J. M. Ma, "Investigation of dynamic driving cycle effect on performance degradation and micro-structure change of PEM fuel cell," *Int. J. Hydrogen Energy*, vol. 34, no. 5, pp. 2369–2376, Mar. 2009.

[139] R. L. Borup, J. R. Davey, F. H. Garzon, D. L. Wood, and M. A. Inbody, "PEM fuel cell electrocatalyst durability measurements," *J. Power Sources*, vol. 163, no. 1, pp. 76–81, Dec. 2006.

[140] K. H. Lim, H.-S. Oh, S.-E. Jang, Y.-J. Ko, H.-J. Kim, and H. Kim, "Effect of operating conditions on carbon corrosion in polymer electrolyte membrane fuel

cells," *J. Power Sources*, vol. 193, no. 2, pp. 575–579, Sep. 2009.

[141] S. Mandal, Pratiti; Hong, Bo KI; Oh, Jong-Gil;Litster, "Understanding the voltage reversal behavior of automotive fuel cells," *Energy Environ. Sci.*, vol. (Manuscrip, 2016.

[142] J. Xie, F. Garzon, T. Zawodzinski, and W. Smith, "Ionomer segregation in composite MEAs and its effect on polymer electrolyte fuel cell performance," *J. Electrochem. Soc.*, vol. 151, no. 7, pp. A1084–A1093, 2004.

[143] A. Caroline, R. Eric, M. Nicolas, and P. Millet, "Influence of iridium oxide loadings on the performance of PEM water electrolysis cells : Part I – Pure IrO 2 - based anodes," *Elsevier B.V.*, 2015.

[144] S. Gouws, "Voltammetric Characterization Methods for the PEM Evaluation of Catalysts," *Electrolysis*, 2012.

[145] A. Skulimowska, M. Dupont, M. Zaton, S. Sunde, L. Merlo, D. J. Jones, and J. Rozie, "Proton exchange membrane water electrolysis with short-side-chain Aquivion membrane and IrO2 anode catalyst," *Int. J. Hydrogen Energy*, vol. 39, pp. 6307–6316, 2014.

[146] J. Rossmeisl, A. Logadottir, and J. K. Nørskov, "Electrolysis of water on (oxidized) metal surfaces," *Chem. Phys.*, vol. 319, no. 1–3, pp. 178–184, 2005.

[147] T. E. Mallouk, "Water electrolysis: Divide and conquer," *Nat. Chem.*, vol. 5, no. 5, pp. 362–363, 2013.

[148] E. Zoulias and E. Varkaraki, "A review on water electrolysis," *TCJST*, vol. 4, no.

2, pp. 41–71, 2004.

[149] T. R. Ralph, S. Hudson, and D. P. Wilkinson, “ELECTROCATALYST STABILITY IN PEMFCs AND THE ROLE OF FUEL STARVATION AND CELL REVERSAL TOLERANT ANODES,” *ECS Trans.*, vol. 1, no. 8, pp. 67–84, 2006.

[150] K. Schmidt-Rohr and Q. Chen, “Parallel cylindrical water nanochannels in Nafion fuel-cell membranes,” *Nat Mater*, vol. 7, no. 1, pp. 75–83, Jan. 2008.

[151] M. B. Satterfleld and J. B. Benziger, “Non-Fickian water vapor sorption dynamics by nafion membranes,” *J. Phys. Chem. B*, vol. 112, no. 12, pp. 3693–3704, 2008.

[152] D. C. Huang, P. J. Yu, F. J. Liu, S. L. Huang, K. L. Hsueh, Y. C. Chen, C. H. Wu, W. C. Chang, and F. H. Tsau, “Effect of dispersion solvent in catalyst ink on proton exchange membrane fuel cell performance,” *Int. J. Electrochem. Sci.*, vol. 6, no. 7, pp. 2551–2565, 2011.

[153] Y.-J. Wang, N. Zhao, B. Fang, H. Li, X. T. Bi, and H. Wang, “Effect of different solvent ratio (ethylene glycol/water) on the preparation of Pt/C catalyst and its activity toward oxygen reduction reaction,” *RSC Adv.*, vol. 5, no. 70, pp. 56570–56577, 2015.

[154] S. Shukla, S. Bhattacharjee, and M. Secanell, “Rationalizing Catalyst Inks for PEMFC Electrodes Based on Colloidal Interactions,” *ECS Trans.* , vol. 58 , no. 1 , pp. 1409–1428, 2013.

[155] W. Wang, S. Chen, J. Li, and W. Wang, “Fabrication of catalyst coated membrane

with screen printing method in a proton exchange membrane fuel cell," *Int. J. Hydrogen Energy*, pp. 1–10, 2014.

[156] V. Mehta and J. S. Cooper, "Review and analysis of PEM fuel cell design and manufacturing," *J. Power Sources*, vol. 114, no. 1, pp. 32–53, Feb. 2003.

[157] C. Wang, S. Wang, L. Peng, J. Zhang, Z. Shao, J. Huang, C. Sun, M. Ouyang, and X. He, "Recent Progress on the Key Materials and Components for Proton Exchange Membrane Fuel Cells in Vehicle Applications," *Energies*, vol. 9, no. 8, p. 603, Jul. 2016.

[158] L. Du, Y. Shao, J. Sun, G. Yin, J. Liu, and Y. Wang, "Advanced catalyst supports for PEM fuel cell cathodes," *Nano Energy*, pp. 1–9, 2016.

[159] C. Marichy, G. Ercolano, G. Caputo, M. G. Willinger, D. Jones, J. Rozière, N. Pinna, and S. Cavaliere, "ALD SnO2 Protective Decoration Enhances the Durability of a Pt Based Electrocatalyst," *J. Mater. Chem. A*, 2015.

[160] A. Pătru, A. Rabis, S. E. Temmel, R. Kotz, and T. J. Schmidt, "Pt/IrO2–TiO2 cathode catalyst for low temperature polymer electrolyte fuel cell – Application in MEAs, performance and stability issues," *Catal. Today*, pp. 20–22, 2015.

[161] S. Yin, S. Mu, H. Lv, N. Cheng, M. Pan, and Z. Fu, "A highly stable catalyst for PEM fuel cell based on durable titanium diboride support and polymer stabilization," *Appl. Catal. B Environ.*, vol. 93, no. 3–4, pp. 233–240, 2010.

[162] E. C. S. Transactions and T. E. Society, "Pt-decorated TiO 2 Electrocatalysts for PEFCs M. Iwami," *ECS Trans.*, vol. 69, no. 17, pp. 603–609, 2015.

Page intentionally left blank

Appendix I

MEA Fabrication Using Decal Transfer Method

In this section, the procedure for fabricating PEFC electrode using the decal-transfer method has been described. The method is primarily based on the procedure described in [13], [111] and [142], however, some changes were needed to achieve best results in the specific laboratory conditions and equipment. The steps are enumerated below:

1. The catalyst ink was coated onto a PTFE-coated fiber glass fabric (bought from McMaster-Carr) and dried in ambient condition for 24 hours. This film was used as the decal. Some researchers have reported the use of Kapton® as the decal substrate [13], [154], which did not work so well in our case.
2. The decal was cut into the size of the MEA that is to be fabricated, and a piece of Nafion® membrane of a larger size was taken (this is to assure better gas sealing around the edges of the MEA which is masked by the sub-gasket). The catalyst coated side of the decal was placed on the membrane.
3. Meanwhile the hot-press (Carver, Inc.) was heated up to 120°C. The decal-membrane assembly was placed between layers of stacked up layers of PTFE-coated fiber glass fabric with adhesive backing. A schematic of the assembly is

shown in Figure A.1. These layers in were housed between two 1/16” thick metallic sheets. The layers of film with adhesive backing have a silicone layer, which acts as a compressible layer that helps distribute the pressure from the hot press uniformly on the decal substrate and membrane. The uniformity of the pressure can be checked using pressure sensitive films in between the platens. This whole assembly is then plated between the heated plates.

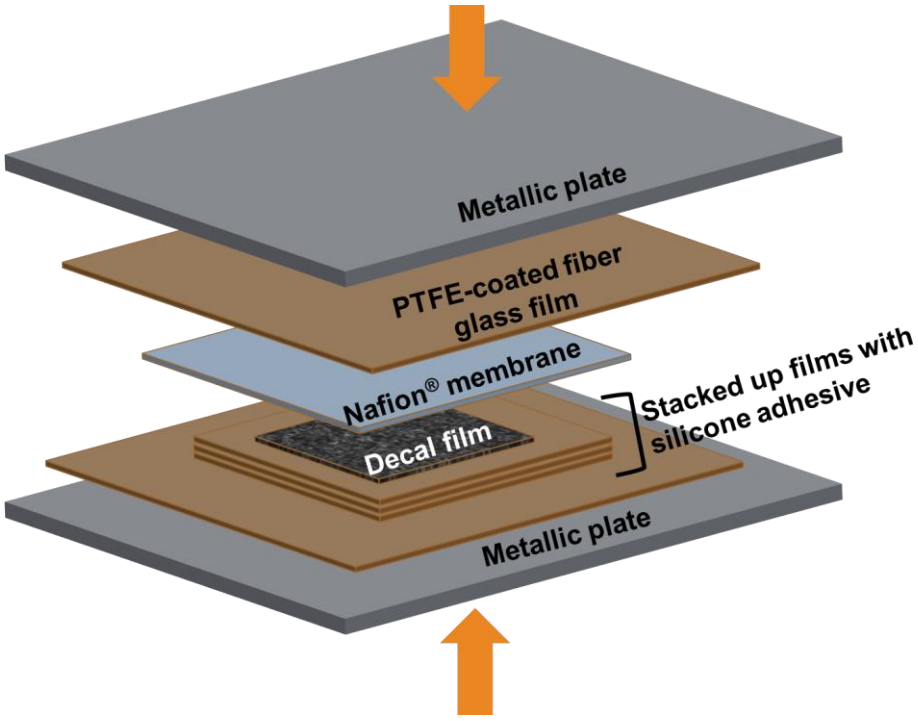

Figure A.1. Schematic representation of the arrangement of the film layers for MEA fabrication using decal-transfer.

4. The platens were then pressed together. The load applied was 360 lb for a MEA surface are of 1 - 4 cm^2 for 5-8 min. The plates can be rotated by 90 every 2 min, to ensure the whole area gets uniform pressure. This step is not necessary for small (~ 1 cm^2) surface area.

5. The pressure was released the films along with the thin metal plates is carefully taken out of the hot-press and left undisturbed to cool for ~ 10 min. The decal substrate was then peeled off the membrane. This leaves the catalyst layer bonded onto the membrane. The weight of the decal substrate should be measured before and after the decal transfer, to determine the catalyst loading on the MEA.

6. In order to coat both the anode and the cathode onto the membrane, the decal transfer can be done in a single step with the two decals on either side of the membrane or one after the other. The former is preferred because it will subject the membrane to the high heat condition for a shorter duration thus reducing possibilities of heat induced degradation of the membrane.
